

## REVIEW ARTICLE

10.1002/2017RG000586

## Key Points:

- Similar processes drive geodetic observations of the earthquake cycle along different convergent margins
- Normal faulting aftershocks may result from a delay in afterslip downslip of the coseismic thrust
- Postseismic processes mask interface relocking in the geodetic observations

## Supporting Information:

- Supporting Information S1
- Movie S1

## Correspondence to:

R. Govers,  
r.govers@uu.nl

## Citation:

Govers, R., Furlong, K. P., van de Wiel, L., Herman, M. W., & Broerse, T. (2018). The geodetic signature of the earthquake cycle at subduction zones: Model constraints on the deep processes. *Reviews of Geophysics*, 56, 6–49. <https://doi.org/10.1002/2017RG000586>

Received 3 SEP 2017

Accepted 22 NOV 2017

Accepted article online 27 NOV 2017

Published online 2 JAN 2018

©2017. The Authors.

This is an open access article under the terms of the Creative Commons Attribution-NonCommercial-NoDerivs License, which permits use and distribution in any medium, provided the original work is properly cited, the use is non-commercial and no modifications or adaptations are made.

# The Geodetic Signature of the Earthquake Cycle at Subduction Zones: Model Constraints on the Deep Processes

R. Govers<sup>1</sup> , K. P. Furlong<sup>2</sup> , L. van de Wiel<sup>1</sup> , M. W. Herman<sup>2</sup> , and T. Broerse<sup>1</sup> 
<sup>1</sup>Tectonophysics Group, Faculty of Geosciences, Utrecht University, Utrecht, Netherlands, <sup>2</sup>Geodynamics Research Group, Geosciences Department, Pennsylvania State University, University Park, PA, USA

**Abstract** Recent megathrust events in Tohoku (Japan), Maule (Chile), and Sumatra (Indonesia) were well recorded. Much has been learned about the dominant physical processes in megathrust zones: (partial) locking of the plate interface, detailed coseismic slip, relocking, afterslip, viscoelastic mantle relaxation, and interseismic loading. These and older observations show complex spatial and temporal patterns in crustal deformation and displacement, and significant differences among different margins. A key question is whether these differences reflect variations in the underlying processes, like differences in locking, or the margin geometry, or whether they are a consequence of the stage in the earthquake cycle of the margin. Quantitative models can connect these plate boundary processes to surficial and far-field observations. We use relatively simple, cyclic geodynamic models to isolate the first-order geodetic signature of the megathrust cycle. Coseismic and subsequent slip on the subduction interface is dynamically (and consistently) driven. A review of global preseismic, coseismic, and postseismic geodetic observations, and of their fit to the model predictions, indicates that similar physical processes are active at different margins. Most of the observed variability between the individual margins appears to be controlled by their different stages in the earthquake cycle. The modeling results also provide a possible explanation for observations of tensile faulting aftershocks and tensile cracking of the overriding plate, which are puzzling in the context of convergence/compression. From the inversion of our synthetic GNSS velocities we find that geodetic observations may incorrectly suggest weak locking of some margins, for example, the west Aleutian margin.

## 1. Introduction

### 1.1. Observing the Seismic Cycle

Key to anticipating and mitigating the consequences of great megathrust earthquakes is our ability to delineate the current slip deficit (potential seismic moment) as it has been accumulating along a particular plate boundary segment and couple that with the record (as preserved in paleoseismic and stratigraphic data) of past earthquakes, their approximate recurrence rate, and the typical extent of rupture in each event. Significant advances in both our ability to observe current rates and patterns of deformation associated with the megathrust (primarily through Global Navigation Satellite System (GNSS, see Glossary) observations (e.g., Sagiya et al., 2000) and detailed observations of the timing, vertical motions, and tsunamigenic character of previous events as preserved in the geologic record (e.g., Witter et al., 2016) indicate the potential to better constrain the size and place of future large events.

There is now a suite of continuous GNSS networks along major subduction zones, which have been accumulating interseismic displacement data. Additionally, the recent occurrence of numerous great earthquakes provides insight into the coseismic and immediate postseismic behavior of the system (e.g., Broerse et al., 2015; Hu et al., 2016; Klein et al., 2016). One thing that has become particularly clear is that (horizontal and vertical) coseismic displacements are not the simple inverse of the integrated interseismic displacements. The (highly variable) recurrence time of these events ranges from a century to millennia. The 50+ years since the great earthquakes of the 1960s thus allows us to observe crustal displacements at an intermediate stage in the earthquake cycle. The net result of these circumstances is a developing picture of the late-cycle, coseismic, early postseismic and intermediate stage observables related to strain accumulation and release.

Similarly, there is a growing number of paleoseismic results relevant to the questions of (particularly) spatial and temporal patterns of vertical motions during the cycle (e.g., Briggs et al., 2014; Meltzner et al., 2010; Sieh

et al., 2008; Wesson et al., 2015; Witter et al., 2014, 2016). For example, the Wesson et al. (2015) study observed vertical motions through a complete seismic cycle bracketed by two megathrust earthquakes at a site associated with the 2010 Maule, Chile, earthquake.

Apparent discrepancies emerge when confronting geodetic data with geological studies. Interseismic locking of the subduction interface is commonly deduced from modern geodetic studies. These inferred patterns of coupling are not always compatible with paleoseismic studies or modern rupture models for large earthquakes. For example, the geologic record provides evidence of one or more large magnitude earthquakes in regions that at present appear to be poorly coupled and thus unlikely to host great earthquakes (Witter et al., 2014). Similarly, the 2006 Kuril Islands great earthquake occurred in a region previously identified as being a location of low strain accumulation (Song & Simons, 2003). Conversely, other areas that are located in regions of moderate coupling or that have other evidence of large events show little to no paleoseismic vertical record of cyclic behavior (even at “good” sites) for events in the region (e.g., Witter et al., 2016). In a site that is near the western terminus of the 1964 Alaska event (a segment boundary for the 1964 rupture?), Briggs et al. (2014) found evidence of multiple tsunami deposits that indicate the area participated in ruptures extending in either direction, indicating that its role as a persistent barrier is unlikely, and the character of the plate boundary interface may change over time.

At least a partial explanation for the mismatch between data and inferences on the earthquake cycle is that our direct observations of subduction megathrust deformational behavior are biased, as the setting of subduction zone margins limits the spatial extent over which key observations can be made. Namely, we typically only have observations over a limited geographical area, and often few GNSS sites lie directly above the interseismic coupled zone, where the spatial sampling is highly variable between the different margins. In a similar fashion, we typically have observations only at isolated times in the earthquake cycle process—modern geodesy such as GNSS provides short-duration views of the deformation at a margin and (paleo)seismology typically only provides data from coseismic and immediate postseismic stages in the cycle (Meade et al., 2013).

What also remains unclear is if variations in the surface observations among several convergent margins reflect real variations in the processes that drive them or rather reflect the different phases of the earthquake cycle. Also ambiguous is the role of variability in the geometry and material properties of the plate boundary zone in generating these observable differences. Whether or not particular subduction zones are special (Wang & Tréhu, 2016) in the sense that their relevant physical characteristics differ from “normal” subduction zones is an important question because it touches on the capability of such atypical regions to produce megathrust events (Bletery et al., 2016; Jarrard, 1986; Pacheco et al., 1993; Ruff & Kanamori, 1980; Schellart & Rawlinson, 2013). It is therefore particularly relevant to identify the main physical components that different subduction zones share.

## 1.2. Deep Earth Processes

Surface deformation before, during, and after an earthquake reflects the contribution of several processes. Coseismic and postseismic slip on the subduction interface causes seaward velocities of the overriding plate. Viscoelastic relaxation of stress perturbations also causes seaward surface velocities. Poroelastic relaxation causes seaward motion above the source region (Hughes et al., 2010). Long-term convergence in combination with locking of (part of) the subduction interface results in landward motion. The net surface velocities vary in different parts of the earthquake cycle (Figure 1), reflecting alternating dominance of these processes.

The following are the main stages of the earthquake cycle in sequential order.

1. During the interseismic interval (late in the earthquake cycle) deformation is dominated by the accumulation of elastic strain in the shallow lithosphere (Figure 1a). This is driven by coupling across a segment of the plate boundary where the interface is mechanically locked between earthquakes. Deformation of the upper plate is confined mostly to the region between the trench and a “backstop” ~300–600 km from the trench. The upper plate shortens and develops horizontal compressive stresses. Upper plate velocities will be landward with a quasi-linear decrease from the trench to the upper plate backstop. Deeper parts of the overriding lithosphere and the mantle wedge/asthenosphere show viscous creep that relaxes stresses while shortening continues.

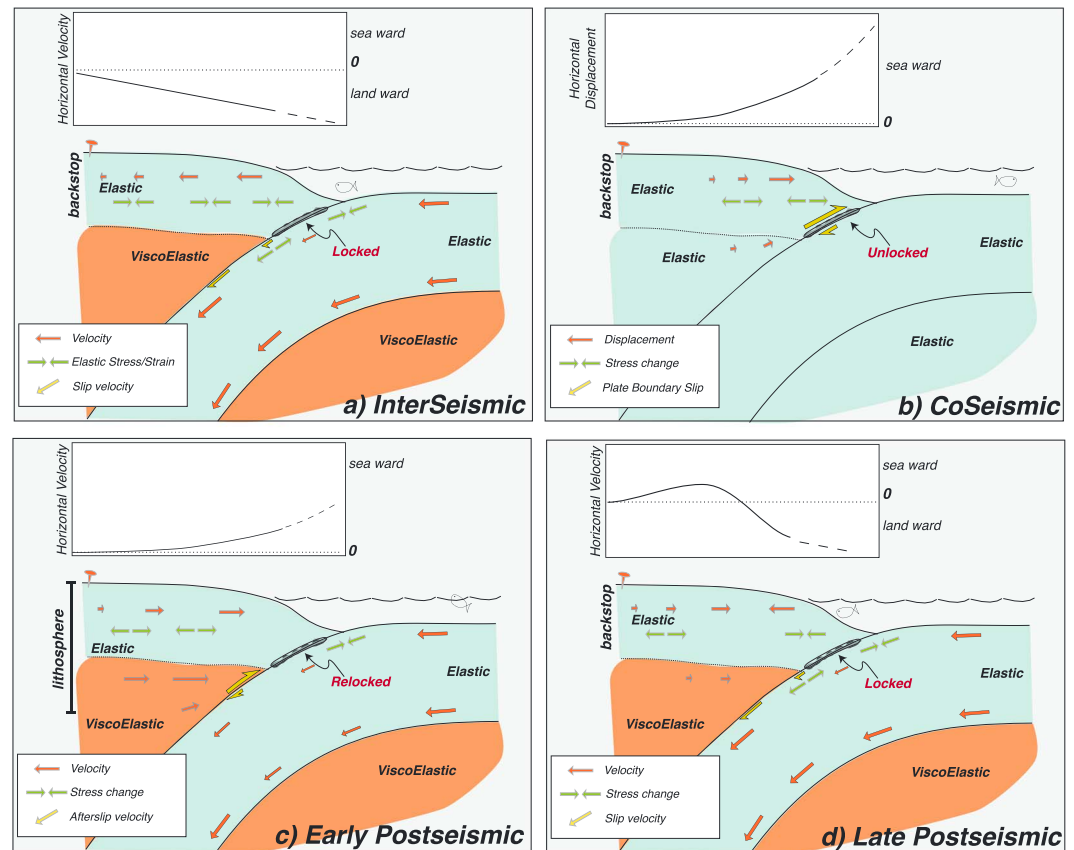


**Figure 1.** Conceptual models of the stress/deformation history during the earthquake cycle in subduction zones. (a) During interseismic times the seismogenic megathrust is locked but the plate boundary down-dip (and up-dip?) of the locked zone deforms at plate motion rates. The upper plate will show a displacement pattern with highest rates of displacement near the trench and the displacements decreasing with distance from the locked plate interface. At depth in the upper plate (lower crust/mantle lithosphere), deformation occurs, but the stresses relax (viscous). For a relatively constant thickness elastic layer, the displacements would vary linearly with position. (b) During earthquake rupture, the previously locked plate interface is unlocked and slips. On the time scale of the earthquake all surrounding rocks are approximately elastic. The upper plate will rebound leading to a nonlinear pattern of seaward surface displacements. (c) During the early postseismic period, the coseismic part of the interface relocks, and afterslip starts on down-dip (and up-dip?) parts of the interface resulting in further seaward velocities. Viscous relaxation commences. (d) Later in the postseismic period the signature of relocking becomes apparent as landward velocities closer to the trench. Further inland postseismic processes have stronger expressions in the surface velocities resulting in continuing seaward velocities.

2. Coseismically much of this characteristic behavior changes (Figure 1b). The locked section of the plate interface is decoupled allowing free slip on that section of the plate boundary, and elastic rebound will occur. Observed horizontal and vertical surface displacements are well reproduced by an elastic half-space with slip on a fault that agrees with seismological observations. The slip/no-slip transition at the down-dip end of the coseismic fault in particular results in surface subsidence. The deeper plate interface thus does not slip coseismically so that remaining slip deficits will not be resolved here during the earthquake.
3. There is evidence that the plate interface may relock shortly after the main earthquake. The most direct evidence comes from postseismic horizontal displacements (GPS/A, offshore) above the northern part of the Tohoku coseismic interface (Tomita et al., 2017; Watanabe et al., 2014). These displacements are directed landward since the first half year after the 2011 event, meaning that the locking signature exceeds the imprint of postseismic processes here. Postseismic subsidence here supports this interpretation. The observations thus provide strong evidence that (significant parts of) the seismogenic fault relocked shortly after the event. Another clear case of relocking is seen in association with the 2006/2007 Kurile Islands great earthquakes (Lay et al., 2009), where the second  $M_w$  8.0 event was an

intraplate normal faulting event within the Pacific plate. Within approximately 1 year, there was a large Pacific plate intraplate compressional event in essentially the same location as the prior normal faulting earthquake, indicative of very rapid (days to weeks) relocking of the interface. Following the 2010 Maule event, Bedford et al. (2016) study the evolution during the first 4 years of horizontal GNSS displacement in terms of direction differences between the long-term relative convergence and locking and the coseismic motion directions. They infer that the interface relocks within the first year after the event, which again is short relative to the duration of the postseismic period. A similar conclusion was drawn by Remy et al. (2016) for the 2007 Pisco (Peru) earthquake.

4. Pressure changes in the rocks and sediments surrounding the source area drive poroelastic flow in the crust of both the overriding and subducted plates. Permeabilities are such that water levels re-equilibrate on time scales of a few months or shorter (Hu et al., 2014; Hughes et al., 2010; Jónsson et al., 2003; Masterlark, 2003). Model studies indicate that poroelastic flow affects surface deformation above the source region, and that the onshore imprint is limited. We will therefore not consider poroelastic deformation.
5. Afterslip may occur during the initial postseismic period (Figure 1c). Depending on the rate and local material properties, it may include aseismic slip and aftershocks. Avouac (2015) reviews the observations for this period and shows that surface deformation in coastal regions is mostly due to afterslip immediately down-dip of the locked part of the interface. Afterslip on the up-dip part of the interface is sometimes observed, for example, following the 2007  $M_w$  8.0 Pisco (south Peru) earthquake (Perfettini et al., 2010) and following the 2005  $M_w$  8.7 Nias earthquake (Hsu et al., 2006). Only a small fraction (1–10%) of the cumulative moment of afterslip occurs as aftershocks (Bedford et al., 2013; Chlieh et al., 2007). Afterslip is commonly found to surround the coseismic ruptures (e.g., Miyazaki et al., 2004; Yagi & Kikuchi, 2003), that is, it occurs exclusively away from the seismic rupture area. However, Johnson et al. (2012) and Perfettini and Avouac (2014) infer some overlap of the areas of coseismic rupture area and afterslip following the 2011  $M_w$  9.1 earthquake. Bedford et al. (2013) draw a similar conclusion for the 2010 Maule earthquake. Observations following major events suggest that afterslip may last a few years (Pritchard & Simons, 2006).
6. Viscoelastic stress relaxation of deeper parts of the lithosphere, and of the asthenosphere, allows additional rebound of the upper plate (Figure 1d). The necessity of such (bulk) viscoelastic relaxation in the first years of the postseismic period is supported by geodetic data (e.g., Broerse et al., 2015; Freed et al., 2017; Hoechner et al., 2008; Klein et al., 2016; Li et al., 2017; Sun et al., 2014; Sun & Wang, 2015). Viscoelastic relaxation is commonly thought to have a dominant imprint on surface velocities during later stages of the postseismic period. Inferred long-term relaxation time scales vary substantially with the assumed rheological properties of the wedge, from many years to a few centuries. During this late postseismic period, the surface displacement pattern reflects the superposition of the interseismic and postseismic patterns. Over time, the postseismic signal will decay, and observations will approach the interseismic pattern. There is strong evidence that within the first year after the event (Wang et al., 2012), regions of the upper plate near the trench (offshore) are moving landward, that is, appear to be well coupled, while the majority of regions are still in the postearthquake relaxation phase with trenchward motions, as seen in Tohoku (Tomita et al., 2017; Watanabe et al., 2014). Fifty years after the 1964 Alaska earthquake the transition from landward to trenchward motion has migrated from near the trench to the region near Cook Inlet, more than 200 km inland from the trench (Li et al., 2016; Suito & Freymueller, 2009). In southern Chile, coastal stations move landward and inland stations move seaward, indicating still ongoing postseismic relaxation following the 1960 Valdivia earthquake (Hu et al., 2004).

While it has been possible to identify these main processes from horizontal surface deformation observations, vertical motions during the earthquake cycle have been more difficult to interpret. One reason is that reliable identification of tectonic components has been feasible only shortly, since the advent of continuous GNSS stations. The other reason is that vertical motions are inherently more sensitive to details of the processes as we will discuss later on.

### 1.3. Mechanical Models

Mechanical models can be important vehicles to connect observations to physical processes, and to constrain the relative contribution of different processes to the data. Also, such models provide a way for



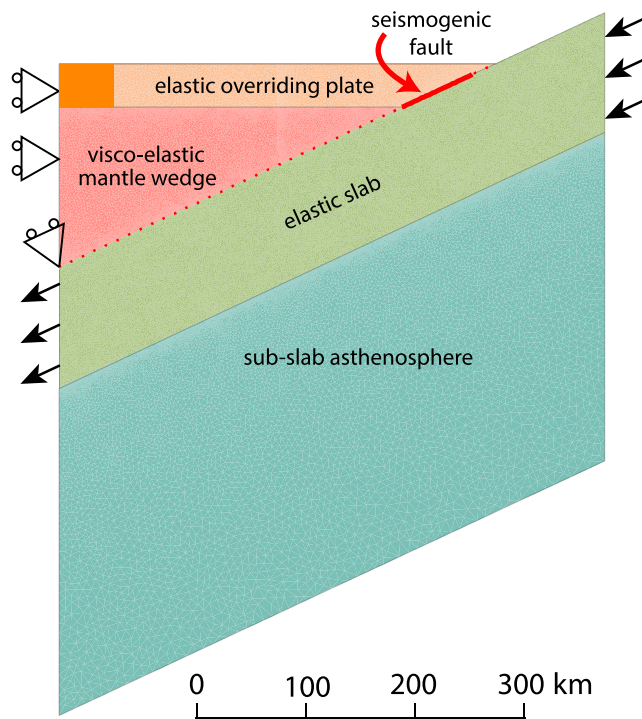


**Figure 2.** Geometry, boundary conditions and distribution of material properties in our model domain, representing a vertical and perpendicular cross section through a subduction plate contact. Arrows stand for the imposed plate velocity. Triangles with wheels are free-slip boundary conditions, and the top left corner is fixed in all directions. The solid red line along the interface is the seismogenic fault, and dotted parts represent updip and downdip fault sections.

interpolating (space and time) sparse data sets. A wide range of models have been used in the context of the subduction earthquake cycle, and the inferences from observations depend strongly on the specific details of the model that was used. Most current studies are based on “single event models.” In this category, models based on simplified geometry and rheology are ubiquitous (an excellent review is given by Cohen, 1999). Some important examples are the elastic half-space models (Okada, 1992) and spherically layered models (Piersanti et al., 1995; Pollitz et al., 2006). These and some more complex models (e.g., Hu et al., 2004; Masterlark, 2003) have been used to model phases of the earthquake cycle.

The second category of “earthquake cycle models” is based on the premise that the earthquake cycle is periodic. In this category, there also are models based on simplified geometry and rheology (e.g., Nur & Mavko, 1974; Thatcher & Rundle, 1984; Matsu’ura & Sato, 1989; Cohen, 1994). These models highlight the significance of earthquake history for the deep processes and their geodetic expression. More complex cycle models (particularly those including an elastic slab) were presented by Wang (1995) and Hirahara (2002), but these papers did not target geodetic observations. With such focus in mind we here develop new earthquake cycle models that are intentionally simple. Inherent in the setup of these models is the potential for further development for studies of permanent strain accumulation on geological time scales. In this paper, we study whether variations in surface displacements seen along all subduction margins can be represented by a single conceptual model.

Before we review available observations for various stages in the megathrust earthquake cycle, we first introduce and motivate our generic

model. We investigate the sensitivity of the model results to variations of model parameters and show that only a few parameters influence the basic model response. Finally, we confront our model with the displacement observations and conclude that the match of the models to these observations is surprisingly good.

## 2. Numerical Model

### 2.1. Modeling Approach

Our goal is to get an overview of the primary controls of the subduction earthquake cycle on geodetic observables at subduction zones. The numerically modeled system, shown in Figure 2, is built on the conceptual model described above (Figure 1). It has an oceanic plate subducting along an inclined boundary, which is 100% locked (interearthquake) to the overriding plate along part of the contact region. Updip and downdip of the locked region, the plate interface is assumed to be able to slip. Earthquakes occur on predefined regular intervals, when the locked patch is unlocked and allowed to freely slip. Regions are assigned elastic or viscoelastic properties that are roughly appropriate for their position and temperature. The system is driven by plate motion. A relatively new aspect of our model is that we run numerous repeating cycles of locking/unlocking, because prestresses may be inherited from previous events. Afterslip is consistently driven by preseismic and coseismic shear stresses.

### 2.2. Model Setup

We study a generic, and therefore simplified/schematic, model in terms of geometry, mechanical properties, and boundary conditions. Variations in slab dip along subduction interfaces in the region of plate coupling are generally small (on the order of 3–5°) (Lallemand et al., 2005) to moderate (15° in case of Tohoku), so we ignore these and represent the slab by a straight beam (dip angle 25°). A consequence of this simplification is an unrealistic geometry, particularly on the oceanic side of the model, but which has the advantage of not generating bending stresses that may complicate the results. We represent the interface between the subducting slab and the overriding plate by a fault. We focus on large earthquakes with an along-strike

dimension of the seismogenic fault plane that is significantly larger than the downdip dimension. This allows us to study a two-dimensional cross section. Another simplification is that we consider trench-perpendicular plate motion only.

We use our in-house finite element package GTECTON version 2017.3 to solve the mechanical equilibrium equations for plane strain (Melosh & Raefsky, 1980; Govers & Wortel, 1993). GTECTON uses the Portable, Extensible Toolkit for Scientific Computation (PETSc version 3.4.2) and OpenMPI (version 1.6) to solve the matrix equations. GTECTON is developed and maintained using the GIT version control system, which is a system for tracking changes and versions of our finite element and associated postprocessing software. The most important update of the finite element code relative to the implementation of Govers and Wortel (2005) is that it now runs fully (and massively) parallel for 2-D, axisymmetric, and 3-D simulations. GTECTON has been successfully verified against a wide range of benchmark problems. Model results are plotted using Generic Mapping Tools (GMT version 5.2.1) (Wessel et al., 2013), which is a collection of public-domain tools for manipulating and plotting a wide range of data. We used convergence tests to demonstrate that the results are insensitive to further refinement in spatial and temporal discretization.

As we will be driving our models to (long-term) steady state, initial stresses (mostly pressures resulting from gravity) are assumed to be in equilibrium with the boundary conditions and body force; that is, we assume that subduction has been going on forever. Given that the mechanical equilibrium equations are linear, we can ignore these background stresses and gravity in the context of the models, which will focus on stress perturbations through the earthquake cycle.

We first present the results of a starting model. We refer to this model as our reference (REF) model because subsequent models will be compared to it. The REF model is driven by velocity boundary conditions of 4 cm/yr on the lateral edges of a slab. The base of the slab corresponds roughly with an isotherm; at this depth and below it viscoelastic flow occurs on the time scale of the earthquake cycle. As a consequence, the slab thickness corresponds with the thermal plate thickness; that is, the slab is significantly thicker than the (long-term) effective elastic thickness for flexure. In our REF model, we choose a slab thickness of 100 km (Figure 2), which corresponds with an oceanic age  $\geq 100$  Myr (Doin & Fleitout, 1996). The left side of the overriding plate can only move vertically; that is, it acts as the far field backstop. The downdip end of the slab can only move parallel to the slab. The reason for this is that in the context of this problem we are not interested in the dynamic topography that would be induced by slab-perpendicular motion. The top 40 km of the overriding plate and the entire oceanic slab is taken to be elastic; although seismicity indicates that they incur permanent strain, this likely represents only a small fraction of the elastic strain variation during the earthquake cycle. Deeper parts of the overriding lithosphere and the asthenosphere are viscoelastic.

We completely lock the fault interface between earthquakes in the depth interval from 10 to 40 km depth (Tichelaar & Ruff, 1993)—the downdip end of the seismogenic fault thus coincides with the transition in the overriding lithosphere from elastic to viscoelastic. During earthquakes, this part of the interface accommodates both the seismic and aseismic part of the coseismic fault slip; that is, the seismic moment magnitude can in principle be smaller than the geodetic moment magnitude (although we recognize that joint source inversions are commonly successful in finding combinations of parameters that make the two identical (e.g., Weston et al., 2014). Model earthquakes repeat every 200 years (periodicity  $T = 200$  years) when we unlock this section of the interface and allow shear stresses to go to zero iteratively. Coseismic slip is thus 8 m, corresponding with  $M_w \sim 8.9$  (Papazachos et al., 2004). We relock the fault immediately after the event, in agreement with inferences that this happens shortly after the earthquake (Bedford et al., 2016; Tomita et al., 2017; Watanabe et al., 2014).

Observations of seismic anisotropy and laboratory results support that the mantle wedge has a power law viscoelastic rheology (Karato et al., 2008). This has the consequence that differential motion of the slab with respect to the mantle wedge is localized in a shear zone (Kneller et al., 2005), or subduction channel. We therefore represent the downdip part of the plate interface by a thin viscoelastic shear zone with an ultralow viscosity, that is, similar to Hu et al. (2016). The choice for a low viscosity is motivated by the effect that water has on viscosity; dewatering of the slab in combination with power law creep, for both of which there are abundant observations, results in a significant reduction of the viscosity particularly in the shear zone. Its model implementation is by slippery nodes (Melosh & Williams, 1989), a finite element technique to accurately incorporate differential slip across internal interfaces. Importantly, the shear zone responds

elastically during an earthquake. Immediately after relocking the seismogenic part of the interface, we allow slip on the deep shear zone. Given the high slip rates on the shear zone immediately after the earthquake, we iterate the solution until mechanical balance and zero shear stress is achieved. As we describe later when we compare our model results with observations, it is likely that slip on the deep shear zone lasts months to years. Our model assumption of instantaneous slip will, however, prove to be very useful because it helps us to isolate the role of the deep shear zone without introducing the additional time scale that would be associated with a more viscous material.

The shear zone determines the shear stress between the slab and the wedge. A slab velocity  $v_c$  imposes a shear strain rate on the deep shear zone above the slab that will be higher for a decreasing width  $W$  of the shear zone  $\dot{\epsilon}_{xy} = v_c/W$ . The shear stress is the product of the shear zone viscosity  $\eta$  and the shear strain rate

$$\sigma_{xy} = 2\eta\dot{\epsilon}_{xy} = \frac{2\eta}{W}v_c$$

In nature, the shear zone width results from strain (rate) localization and will depend on the viscosity contrast with the mantle wedge. Direct observations suggest that the shear zone width ranges from a few meters to tens of kilometers (Vauchez et al., 2012). A 2 times wider shear zone with a 2 times higher viscosity would result in the same shear stress between the two domains. For numerical convenience, our model implementation of a finite width shear zone is by an infinitely thin fault zone because this makes our results independent of the size of the finite elements in the shear zone. Given that we do not know any details about thickness and viscosity variations in the shear zone, we opt to use a uniform and constant value for the shear stress in the model. In the REF model this shear stress is set to zero. A consistent choice for the downdip length of the shear zone corresponds with the depth where the viscosity contrast with the mantle wedge disappears. Given our selection of an ultralow viscosity, our model shear zone therefore extends along the entire plate interface.

Away from the shear zone, stress variations are relatively small in the mantle wedge during the earthquake cycle. The viscosity of the bulk of the mantle wedge therefore is near linear, and we assume a Maxwell rheology here (Melosh & Raefsky, 1983). For the subslab asthenosphere, we select the same viscosity as the wedge; we do not expect the surface kinematics to be sensitive to this choice and we wish to keep the model as simple as possible. In the reference simulation, the Maxwell time (Glossary) of the viscoelastic wedge is about 8 years (see material parameters of the REF model in section A1). Throughout the paper we use  $\tau$  to refer to the Maxwell time.

The section of the megathrust interface updip of the locked section has no friction on it between earthquakes. During earthquakes, a constant resistive shear stress acts on the updip section of the subduction interface to represent a low kinematic friction in the REF model ( $2 \cdot 10^4$  Pa). This represents the brittle response of the shallow interface. Some coseismic slip can occur here in response to unlocking of the seismogenic portion of the fault. The coseismic friction controls whether coseismic slip occurs all the way to the trench or occurs as afterslip on the updip section of the fault.

### 2.3. Reference Model Results: Model 1

The imposed velocities on the slab edges result in increasingly large shear stresses on the locked portion of the subduction interface. Earthquakes occur in the model in response to complete unlocking of the seismogenic fault. Figure 3a shows the coseismic slip on the subduction interface during multiple (megathrust) earthquake cycles. Like similar geodynamic models (Hirahara, 2002), fault slip increases during subsequent earthquakes until it becomes equal to the accrued slip deficit after (roughly) the tenth cycle. The spin-up period serves to define a consistent pattern of prestresses (which we discuss below). Model earthquake cycles are self-similar after spin-up, and in the remainder of our paper we concentrate on the results of these “steady state earthquake cycles,” typically reached after 20 cycles.

#### 2.3.1. Coseismic and Primary Afterslip Stages

Displacement magnitudes due to the thrust earthquake (Figure 4a) display the typical lobe pattern in an elastic medium (Okada, 1992). Coseismic displacements are not symmetric (Sun et al., 2014); maximum displacements are 592 cm on the overriding plate and 208 cm on the downgoing plate; that is, ~74% of the slip occurs in the upper block. The overriding plate mostly lengthens during the earthquake—flexural deformation is a minor component. The typical aperture of a geodetic network on a convergent plate boundary ranges from

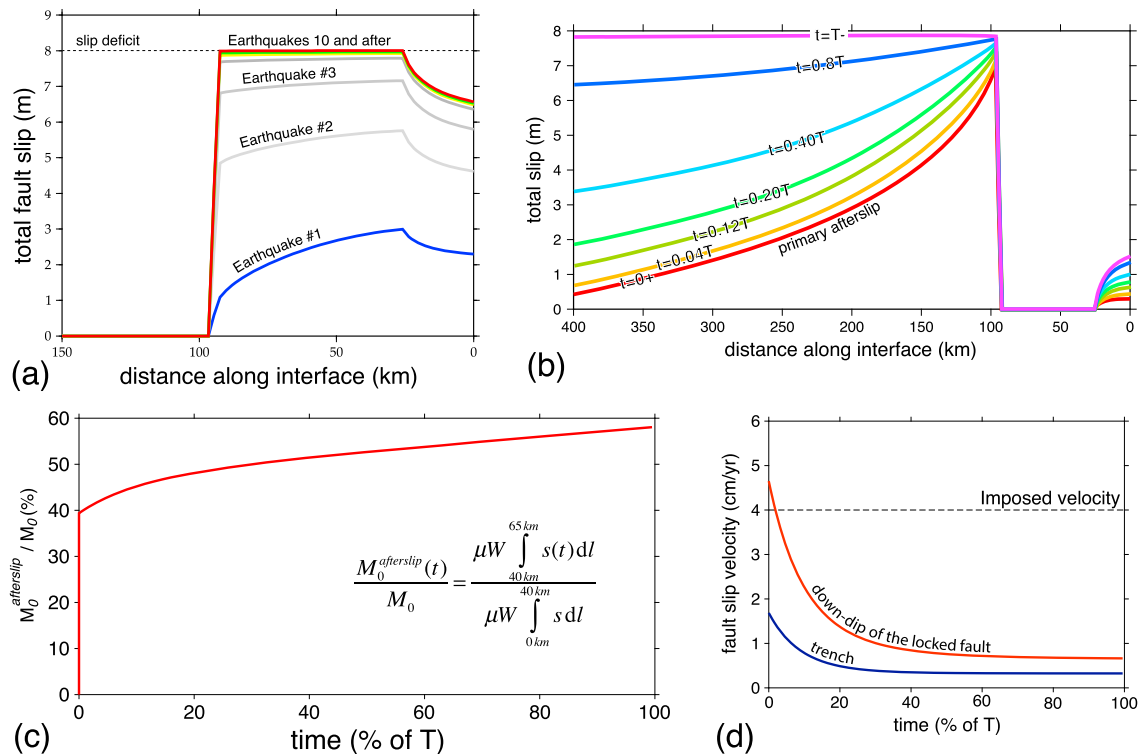


**Figure 3.** (a) Coseismic slip as function of the distance along the subduction interface from the trench. Coseismic slip increases during the first 10–15 earthquake cycles and remains constant and equal to the interseismic slip deficit of 4 cm/yr times 200 years = 8 m. During model spin-up, the prestress field is established. In our paper, we only discuss the results of the “steady state” 20th cycle. (b) Evolution of interseismic slip on the subduction interface as function of distance from the trench. The graphs illustrate that afterslip consists of relatively fast primary afterslip ( $t = 0+$  curve) followed by slower and transient secondary afterslip, and eventually by steady slip on the deep shear zone. Primary afterslip is possibly correlated with aftershocks. (c) Equivalent seismic moment corresponding with afterslip relative to the coseismic moment as function of time (as a fraction of the earthquake recurrence time  $T$ ) into the earthquake cycle. The coseismic moment is defined by the (coseismic) slip in the depth interval 0–40 km, and the “afterslip moment” by the depth interval 40–65 km. Primary afterslip amounts to ~40% of the coseismic moment, and secondary afterslip further increases the cumulative afterslip moment slowly to ~68% of the coseismic moment. (d) Slip velocity following the earthquake at two points along the subduction interface, at the trench, and at 30 km downdip from the locked fault where velocities are highest.

the coast to the volcanic arc, corresponding with horizontal positions of roughly –100 to –200 km for our 25° dipping slab.

Whether the earthquake results in coastal uplift or subsidence depends on the distance of the coast to the trench; the transition from coseismic uplift to subsidence (the “hinge line”) is located near the surface projection of the downdip end of the fault rupture. This was also observed following the 2004 Sumatra event (Meltzner et al., 2006).

With our assumption of a low-viscosity shear zone downdip of the locked segment, afterslip occurs instantaneously in the REF model; that is, negligible bulk viscous relaxation occurs in the mantle wedge during this initial afterslip (time  $t = 0 \times \tau$ , i.e., zero times the Maxwell time, so no viscoelastic mantle relaxation has occurred). This assumption helps us to discriminate two main ingredients of “afterslip”; first there is this fast slip on the interface that is solely driven by coseismic shear stresses, which we will refer to as “primary afterslip.” As we will discuss below, slower transient slip occurs subsequently on the interface due to viscoelastic relaxation in combination with plate motion (“secondary afterslip”). In the interseismic stage there is only plate motion driven steady slip, which is not afterslip.

Primary afterslip modifies the displacement field significantly (Figure 4b). This additional plate boundary localized postseismic displacement results from the mantle wedge overthrusting the oceanic slab. Primary afterslip results in significant surface uplift particularly between 50 and 200 km from the trench and thus likely involves coastal uplift in most regions.

Figure 3b shows the cumulative interface slip since the last earthquake. Primary afterslip is shown by the red ( $t = 0+$  curve). Primary afterslip is consistently driven by residual prestresses and coseismic stress

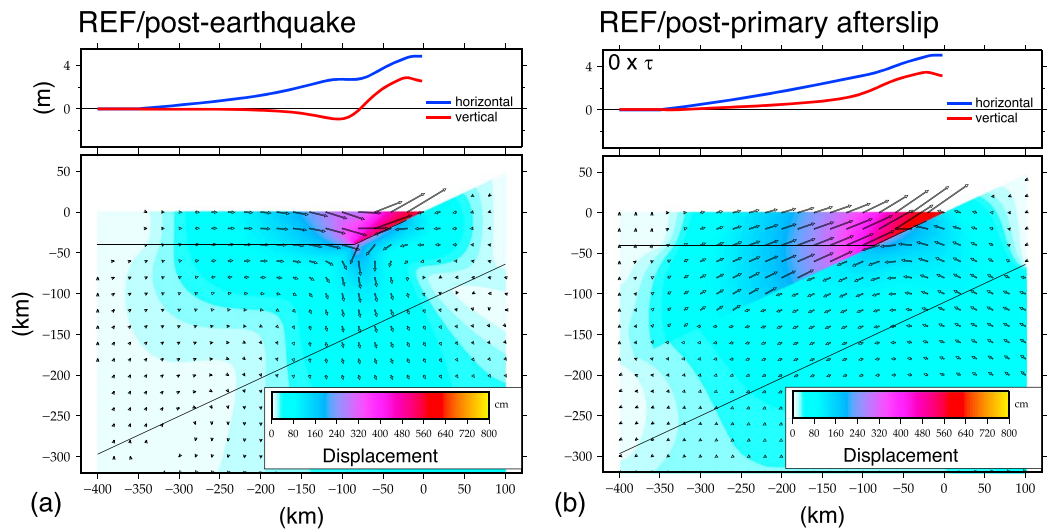


**Figure 4.** (a) Coseismic horizontal and vertical displacements of the surface (top) and total displacement field in the model domain (bottom). Coseismic displacements are calculated by subtracting displacements after coseismic slip from the displacements before the event. Positive horizontal displacements are directed trenchward. Upward (downward) displacements are positive (negative). The downdip section of the interface is a viscoelastic shear zone that remains locked during the earthquake. As a consequence, the displacement field is continuous here. (b) Displacements (including coseismic) after primary afterslip corresponding with the  $t = 0+$  curve in Figure 3b. Top panel shows a substantial change in particularly the vertical surface displacements. The bottom panel shows the deep shear zone as a displacement discontinuity.

changes; unlocking of the downdip and updip portions of the interface in our model removes shear stresses instantaneously.

Figure 3c shows the equivalent seismic scalar moment on the downdip section of the plate contact 40–65 km depth. Primary afterslip in our model amounts to ~40% of the coseismic moment.

The stress field immediately before the earthquake is shown in Figure 5a. It shows color contours of the “effective shear stress” (equivalent to the maximum shear stress and proportional to the octahedral shear stress) and is defined by

$$\sigma_E \equiv \sqrt{\left(\frac{\sigma_{xx} - \sigma_{yy}}{2}\right)^2 + \sigma_{xy}^2}$$

Arrows show principal stresses. This stress field was built during previous earthquake cycles. Horizontal stresses are compressive in most of the overriding plate. Viscous flow has relaxed shear stresses in the mantle wedge and in the subslab asthenosphere. The effective shear stress is highest near the downdip end of the locked fault, both in the overriding plate and in the slab.

A significant subhorizontal tensile stress is generated by the earthquake near the downdip end of the coseismic rupture, where displacement gradients are largest (Figure 5b). Green colors in the overriding plate above the fault show that shear stresses resulting from horizontal compression are substantially reduced by the earthquake.

Afterslip notably changes the stress near the downdip fault tip: the tensile stress decreases and (subhorizontal) horizontal compression increases (Figure 5c). Thrust movement of the mantle wedge in combination with no-displacement horizontal boundary conditions on the left side results in horizontal tension in the mantle wedge.

### 2.3.2. Postseismic and Interseismic Stages

Figure 6a shows the velocity field immediately after primary afterslip. Model velocities consist of three contributions: (1) continuing plate tectonic velocities (boundary conditions on left and right end of the slab), (2) viscoelastic relaxation in the mantle wedge and subslab asthenosphere, and (3) slip on nonlocked portions of the plate interface (Figure 3b).



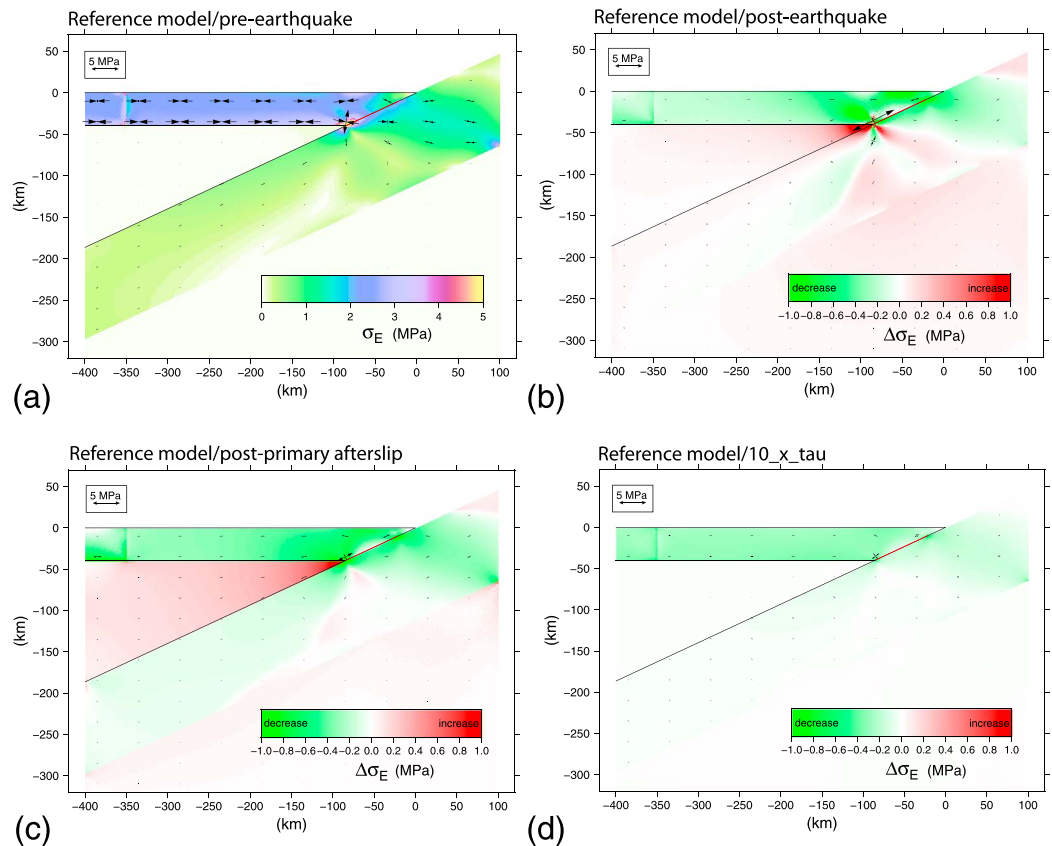


**Figure 5.** (a) Effective shear stresses (color) and principal stresses (arrows) immediately before the earthquake representing the prestress field resulting from many earthquake cycles. (b) Change in effective shear stress (color) and principal stresses (arrows) due to the earthquake. In most of the upper plate and in the shallow slab the effective shear stress decreases corresponding with  $< 1$  MPa subhorizontal tension. The stress pattern is more complicated around the downdip end of the coseismic fault where the step change in fault slip causes a lobe pattern of increased and decreased shear stresses. A significant tensile stress develops in the overriding plate directly above the fault tip. (c) Stress differences relative to the pre-earthquake state after reloading of the seismogenic fault and unlocking and primary afterslip on the rest of the interface. The most noticeable change relative to Figure 5b is that the signature of the downdip end of the coseismic fault has disappeared including the fault parallel tension, and that the effective shear stress has further increased in the viscoelastic wedge; (d) the change in effective shear stress in the wedge has gone back to zero after the postseismic period (here shown at time  $t = 10 \times \tau$ ).

Viscoelastic relaxation is particularly prominent in the mantle wedge shortly after the earthquake. Here, viscous strain rates are largest (up to a few times  $10^{-12}/s$ ) in the corner near the downdip edge of the seismogenic fault. Vertical to slab-perpendicular shortening is a response to slab-parallel extension during the earthquake. Its magnitude is primarily controlled by Poisson's ratio (assumed 0.25 here). Near-vertical (horizontal) velocities in the distal (proximal) mantle wedge are a consequence of this relaxation, with a clear expression in the elastic (flexural) beam on top of it. Significant horizontal surface motions are directed trenchward, even in the region near the trench, so that the actual plate interface reloading is (initially) not reflected in these motions.

The secondary afterslip velocity is initially high updip and downdip from the locked fault and decreases rapidly (Figure 3d). The slip rate on the deep shear zone is mostly less than the imposed plate velocity, except in the region downdip from the earthquake: here slip speeds are higher until  $t = 0.5 \times \tau$  (Movie S1 in the supporting information shows the evolution of velocities along the interface). Secondary afterslip on the downdip section of the plate contact increases from  $\sim 40\%$  of the coseismic moment to  $\sim 58\%$  before the next megathrust event (Figure 3c).

Slower viscoelastic relaxation in the mantle wedge results in reduced surface velocities at time  $t = 0.5 \times \tau$  (Figure 5b). Near the trench, the (landward) plate tectonic velocity now contributes slightly more to the

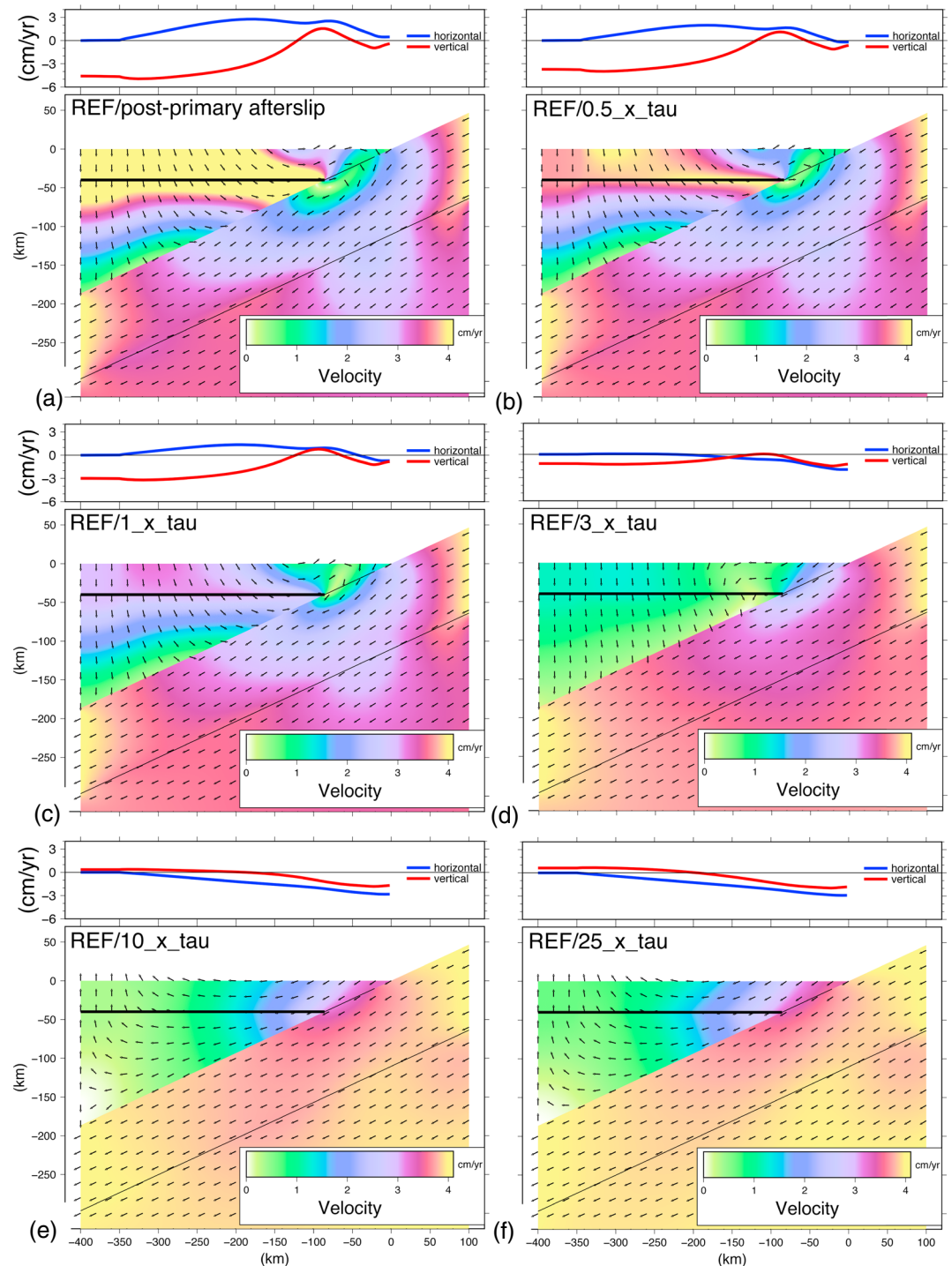


**Figure 6.** REF model velocities at (a) time  $t = 0 \times \tau$ , (b)  $t = 0.5 \times \tau$ , (c)  $t = 1 \times \tau$ , (d)  $t = 3 \times \tau$ , (e)  $t = 10 \times \tau$ , and (f)  $t = 25 \times \tau$ , which is right before the next megathrust event. Here  $\tau$  is the characteristic time for relaxation of shear stresses (Maxwell time) in the wedge and the subslab asthenosphere (Glossary and Appendix A). Arrows show directions and colors indicate velocity magnitudes. Top panels show horizontal (blue) and vertical (red) surface velocities. Positive (negative) horizontal velocities are directed trench (continent) ward. Upward (downward) velocities are positive (negative).

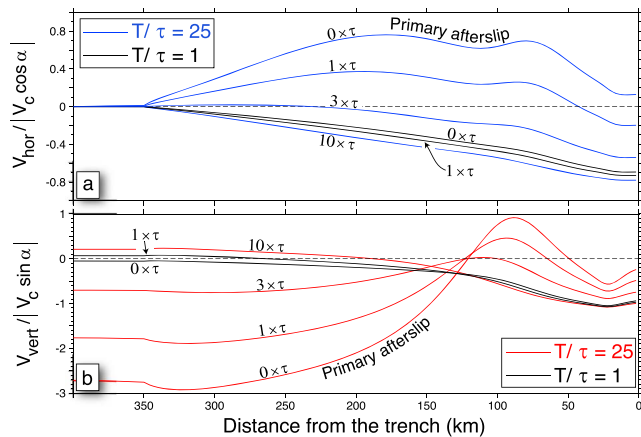


**Figure 7.** Surface velocity as function of horizontal distance at selected moments during the earthquake cycle (time as multiple of  $\tau$ ). The horizontal and vertical velocities are scaled by the corresponding component of the convergence velocity  $v_c$  (for subduction angle  $\alpha$ ). Results for the REF model (Model 1,  $T/\tau = 25$ , relaxed system), Model 2 (twice convergence velocity,  $T/\tau = 25$ ), and Model 3 ( $T/\tau = 25$ ) overlap and are represented by the red and blue lines. Black lines show the results of Model 4 for a small time ratio (unrelaxed system,  $T/\tau = 1$ ).

and viscoelastic relaxation, continent and down ward velocities represent shortening and flexure of the elastic overriding plate (Figures 6e and 6f). Eventually, horizontal velocities in the offshore forearc reach up to 75% of the imposed velocity, which is the combined result of subduction angle and interface locking distribution.

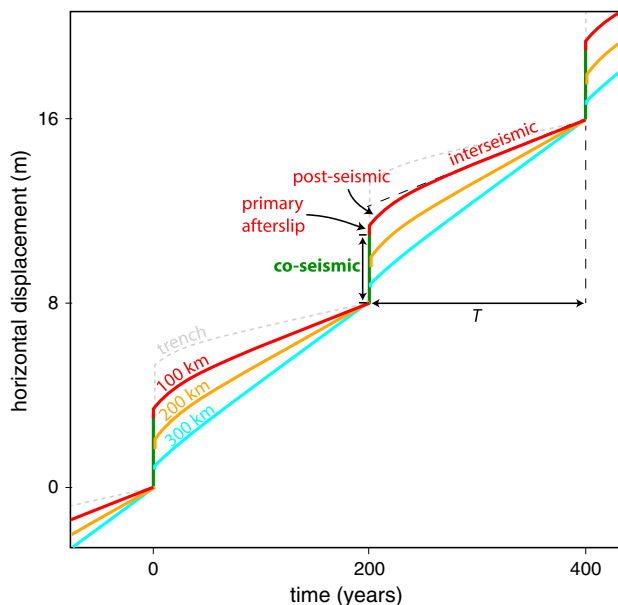


**Figure 8.** Evolution of horizontal surface displacements relative to the far-field oceanic plate for benchmarks located at the trench and at 100, 200, and 300 km distance from the trench. The coseismic displacement (green) is highest close to the trench. Displacements corresponding to afterslip also decrease with distance from the trench. The benchmark velocity (slope of the curve) is constant during the interseismic period. This velocity decreases during the postseismic period.

horizontal surface velocity than the (ocean ward) component of relaxation: the net horizontal velocity is somewhat negative (i.e., landward) here. Further inland, horizontal velocities are directed ocean ward still. Locking of the subduction interface results in downward velocities near the trench, whereas uplift reflects viscoelastic relaxation in the mantle wedge.

Figures 6c–6e show a diminishing contribution of viscoelastic relaxation. By  $t = 5 \times \tau$  the postseismic period is over as velocities in the triangle corner are oriented parallel down the slab due to interface locking near the down dip end of the seismogenic fault. Figure 6e shows a later stage where velocity gradients (i.e., strain rates) reflect continual stress relaxation because the plate tectonic loading rate is slower than the viscous relaxation rate. As a consequence, shear stresses are zero in the mantle wedge (Figure 5d). The back-arc subsidence reaches a maximum of 0.75 m at  $t = 5 \times \tau$ . The slip rate on the deep shear zone decreases exponentially on a somewhat longer time scale to a steady value (Figure 3c). In Figures 6c to 6e, the transition from trenchward to landward (positive to negative) of horizontal surface velocities is a convergence point. The convergence point migrates inland with time (Wang et al., 2012). The disappearance of ocean ward surface velocities signals the end of postseismic relaxation in the mantle wedge. After surface uplift rates wane, which was driven by secondary afterslip

Figure 7 summarizes the evolution of vertical and horizontal surface velocities. The velocities are relative to the far-field overriding plate and scaled by the vertical or horizontal component of the imposed convergence velocity. Horizontal surface velocities on the overriding plate (blue in Figure 7a) range from  $-1$  to  $1$ ; that is, they never exceed the imposed velocity during the postseismic phase. Initially they are directed opposite to the convergent motion, but as time progresses and the convergence point moves landward, increasingly large segments the overriding plate move parallel to, yet at a slower rate than, the imposed convergent velocity. Red curves in Figure 7a show normalized vertical velocities. Postseismic uplift rates in the trench coast region initially are nearly as large as the (downward) convergence component, and this uplift decreases to become subsidence after  $3\tau$ . Between 150 and 400 km from the trench, subsidence rates are initially higher than the vertical convergence component and decrease thereafter.

Horizontal displacements of the trench and of surface benchmarks at 100, 200, and 300 km from the trench are shown in Figure 8. Coseismic displacement (toward the trench) is indicated in green for the benchmark at 100 km. Primary afterslip further increases the trenchward displacement. During the postseismic period, horizontal velocities decrease until they reach a constant value during the interseismic period.

Our model differs in two critical aspects from most published multi-cycle models (e.g., Savage, 1983; Thatcher & Rundle, 1984). These earlier models are based on a fault in a horizontal elastic layer that

**Table 1**  
Overview of Numerical Models

Model number in the paper	Numerical model #	Change with respect to Model 1
Model 1 (reference model, "REF")	MC26	
Model 2	MC15	Convergence rate twice as high (8 cm/yr)
Model 3	MC14	$T = 2,000$ years, $\tau = 80$ years ( $T/\tau = 25$ , i.e., identical)
Model 4	MC32	$\tau = 200$ years so that $T/\tau = 1$
Model 5	MC33	Thickness of subducting plate half as thick (50 km)
Model 6	MC34	Slab dip angle reduced from $25^\circ$ to $20^\circ$
Model 7	MC29	Backstop location 300 km instead of 350 km
Model 8	MC31	Higher shear stress on deep shear zone
Model 9	MC42	Higher shear stress on shallow shear zone
Model 10	MC43	$T/\tau = 2.5$ and dip angle $30^\circ$ (Figure A1)

overlies a viscoelastic half-space; that is, they do not include an elastic slab and they do not include a viscoelastic shear zone. The coseismic response of our models is very similar, but surface displacements are substantially different following primary afterslip (Figure A1). Although the model response is again very similar toward the end of the earthquake cycle, the inclusion of an (inclined) slab and a shear zone in the model significantly affects the observational signature of the earthquake cycle.

The velocity field in the top 100 km is strongly affected by the triangular geometry of the mantle wedge, and by the restriction of the flow to the cross section. We expect the volume of the wedge to affect the duration of the postseismic period. These and other model-related sensitivities will be investigated in the next sections (see also Table 1).

#### 2.4. Sensitivity to Convergence Rate: Model 2

We first investigate the parameters that affect the progression of the cyclic earthquake model through the coseismic, afterslip, postseismic, and interseismic stages. We solve the mechanical equilibrium equation using strictly linear elastic and viscoelastic rheologies. Based on this, we might expect that a convergence rate that is twice as high would cause displacements, strains, velocities, and strain rates to be twice as large as in the REF model. As would be the case in a one-dimensional Maxwell model, we expect the length of the various stages to be insensitive to convergence rate. One possible deviation from this assumed behavior could be the fault segments, which constitute highly nonlinear mechanical elements, but we expect them to be well behaved in the context of regularly repeating earthquakes. We test linearity in Model 2 by increasing the convergence rate by a factor of 2. Like in the REF model, earthquakes occur every 200 years so that the slip deficit is twice as high as in Model 1 (the effect of changing the earthquake repeat time will be investigated in isolation below). Coseismic slip shows to be twice as large also. Overlapping velocities of Models 1 and 2 in Figure 7 illustrate that changing the convergence rate does not affect the time axis, that is, the duration of the individual stages during one cycle. The velocity magnitude is twice as large, confirming that the model response is linear. This shows that relaxation time does not depend on earthquake magnitude. The magnitude of surface displacements and velocities is directly coupled to the seismic moment.

#### 2.5. Ratio of Recurrence Time and Relaxation Time: Models 3 and 4

A well-established fact is that the mechanical response is sensitive to the ratio of characteristic loading (or repeat) time  $T$  and the characteristic unloading/relaxation time of the system  $\tau$  (Savage, 1983; Savage & Prescott, 1978; Thatcher & Rundle, 1979). The progression of the cyclic earthquake model through the coseismic, afterslip, postseismic, and interseismic stages is identical when  $T/\tau$  is the same. We test whether this holds for our models. In our REF model,  $T = 200$  years and  $\tau = 8$  years, so  $T/\tau = 25$ . In this next model (Model 3) we choose  $T = 2,000$  years and  $\tau = 80$  years ( $T/\tau = 25$ ). Figure 7 shows that horizontal velocities scaled by the convergence velocity are identical to those in, that is, overlap the curves of, the REF model. We thus conclude that the mechanical evolution of models with the same  $T/\tau$  is identical.

Any estimate of the time ratio for real subduction zones is bound to be approximate, first because major earthquakes occur irregularly and second because viscosity estimates depend strongly on the model that is used for postseismic relaxation. In the region of the 2004  $M_w = 9.2$  Sumatra-Andaman earthquake, the

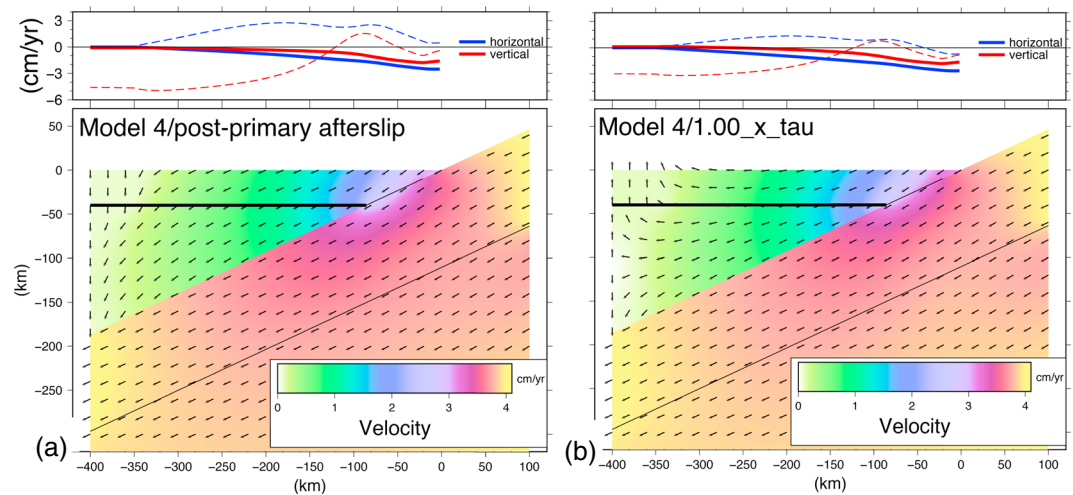


**Figure 9.** Velocities for Model 4 ( $t/\tau = 1$ ) at a) time  $t = 0 \times \tau$ , and b)  $t = 1 \times \tau$ . Dashed lines in the upper panels represent surface velocities of the REF model at  $t = 0 \times \tau$  and  $t = 1 \times \tau$ . Postseismic relaxation is close to absent in Model 4, and surface velocities correspond with interseismic convergence at all times.

last previous event of similar magnitude likely occurred around 1450 CE (Meltzner et al., 2010). We therefore estimate  $T = 600$  years here. The long-term Maxwell time  $\tau$  of the mantle wedge was estimated at 5 years from a viscoelastic model using spherical symmetric layering (Broerse et al., 2015) as well as from a model including a realistic slab geometry (Hu & Wang, 2012). For the Sumatra-Andaman section of the plate contact we thus arrive at an estimate of  $T/\tau = 120$ ; that is, the viscoelastic part of the system has no memory of previous earthquakes when a large event occurs because coseismic stress changes in the mantle wedge have completely relaxed. In our REF model (for time ratio 25), we find that the coseismic stresses had relaxed after 5 Maxwell times (Figures 5c–5e), so we expect the REF model to behave similar to a model for larger time ratios.

The plate boundary segment involved in the 2010  $M_w = 8.8$  Maule (Chile) event was previously active in 1835 (Darwin, 1846). Aron et al. (2015) estimate a recurrence range of 84–178 years for the megathrust cycle. The long-term Maxwell time ranges between 5 and 70 years (Ding & Lin, 2014; Piersanti, 1999). For this part of the Chilean margin  $1 \leq T/\tau \leq 36$ . The lower bound indicates that stress relaxation of previous events is still ongoing when a new event occurs. This type of behavior will be the focus of the next set of models. We investigate the evolution for a time ratio at the lower end of the spectrum:  $T/\tau = 1$  in Model 4.

Like in the REF model, the slip deficit of 8 m is resolved in Model 4 during the earthquake. The coseismic partitioning of the differential motion on lower and upper block is very similar to that of Model 1. Primary afterslip is also the same. Immediately after primary afterslip (Figure 9a), model velocities are, however, distinctly different from the REF model at this stage, and hardly different from velocities right before the next earthquake (Figure 9b). Surface velocities correspond with interseismic convergence at all times and are similar to late-stage velocities of the REF model (Figure 7). Postseismic relaxation is thus close to absent. This demonstrates that the time ratio  $T/\tau$  has a first-order influence on the mechanical response during the megathrust cycle, and on its geodetic expression.

## 2.6. Influence of the Thickness of the Oceanic Slab: Model 5

Elastic strain is stored in the subducting plate between earthquakes. In our REF model we use a relatively thick oceanic slab: 100 km, corresponding with an oceanic age of  $\geq 100$  Myr. Here we investigate the influence of the thickness/age of the slab by assuming a 50 km thick oceanic lithosphere, which corresponds with an oceanic age of  $\approx 20$  Myr (Doin & Fleitout, 1996). All other geometric and material parameters are identical to the REF model.

The coseismic slip partitioning between upper and lower block, and the surface response is similar to the REF model (Figure 10). Fault slip results in an increase of the effective shear stress near the downdip end of the



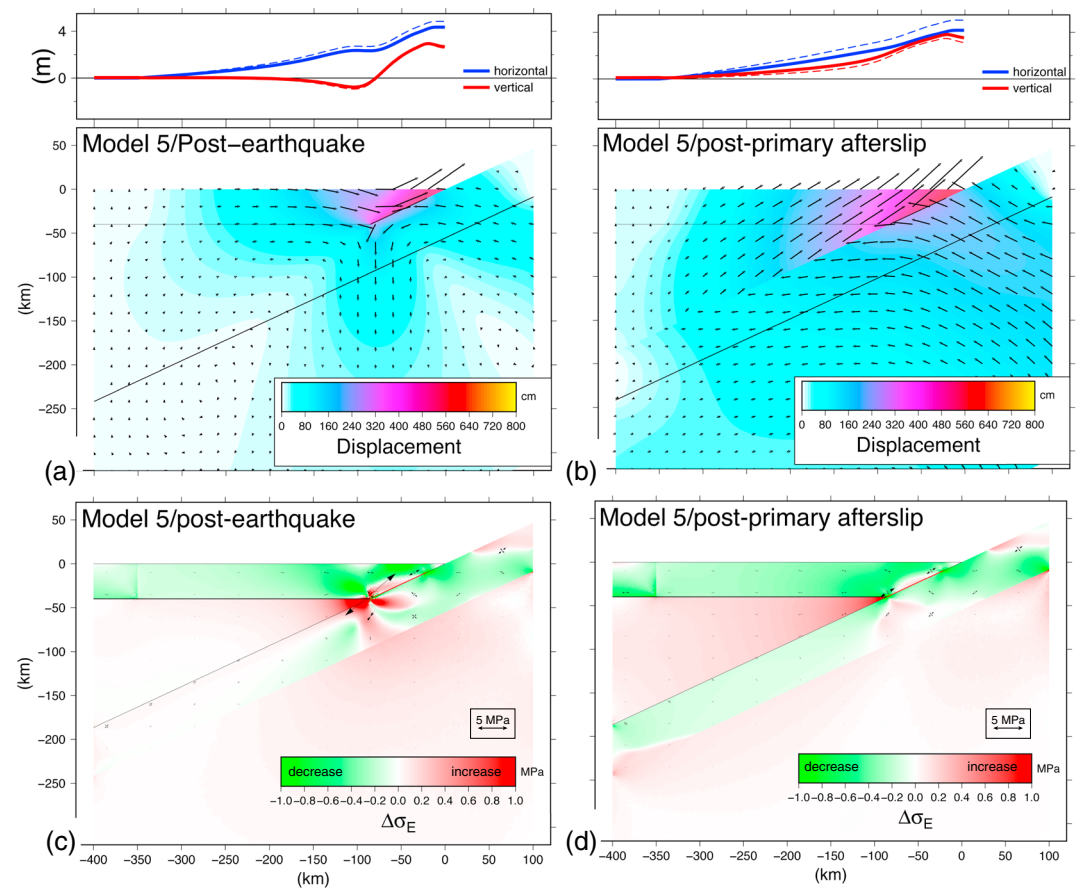


**Figure 10.** Model 5 has a 50 km thick slab, that is, half the thickness of the slab in the REF model. (a) Coseismic displacement field. The top panel shows surface displacements of Model 5 with solid lines and of Model 1 with dashed lines, showing that only horizontal displacements near the trench are slightly less for a thinner slab. (b) Displacement field following primary afterslip, showing that horizontal surface displacements persistently are smaller than in the REF model. A comparison with Figure 5b shows substantial differences in and below the slab also. (c) Coseismic changes in effective shear stress  $\sigma_E$  are markedly higher in Model 5 (cf. Figure 5b). (d) Changes in effective shear stress (relative to pre-earthquake) after primary afterslip has taken place. The stress changes are lower than in the REF model (Figure 5c), and the maximum  $\sigma_E$  is similar.

seismogenic fault by 25.8 MPa, much more so than in the REF model (11.4 MPa). The slab and subslab asthenosphere move more during primary afterslip than in the REF model (cf. Figure 10b with Figure 4b), and the overriding plate moves less; that is, the slip partitioning between the upper and lower plates is somewhat more symmetric.

The contact area between the upper part (overriding plate and mantle wedge) and the slab in Model 5 is identical to Model 1. In between earthquakes, the resistive force to differential motion exerted by the upper part of the system on the slab is the same as in the REF model and so must be the total driving force on the slab. This force is concentrated in a thinner section in Model 5, so that slab stresses are higher (Figures 10c and 10d). Higher slab stresses contribute to higher shear stress on the deep shear zone, in particular on the updip end in the corner of the mantle wedge. This is why there is more primary afterslip in the thin-slab model.

The slab in Model 5 is more pliable than that in the REF model. The shear traction by the overriding beam attempts to flex the slab into an upward concave form. The resulting slab bending is very sensitive to the location where boundary conditions are imposed on the slab. In the slab beneath the wedge, slab-perpendicular velocity components indicate unbending during the postseismic phase, and rebending after that (Figure A2). Surface velocities are consequently significantly different from the REF model. In their corrections for postseismic relaxation, workers should thus account for slab bending imprints on surface signals also.

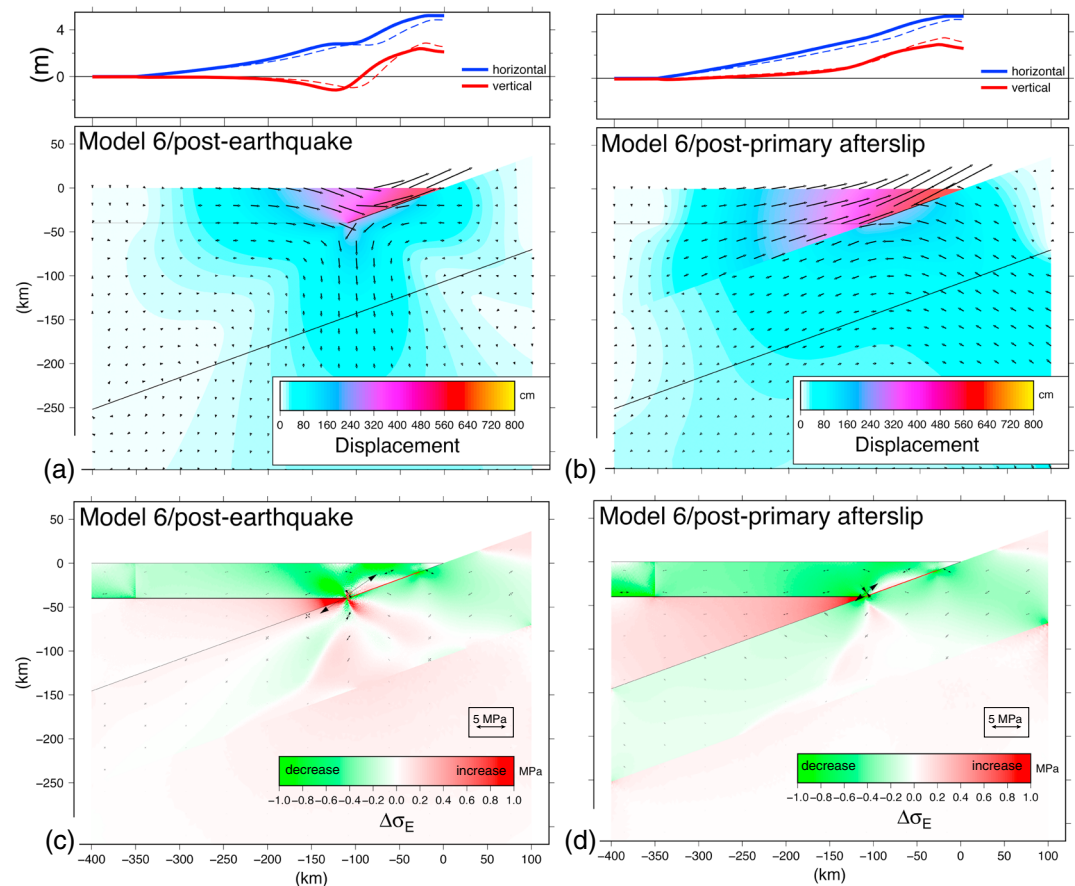


**Figure 11.** The dip angle of the slab in Model 6 is  $20^\circ$ , which is shallower than in Model 1 ( $25^\circ$ ). (a) Coseismic displacement field. Horizontal and vertical surface displacements are displayed in the top panel (solid lines = Model 6, dashed lines = REF model). (b) Displacements since beginning of the last earthquake when both the earthquake and primary afterslip have taken place. (c) Coseismic change in effective shear stress, green where  $\sigma_E$  decreased due to the earthquake, and red where it increased. (d) Change in effective shear stress relative to the beginning of the last earthquake after primary afterslip.

## 2.7. Influence of the Slab Dip Angle: Model 6

The dip angle is reduced to  $20^\circ$  in Model 6. The downdip end of the locked fault is kept at 40 km depth, so the surface area (moment magnitude) is 24% higher than in the REF model. More importantly, the horizontal coordinate of the downdip end of the locked fault sits 24 km further from the trench. The shifted location of the downdip fault is clearly expressed in the coseismic surface displacements of Model 6 when compared with the REF model (Figure 11a). Following primary afterslip, this footprint has disappeared from the surface displacements (Figure 11b), which now mostly show a pronounced horizontal displacement and slightly reduced vertical displacement relative to the REF model. The different partitioning of the interface slip between horizontal and vertical components results in a stronger tensile stress in the overriding plate above the downdip end of the coseismic fault (cf. Figure 11c with Figure 5b). A shallower fault dip thus facilitates more complete coseismic extension of the overriding plate. Like in the REF model, the tensile stress is reduced following primary afterslip (Figure 11d).

In Figure 12 we compare surface velocities of Model 6 with those of the REF model. The horizontal (vertical) velocities are scaled by horizontal (vertical) components of the imposed convergence velocity. Shortly after the earthquake and primary afterslip, normalized horizontal velocities are significantly lower than in the REF model. The postseismic extension rate of the overriding plate is lower because the coseismic extension was higher, which leaves the upper plate more relaxed at the beginning of the postseismic period. Differences between the models decrease with time. Vertical postseismic displacements of the surface (Figure 12b) mostly represent the translation of the wedge tip of Model 6 toward the left. Amplitude differences with

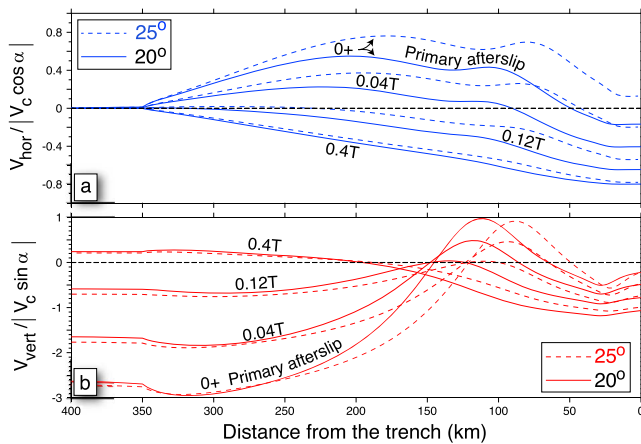


**Figure 12.** Normalized (a) horizontal and (b) vertical surface velocities (like Figure 7) at different stages of the postseismic period: time = 0+ is after primary afterslip, time = 0.04 T (= 1 $\tau$ ), time = 0.12 T (= 3 $\tau$ ), and time = 0.4 T (= 10 $\tau$ ). Solid color curves for Model 6 (20° slab dip angle) dashed color curves for the REF model (25°).

respect to Model 1 are much less. These differences also decrease with time into the cycle. The dip angle of the seismogenic fault thus clearly affects the surface expressions, both coseismically and during the post-seismic phase. We return to this below when we compare our models with observations.

## 2.8. Influence of the Horizontal Distance to the Backstop: Model 7

We put the backstop 100 km closer to the trench in Model 7, at 250 km (350 km in the REF model). Horizontal surface displacements due to the earthquake and primary afterslip are restricted to the region between the trench and the backstop; horizontal displacement at trench is similar to the REF model, but it decreases more rapidly going away from the trench. Vertical displacements are hardly affected. Figure 13 shows surface velocities at various instances during the postseismic period. The convergence point (where horizontal velocities change sign) migrates faster to the backarc in Model 7. Vertical (horizontal) velocities are initially significantly higher (lower) in the near trench region. Sinking rates are higher between 150 and 250 km, and lower further inboard. It is clear that both the horizontal extent and the magnitude of horizontal and vertical surface velocities are substantially affected by the backstop location.

## 2.9. Shear Coupling Between the Slab and the Mantle Wedge: Model 8

For the deep shear zone in the REF model the shear stress between the wedge and the slab was set to zero. In Model 8 we impose a moderate shear stress (0.3 MPa) between the slab and the wedge. Like in the REF model, the wedge viscosity is  $5 \cdot 10^{18}$  Pa s, so the equivalent viscosity of the shear zone should be lower than that. It follows from the above relation that a shear zone viscosity of  $5 \cdot 10^{17}$  Pa s would require a shear zone thickness of 4.2 km to generate a shear resistance of 0.3 MPa, which are all reasonable numbers.

Stronger shear coupling across the deep shear zone has little effect on the primary afterslip (Figure A3). Secondary afterslip is, however, significantly reduced relative to the REF model. Wedge material is dragged downward with the slab (visible in the later stages of the earthquake cycle, Figure A3). However, the surface response (displacement, velocity) of Model 8 is very similar to the REF model. In other words, surface observations are expected to be insensitive to shear coupling on the deep shear zone.

## 2.10. Friction on the Shallow Section of the Interface: Model 9

The coseismic kinematic friction on the shallow, updip section of the subduction interface was selected relatively low so that significant slip occurred here during the earthquake (Figures 3a and 4), that is, consistent with evidence of tsunami generation in that region. In Model 9 we impose a high coseismic friction on the shallow interface. Low interseismic friction is maintained, so we are mimicking a form of coseismic velocity strengthening in this model. The coseismic slip on the updip interface is greatly reduced (Figure A4) resulting in differences in local trench uplift near the trench, and in the regional horizontal displacements (Figure 14). Primary afterslip on the shallow interface is larger and compensates exactly for the coseismic slip reduction. As a consequence, both the surface displacements and velocities are identical to the REF model after primary afterslip has occurred. Friction on the updip section of the interface thus does not affect the geodetic signature of the earthquake cycle notably.

## 2.11. Mechanical Properties

Additional model experiments (Appendix A) show the following. Regarding the elasticity of the overriding plate, an increase of Poisson

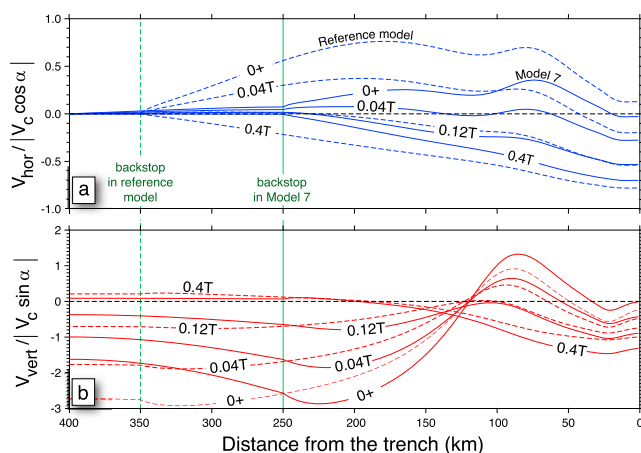


**Figure 13.** Normalized (a) horizontal and (b) vertical surface velocities (like Figure 7) at different stages of the postseismic period: time = 0+ is after primary afterslip, time = 0.04 T (= 1 $\tau$ ), time = 0.12 T (= 3 $\tau$ ), and time = 0.4 T (= 10 $\tau$ ). Solid color curves for Model 7 (backstop at 250 km distance from the trench) dashed color curves for the REF model (backstop at 350 km).

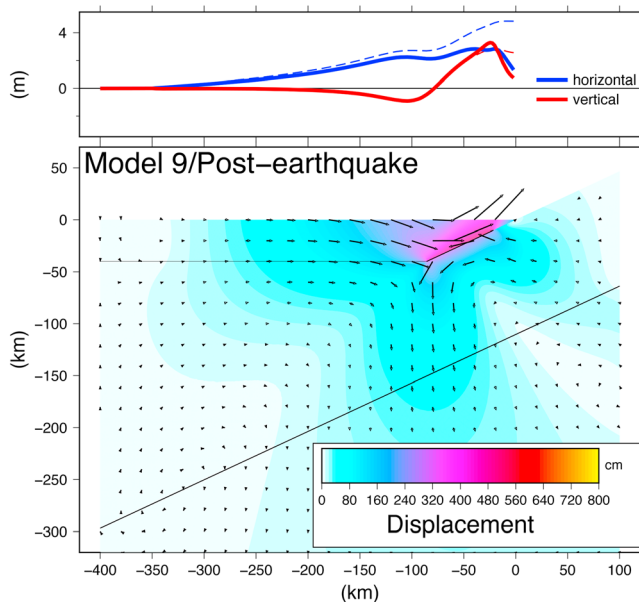


**Figure 14.** Coseismic displacements for Model 9, which has higher kinematic friction on the updip interface during the earthquake than the REF model. Horizontal surface displacements (top panel) differ from the REF model (dashed); vertical surface displacements are identical except within the first 20 km from the trench.

ratio from 0.25 to 0.45 (i.e., nearly incompressible elasticity) and a simultaneous decrease of Young's modulus (from 50 to 42.5 GPa) such that the flexural rigidity is preserved yield similar horizontal surface displacements, and smaller vertical displacements than the REF model. Increasing both the Young's modulus and the viscosity in the mantle wedge and subslab asthenosphere by a factor of four gives identical results. The results are largely insensitive to the elastic bulk modulus of the wedge and subslab asthenosphere. Increasing the subslab viscosity by a factor of 10 (e.g., Hu et al., 2004) does not affect the surface expressions.

### 3. Interface Coupling From Inversion

Formal inversion of surface displacements observed by geodetic arrays is commonly used to resolve slip and locking patterns on the subduction interface based on the back slip hypothesis (Savage, 1983). We use the (full) synthetic surface velocities from our REF model to test what aspects of actual model interface slip is recovered by such inversions. We follow the common assumptions for interseismic coupling inversions; the only source of surface deformation is slip on the interface and the deformation occurs in an elastic half-space (e.g., Loveless & Meade, 2016; Metois et al., 2016; Tsang et al., 2015). Here the downdip length of the interface is divided into  $N$  subfaults. The velocity  $\mathbf{v}$  at surface coordinate  $\mathbf{x}_i$  of the  $i$ th benchmark resulting from the slip velocity  $\dot{\mathbf{s}}_j$  on the  $j$ th subfault with coordinate  $\mathbf{y}_j$  is given by the observation equation

$$\mathbf{v}(\mathbf{x}_i) = \sum_{j=1}^N \dot{\mathbf{s}}_j \mathbf{G}_{ij}(\mathbf{x}_i, \mathbf{y}_j)$$

where  $\mathbf{G}_{ij}$  are the Green's functions for dislocations in an elastic half-space (Okada, 1992). The 2-D mechanical model represents a cross section through the subduction margin that experiences megathrust earthquakes. The inversion is based on 3-D, so we extend the subduction fault by 400 km in the along-strike direction, that is, so far that the central part of the slip solution is insensitive to lateral edge effects. The least squares minimization of differences between benchmark and analytic velocities takes the form of a simple linear matrix equation that we solve using the Linear Algebra Package (LAPACK) subroutine *dgels* (Anderson et al., 1999). The resulting solution  $\dot{\mathbf{s}}_j$  is unstable unless regularization is applied; we add damping to minimize the model length (Levenberg, 1944) and Laplacian smoothing to minimize the slip difference between adjacent subfaults (Constable et al., 1987). The damping and smoothing weighting coefficients are chosen by visual inspection of the resulting solution and the corresponding fits between modeled and inverted velocities.

The inversion results in Figure 15 are based on the assumptions that the data are noise free, and that a sufficiently dense geodetic network exists from the trench to far in the backarc. At time =  $0.25\tau$  (Figure 15a), the input surface velocities are poorly fit by the inverted velocities. The inverted slip pattern (red bars) is highly dissimilar from the slip pattern in the model (green line). A similar result is seen after one relaxation time (Figure 15b). The fit of the inverted surface velocities to the synthetic velocities is somewhat improved but still lacking. The inversion suggests partial locking on the fully locked part of the interface (blue). The back slip rate smaller than the plate convergence rate in the updip part of the interface; although the interface is mechanically free, the result illustrates the stress shadow effect (Hetland & Simons, 2010). From these time slices it is thus clear that postseismic relaxation obscures the slip velocities on the shallow subduction interface. Locking would be significantly underestimated based on inversion results during the postseismic relaxation phase. This was already suspected for various subduction zones, for example, the Ecuador-Columbia subduction zone (White et al., 2003). Slip on the deeper part of the interface is also not recovered.

The next two time slices are taken toward the end of the postseismic relaxation phase of the earthquake cycle ( $3\tau$ , Figure 15c) and well after that time ( $5\tau$ , Figure 15d). At these times, surface velocities are reasonably well

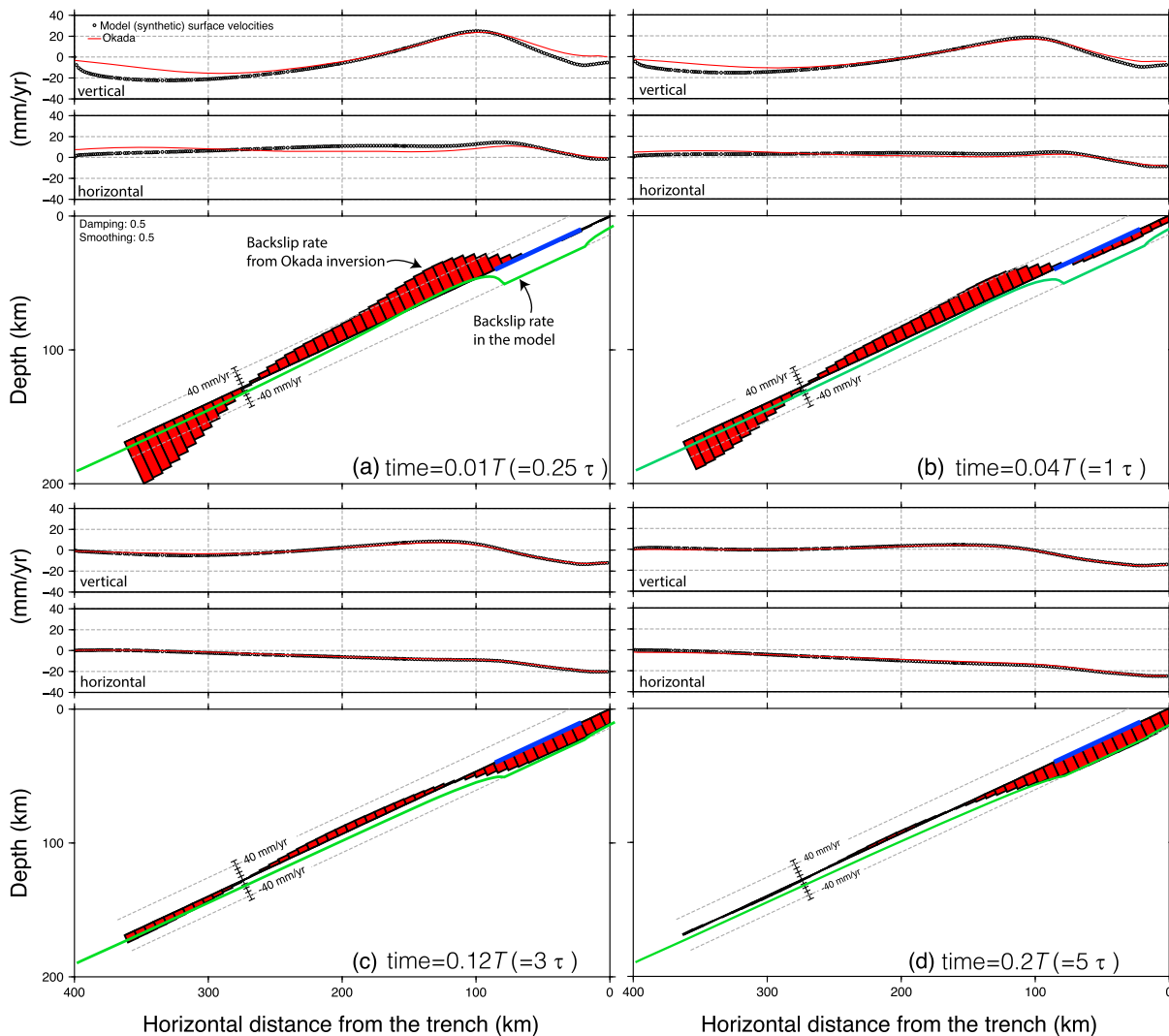


**Figure 15.** Results from an inversion (using Okada, 1992 Green's functions) of the synthetic horizontal and vertical velocities of the REF model (Model 1). The aperture of the network is highly idealized, with a dense network of benchmarks from the trench to very far in the backarc. Also, the synthetic data are noise free. (a) Time = 0.01  $T$ . Top (middle) panel shows vertical (horizontal) velocities of Model 1 (black dots) and the synthetic velocities produced by the back-slip inversion (red line). The bottom panel shows the inverted interface slip rate (red bars) and the actual interface slip rate in Model 1 (minus the back slip rate of 40 mm/yr, green line). Ideally, the red bar diagram would follow the green line but full locking of the coseismic fault (blue line) is clearly not reproduced as 40 mm/yr back slip by the inversion. (b) Time = 0.04  $T$ . (c) Time = 0.12  $T$ . (d) Time = 0.2  $T$ . After the postseismic period ( $5\tau$  and thereafter) the back slip rate on the updip and locked parts of the interface are well reproduced by the inversion. Back slip on the deep interface below the locking depth is never correctly reproduced.

fit by the inversion. Inverted slip velocities (red blocks) on locked and updip parts of the interface agree with interface slip rates in the mechanical model (green line). Inverted interface slip rates also agree immediately below the locked section. Slip velocities on deeper parts of the interface, which are lower than the convergence velocity, are poorly recovered by the inversion.

Differences between interface slip rate (green lines in Figure 15) and locking (blue lines) are particularly large updip of the seismogenic part of the interface and illustrate that fault slip rates as inverted from surface kinematics are loosely connected to fault friction properties (Wang & Dixon, 2004). If the slip deficit updip of the locked fault would be interpreted as mechanical coupling, friction would be overestimated based on the inversion results.

The rheology of the REF model differs significantly from the elastic half-space model that is used in the inversions. The relevant difference during the interseismic phase is that the overriding plate in the REF model corresponds to a horizontal elastic beam that is subject to a shear traction on the locked section of the interface.



One consequence is that horizontal surface velocities produced in an elastic half-space model with an equivalent interface slip distribution are reduced by 10–15% relative to those from the REF model but have the same linear decrease in magnitude from the trench to the backstop. Vertical velocities differ more starkly; in the elastic half-space model they are broadly downward, whereas those in the REF model change from subsidence near the trench to uplift at greater distances. Therefore, inversions based on elastic half-space Green's functions that weigh horizontal and vertical velocities equally may produce artifacts in the interface slip distribution.

It is important to recollect the result from our Model 4 (Figures 7 and 9) here, namely, that the surface velocities are highly dependent on the ratio of cycle time  $T$  and the relaxation time  $\tau$ . Postseismic relaxation has a smaller footprint when this time ratio is small, and the locking pattern above the deep shear zone therefore becomes apparent immediately following primary afterslip.

Actual geodetic networks are often restricted to the region from the coast to the volcanic arc. Inversion of synthetic surface velocities with limited aperture (50–200 km) does not affect our conclusion that interface slip velocities in the updip, and locked sections of the interface can be recovered well later in the cycle after postseismic relaxations have substantially decayed (Figure A5). Inferences of locking during the postseismic phase are more difficult in that they require an accurate model of the postseismic imprints.

#### 4. Comparison With Observations

In this section we review observations made at different stages of the earthquake cycle at convergent margins and compare these observations with our REF model. We will show a strong agreement between observations and models (when appropriately scaled). This demonstrates that although simple, our model captures the first-order processes at depth. Consistent with our approach thus far, we focus on margins that have experienced large events, which are in different parts of the earthquake cycle, and for which the observations conform to modern standards.

##### 4.1. Megathrust Events

The Valdivia (southern Chile) earthquake of 22 May 1960 was the largest instrumentally recorded event with a seismic moment magnitude of  $M_w$  9.5 (Kanamori, 1977). The event ruptured ~1,000 km of strike length of the subduction interface, which had shown relatively low seismic activity during the period 1906–1944 (Gutenberg & Richter, 1954) and where destructive earthquakes had occurred during the post-Columbian period (Lomnitz, 2004). There is some evidence that the 1960 Chile earthquake was preceded by a slow-slip event of comparable moment (Cifuentes & Silver, 1989). Plafker and Savage (1970) report 155 vertical displacements along the coast that were acquired in 1968. A limited set (20) of coastal uplift data acquired immediately after the event were insufficiently accurate, yet “reasonably consistent” with the 1968 measurements. Inland elevation differences were obtained from differencing a 1957–1959 leveling line along the Inter-America Highway with observations in 1963–1964 at the same benchmarks. Moreno et al. (2009) invert the observations for coseismic slip. Similar to Barrientos and Ward (1990), they find that most of the slip (>25 m) occurred between 38°S and 42°S.

The  $M_w$  9.2 Prince William Sound (Alaska) earthquake of March 27 1964 ruptured 600–800 km of the margin. Most of the moment release resulted from up to 20 m of slip on two separate asperities (Christensen & Beck, 1994; Ichinose et al., 2007; Suito & Freymueller, 2009). Leveling and tide level measurements in the months after the earthquake (Plafker, 1972) show significant uplift near the trench, and subsidence further inboard. Horizontal displacements were calculated from triangulation data by Parkin (1972) and reanalyzed by Snay et al. (1987). Initial triangulations were done on 196 benchmarks from 1901 to 1961 (147 benchmarks after 1940; network details in Holdahl & Sauber, 1994). Postearthquake surveys were done in 1964–1965. Horizontal displacements were specified relative to Fishhook (149.23°W, 61.72°N). Data west of 150°E are suspect (Snay et al., 1987), and there are possibly systematic biases (Suito & Freymueller, 2009).

The 26 December 2004  $M_w$  9.2 Sumatra-Andaman earthquake extended >1,300 km along the margin. Coseismic displacements in excess of 20 m were recorded seismically (Ammon et al., 2005; Lay et al., 2005) and by continuous Global Navigation Satellite Systems (GNSS) stations in the far field (Vigny et al., 2005). A massive tsunami was generated by coseismic slip (Chlieh et al., 2007). Near-field observations included both coseismic and postseismic deformation during 1 to 2 months after the earthquake. Initial afterslip was

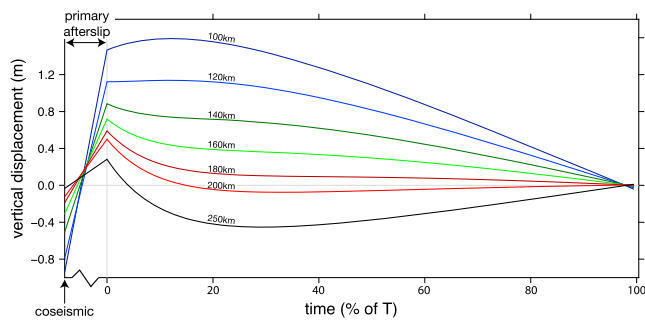


**Figure 16.** Evolution of vertical surface displacements at different distances from the trench from Model 1. Coseismic displacements are downward, and substantially larger close to the trench (e.g., 100 km distance, blue curve) than further away. Afterslip results in uplift. Stations within 180 km from the trench gradually subside to zero right before the next earthquake (time = 100% of the cycle time  $T$ ). Stations at larger distances sink to a net subsidence that is recovered by rising of the surface after the postseismic relaxation phase from time =  $0.4 T$  ( $= 10\tau$  in this model) onward.

particularly significant in the Andaman and Nicobar Islands (Banerjee et al., 2007; Bilham et al., 2005; Gahalaut et al., 2008; Subarya et al., 2006). Afterslip continued here 2008.5–2010.5 (Paul et al., 2012). Far-field observations of geodetic motions (Broerse et al., 2015; Satirapod et al., 2013) and gravity changes (Broerse et al., 2015; Han et al., 2008; Hoechner et al., 2011; Panet et al., 2010) find that (bulk) relaxation in the upper mantle has commenced.

The Maule (Chile)  $M_w$  8.8 earthquake of 27 February 2010 occurred along the Nazca-South America subduction margin. Coseismic slip was concentrated in two patches on the  $\sim 500$  km long interface with a maximum of 19 m coseismic slip on the northern patch (Delouis et al., 2010; Lorito et al., 2011; Pollitz et al., 2011). Before the earthquake, horizontal GNSS velocities decreased roughly linearly away from the trench which was interpreted to indicate complete locking (Ruegg et al., 2009). Sustained trenchward motions during the first 5 years after the event are interpreted to result from afterslip and bulk viscous relaxation (Klein et al., 2016).

The Tohoku (Japan)  $M_w$  9.0 earthquake that occurred on 11 March 2011 was the result of slip on a compact, 300 km long rupture on the interface of the Pacific and North American plates. Estimates for the maximum slip are in the 40–60 m range (Ammon et al., 2011; Koketsu et al., 2011; Lay et al., 2011), where especially seismological and tsunami data indicate that the rupture continued to the trench (Hooper et al., 2013; Ide et al., 2011). The earthquake has been well recorded, where the dense GEONET GNSS network in Japan enables a good view on the interseismic, coseismic as well as postseismic surface displacements on land. Notably, GPS/acoustic seafloor positioning provides a view on the near-field displacements that indicate landward motions in the early postseismic phase (Tomita et al., 2017; Watanabe et al., 2014). Whereas early postseismic GNSS displacements have often been attributed to afterslip only (e.g., Johnson et al., 2012; Ozawa et al., 2011), more recent studies indicate the necessity for a large contribution from bulk viscous relaxation of the mantle (Freed et al., 2017; Hu et al., 2016; Sun et al., 2014; Yamagiwa et al., 2015).

## 4.2. Coseismic Surface Displacements

### 4.2.1. Uplift and Subsidence

The relative magnitude of coseismic coastal subsidence decreases with the distance of the coastline from the trench; however, the actual magnitude of the vertical motions is dominated by earthquake magnitude. Figure 16 shows the uplift/subsidence evolution for our REF model for various horizontal distances (corresponding with the range of coastal distances) from the trench. It shows that coseismic subsidence (or uplift) depends strongly on the distance from the trench (Savage & Hastie, 1966).

In order to compare our model results with observations, we need to address that our REF model results are obtained with a constant ( $25^\circ$ ) slab dip angle, and the characteristics dip of actual subduction zones varies. It is well established that vertical displacements in the forearc region are particularly sensitive to slab dip angle (e.g., Moreno et al., 2009). We therefore apply a simple near-field correction to our model results, as follows. A real slab dips with an angle  $\alpha$  ( $10^\circ$ – $15^\circ$ ) from the trench so that the top of the slab is located at depth  $d$  beneath the coast. The coast is located at a horizontal distance 80–250 km from the trench. The model slab top reaches that depth over a much shorter horizontal distance. To correctly locate the interface beneath the coast, we scale the horizontal model axis by  $\tan(25^\circ)/\tan(\alpha)$ .

Figure 17a shows coseismic uplift and subsidence for the 2004 Sumatra earthquake (Chlieh et al., 2007). In the same figure we plotted coseismic vertical motions in the forearc of the Maule  $M_w = 8.8$  2010 earthquake (Vigny et al., 2011). The horizontal scales for distance to the trench are different because they have been corrected for the dip of the shallow slab. The vertical scales differ because of the different magnitudes of the events. The fit to coseismic vertical displacements of our REF model is remarkably good given its generic nature, but the systematic misfits also show something that has been well established, that geodetic observations can resolve regional variations in earthquake slip.

Likewise, we get a reasonable fit with coseismic vertical displacements of GNSS, marine benchmarks, and pressure gauge observations from the 2011 Tohoku  $M_w = 9.0$  earthquake (Figure 17b) (Ito et al., 2011;

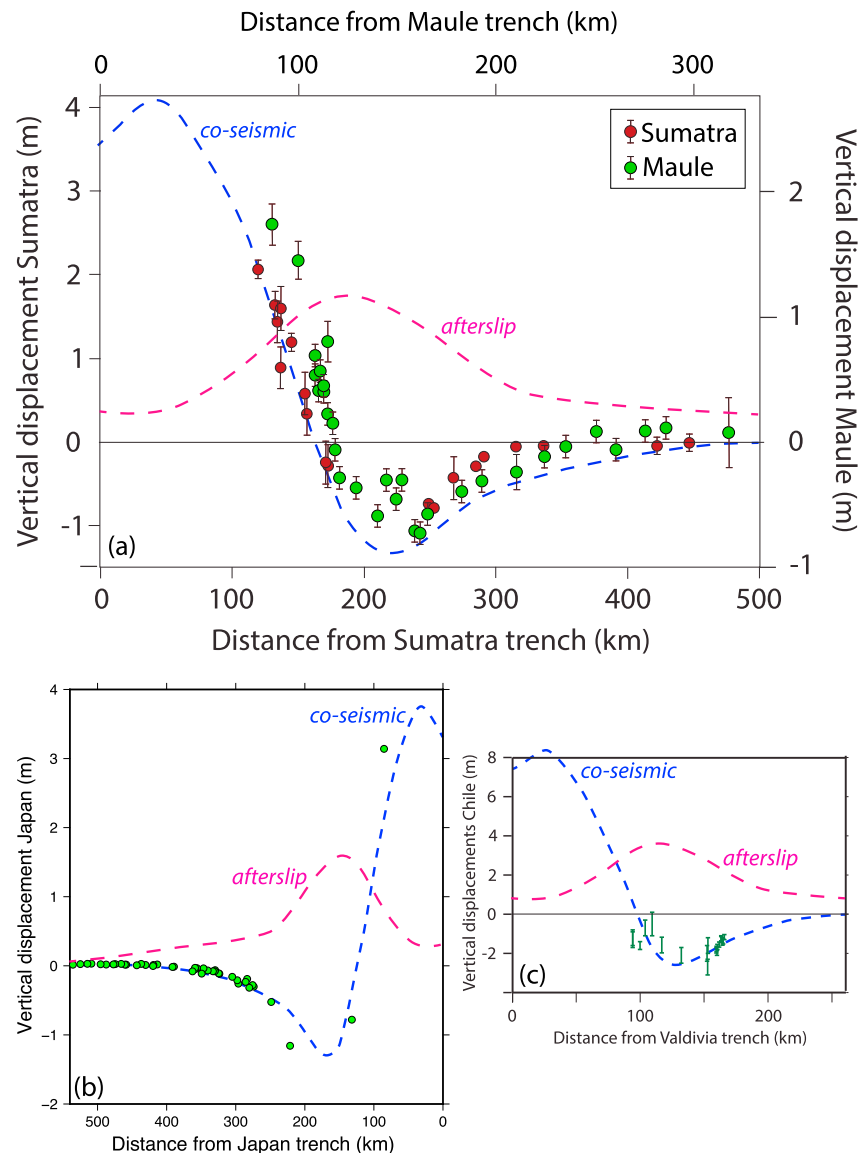


**Figure 17.** (a) Coseismic uplift inferred for the 2004 Sumatra earthquake (red = G-M9.15 from Chlieh et al., 2007) and for the 2010 Maule event (green, Vigny et al., 2011). Note that horizontal axes are different following a correction for the dip of the shallow slab. Vertical axes are different because the events had different magnitudes. The blue dashed line shows coseismic vertical displacement from the REF model (scaled horizontally and vertically also). The purple dashed line shows predicted uplift due to primary afterslip. See text for further details. (b) Coseismic uplift/subsidence along a profile perpendicular to the Japan trench through the region of maximum slip of the 2011 earthquake off-shore Sendai. GNSS data from Ozawa et al. (2011) and offshore transponder data from Sato et al. (2011). The dashed blue line is our REF model prediction. (c) Coseismic vertical displacement along a profile along 40°S perpendicular to the Nazca-South America trench through the high-slip area of the 1960 Valdivia earthquake (Moreno et al., 2009). The blue dashed line represents the REF model uplift/subsidence.

Ozawa et al., 2012; Sato et al., 2011). Similarly, for the Valdivia earthquake (Figure 7c), the observations agree approximately with coseismic uplift of our REF model along a cross section perpendicular to the trench along 40°S, where Moreno et al. (2009) infer the highest fault slip. Significant coseismic coastal subsidence and uplift (and a significant spatial variation) is commonly observed in great subduction earthquakes, and our models reproduce this effect.

#### 4.2.2. Horizontal Coseismic Displacements

Subduction zone earthquakes cause ocean ward displacement of the overriding plate. Displacements decrease from the trench to become zero at the backstop, beyond which there is no accumulation of

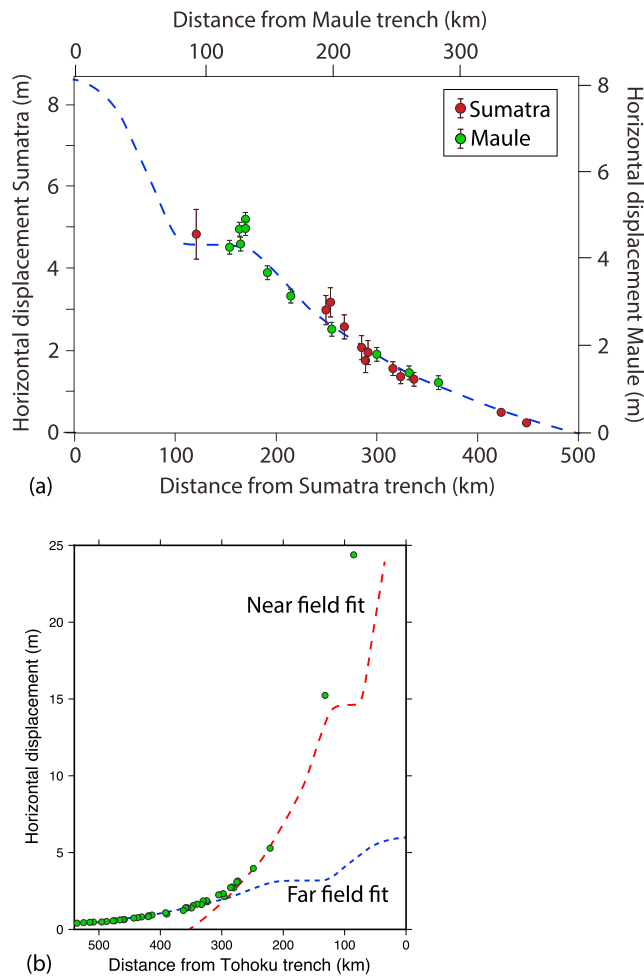


**Figure 18.** (a) Coseismic horizontal displacement in the epicentral region of the 2004 Sumatra earthquake (red = G-M9.15 from Chlieh et al., 2007), and E-W coseismic displacements for the 2010 Maule event (green, Vigny et al., 2011). The blue dashed line shows horizontal coseismic displacement of the REF model (scaled horizontally and vertically, see text). (b) Coseismic trench-perpendicular displacements along a profile directly north of Sendai (Ozawa et al., 2011; Sato et al., 2011). The fit of the model (blue dashed line) is acceptable only further inland.

the REF model is acceptable considering that it is generic only and ignores lateral variability; misfits result from nonuniform slip during the actual event.

#### 4.3. Relocking of the Seismogenic Interface

Surface displacements shortly after a major earthquake are a superposition of trenchward displacements due to afterslip, and ocean ward displacements due to relocking of the interface once this has occurred. As Wang et al. (2012) pointed out, the first signature of relocking is to be expected offshore near the trench. Watanabe et al. (2014) and Tomita et al. (2017) present (offshore) GPS/A displacements above the Tohoku seismic interface. Postseismic horizontal displacements in the northern part are directed landward in the northern part, meaning that the locking signature exceeds the imprint of afterslip here. The observations thus provide strong evidence that (significant part of) the seismogenic fault relocked shortly after the event.

Differences between the direction of relative plate motion and the direction of coseismic slip may also be diagnostic: in the Maule region, the decrease of a southward component in postseismic GNSS velocities is interpreted as evidence for rapid relocking here (Bedford et al., 2016).

elastic strain during the earthquake cycle. For comparing the coseismic horizontal displacement in our REF model to observations, we scale the horizontal axis so that the backstop is located where extrapolated data indicate that the displacements become zero. The vertical scale is adjusted for earthquake magnitude.

Figure 18 shows coseismic east-west displacements along a profile through the southern end of the maximum-slip region of the 2010 Maule event (Lorito et al., 2011), that is, at the latitude of Constitución (Vigny et al., 2011). The model fits the GNSS observations well. Similarly, the coseismic displacements perpendicular to the trench near the epicenter of the 2004 Sumatra earthquake (Chlieh et al., 2007) are reasonably well fit by the REF model.

Horizontal displacements due to the 2011 Tohoku earthquake are poorly fit by our model. The blue dashed curve in Figure 18b shows one fit to the data where the backstop lies ~650 km from the trench. This model fits the observations in the far field, but poorly within ~300 km from the trench. Alternatively, when we assume a backstop location around 350 km (red dashed line), the fit in the far field is poor. The near-field fit is imperfect, but reasonable considering that there are significant differences of the actual earthquake slip and coseismic slip in our model. Specifically, the actual fault slip is higher on the shallow part of the interface, and less on the deeper part (e.g., Hooper et al., 2013). This suggests that pre-event locking was more restricted to the updip part of the interface than we assumed in our model. A unified model that simultaneously reproduces the near- and far-field observations could involve a compliance contrast in the overriding plate. One needs to realize that a backstop represents a jump from elastic to rigid material. A less extreme contrast, more deformable near the trench and less deformable beyond 300 km would result in moderate strain in the far field (>300 km) if the backstop is located ~650 km from the trench. We do not elaborate on such model here, but we note that the compliance contrast would be colocated with the volcanic arc, and the backstop with the oceanic Yamato Basin.

Horizontal coseismic displacements along a profile through the maximum-slip patches of the 1964 Alaska earthquake (Suito & Freymueller, 2009) are given relative to an inland benchmark ~330 km from the trench (Snay et al., 1987). As shown by Figure A6, the fit of

In our models, we assume that relocking occurs immediately after the megathrust event. This assumption is commonly made in postseismic relaxation studies, albeit implicitly, by subtracting the interseismic horizontal GNSS velocities from the postseismic time series with the idea that the remaining signal reflects postseismic processes only (some examples are for Sumatra, 2004: Paul et al., 2012; Wiseman et al., 2015; for Maule 2010: Klein et al., 2016; and for Tohoku: Ozawa et al., 2012). Our model results show that relocking is not apparent in horizontal model displacements immediately after an event because (1) afterslip in combination with the onset of viscous relaxation driven flow obscures the fact that relocking has already occurred and (2) the majority of the observations are made onland. Therefore, despite trenchward motions on the Andaman Islands from 2008 to 2010 (Paul et al., 2012), the subduction interface may still have locked shortly after the Sumatra 2004 earthquake.

#### 4.4. Coseismic and Postseismic Tensile Stresses

Postearthquake evidence of tensile stresses in the overriding plate has been found at different margins. In north Chile, surface cracks are clearly related to large earthquakes (Delouis et al., 1998; Loveless et al., 2005; Scott et al., 2016). Young surface cracks are also found above the northern end of the Maule 2010 slip area (Aron et al., 2013; Arriagada et al., 2011) where normal faults are long-lived features (Aron et al., 2015). Young surface cracks were identified above the downdip end of the Tohoku 2011 finite fault (Mizoguchi et al., 2012). Normal faulting earthquakes deeper in the overriding plate followed shortly after the 2011 Tohoku earthquake (Asano et al., 2011; Kato et al., 2013, 2011; Toda & Tsutsumi, 2013), the 2010 Maule main shock (Fariás et al., 2011; Hicks et al., 2014; Ryder et al., 2012), and the 2014 Iquique earthquakes (Hayes, 2014). Subhorizontal tensile stress in our models (Figures 5b, 10c, and 11c) results from the delay between coseismic slip and afterslip on the deeper interface. This delay results from our assumption of a brittle fault above a viscoelastic shear zone. Afterslip redistributes the tensile stresses so that tension is decreased in the forearc region. This would suggest that periods of surface cracking and normal faulting would be restricted to the period shortly after the event.

#### 4.5. Postseismic Evolution

A large number of studies have addressed postseismic relaxation of megathrust earthquakes in the last decades. The clearest geodetic evidence for long-term postseismic relaxation is a velocity convergence line (a point in our 2-D models) (Wang et al., 2012). Both afterslip and viscoelastic relaxation are likely consequences of large earthquakes. Opinions differ regarding their relative importance because the processes can have similar geodetic signatures in specific observation windows, and rheology is a key component of the discussion.

##### 4.5.1. Horizontal Surface Kinematics Following the Sumatra 2004 Earthquake

Pollitz et al. (2006) reproduced the initial 120 day postseismic GNSS time series for the 2004 Sumatra earthquake using a Burgers asthenosphere rheology. This biviscous rheology has both a short-term (Kelvin) and a long-term (Maxwell) relaxation time as required by particularly the early part of the time series. Since then, Burgers rheology has been widely used to model postseismic relaxation. For the 2004 Sumatra event it was adopted in the context of radially stratified models by Panet et al. (2010), Hoechner et al. (2011), and Broerse et al. (2015), and for models with a slab by Pollitz et al. (2008) and Hu and Wang (2012).

Afterslip is an alternative process for introducing short-term relaxation that we employ in our model in combination with a simpler (Maxwell) rheology of the asthenosphere. The Andaman and Nicobar Islands showed significant and rapid uplift (Banerjee et al., 2007; Bilham et al., 2005; Gahalaut et al., 2008, 2006; Paul et al., 2012), and further trenchward displacements. These observations were interpreted to result from afterslip. Chlieh et al. (2007) find that afterslip during the first 40 days after the event corresponds with a moment release of ~35% of the coseismic moment to the south of 11°N, a figure that agrees roughly with what we find (Figure 3c). They indicate that <1% of the afterslip moment was released as aftershocks and the majority of afterslip occurred aseismically. To the south of the Nicobar Islands, the spatial anticorrelation of regions of significant afterslip with regions with high coseismic slip is good. This agrees with afterslip driven by coseismic shear stresses like we have it in our model.

Figure 19a shows the horizontal displacement since the earthquake of GNSS benchmark CARI in Port Blair (south Andaman Islands, Figure 19a) which is located at 130 km from the Sumatra-Andaman trench. The benchmark displacement is scaled with its coseismic horizontal displacement. We refer to this as the *horizontal displacement ratio* (HDR). HDR is useful in the context of geodetic observations at varying distances from



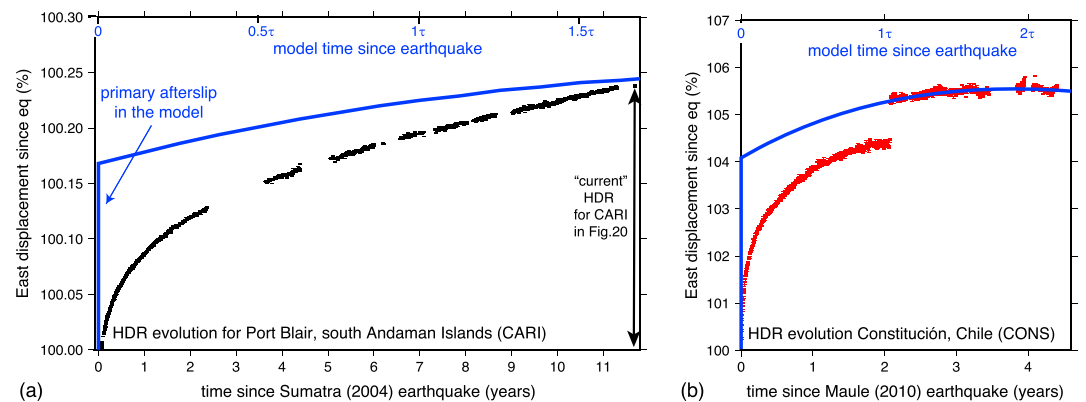


**Figure 19.** Evolution of postseismic horizontal displacement as fraction of the coseismic horizontal displacement (HDR) of benchmarks following the 2004 Sumatra event. Black bars represent GNSS observations (not corrected for interseismic velocities); blue lines are results of the REF model (corrected for different slab dip and scaled vertically). (a) Near-field east ward displacement at CARI (Port Blair)—Data downloaded July 4 2017 from the Nevada Geodetic Laboratory, University of Nevada Reno ([http://geodesy.unr.edu/NGLStationPages/GPSnetmap/GPSNetMap\\_MAG.html](http://geodesy.unr.edu/NGLStationPages/GPSnetmap/GPSNetMap_MAG.html); Blewitt et al., 2016). The original GNSS solutions are expressed in the ITRF08 coordinate system (Altamimi et al., 2011). We rotate the data into the fixed Sunda reference frame (Altamimi et al., 2012). The coseismic displacement was taken from Gahalaut et al. (2006). (b) East ward displacement at station CONS after the 2010 Maule earthquake (data downloaded from Nevada Geodetic Laboratory).

the trench. Typically, such observations are dominated by the stations nearest to the trench. HDR gives more equal weight to observations at all distances from the trench. The blue curve shows our model response, corrected for the different slab dip. The model does not reproduce the initial part of the observations. This likely is a consequence of our model assumption of a very low viscosity shear zone downdip from the seismogenic interface. Primary afterslip in the model therefore occurs instantaneously, whereas the data suggest that it should occur over a longer period (few years?).

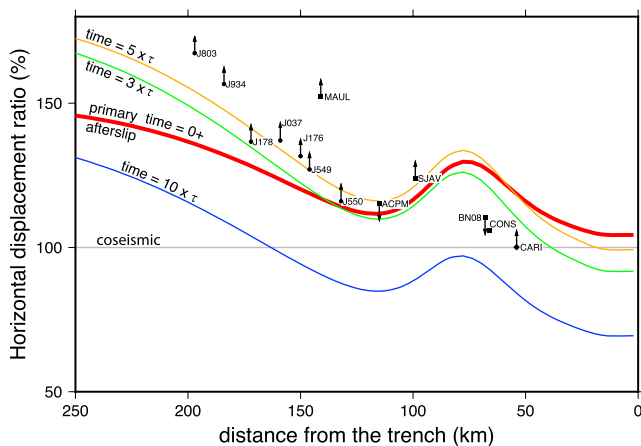


**Figure 20.** Ratio of horizontal displacement since the earthquake and the coseismic horizontal displacement (HDR) for locations at different model distances from the trench. The lines show the horizontal displacement ratio from the REF model. The gray line (100%) represents the coseismic horizontal displacement, the thick red line corresponds with coseismic + primary afterslip, and the other lines represent the accumulated horizontal deformation at different viscoelastic relaxation times. Dots represent the horizontal displacement ratio for various GNSS benchmarks at the end of currently available time series (data downloaded July 4 2017 from the Nevada Geodetic Laboratory, University of Nevada Reno): Solid circles for the 2011 Tohoku earthquake, squares for the 2010 Maule earthquake, and a diamond for the 2004 Sumatra earthquake. Arrows indicate whether the ratio increases or decreases. Benchmark distance from the trench is mapped into model distance, like for Figure 17, by  $\tan(\alpha)/\tan(25^\circ)$ . The observed horizontal displacement ratio is not corrected (see text for discussion).

Near-field horizontal displacements are getting closer to the model after  $1\tau$ . The “current” HDR (which is the HDR at the end of the available time series) is shown in Figure 20 for a number of near and intermediate field stations. The HDR of the Port Blair benchmark (CARI) has shown little change in the 11.7 years since the earthquake, as is clear also from Figure 19a. The model predicts that primary afterslip would have resulted in a substantial increase of the HDR followed by a decrease due to reloading since  $\sim 3\tau$ . Primary afterslip was probably not instantaneous in reality.

#### 4.5.2. Maule 2010 Horizontal

Figure 19b show the HDR evolution after the 2010 Maule earthquake for GNSS station CONS in Constitución near the Chilean coast. The misfit of our model to the initial part of the time series is large. Following an aftershock (which is essentially part of the afterslip) the fit is rather good but only if we rescale the vertical model axis to match the data. Figure 20 shows the HDR for five stations (BN08, CONS, SJAV, ACPM, and MAUL) in Chile without scaling. The observed HDR increases with distance from the trench. Similar to what we saw for CARI, BN08 and CONS are located well below the primary afterslip curve 4.4 years after the main shock. The BN08 time series first increased and has now started to decrease. In line with our previous discussions we suspect that this misfit is a consequence of primary afterslip that takes place over the course of years rather than instantaneously as we now have it in our model.

#### 4.5.3. Tohoku 2011 Horizontal

Trubienko et al. (2014) were the first to consider the HDR along a cross section perpendicular to the trench of 2011 Tohoku earthquake. HDR at

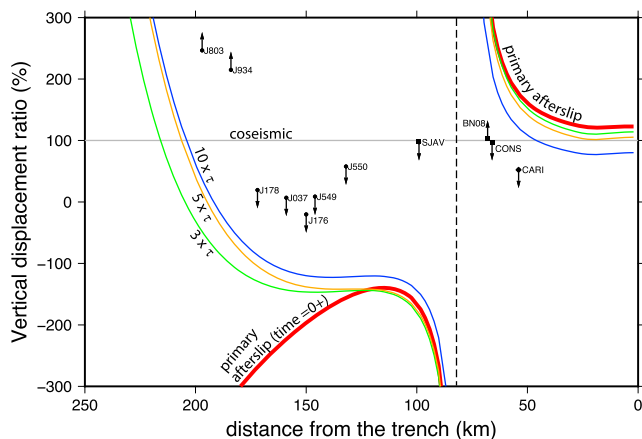


**Figure 21.** Ratio of vertical displacement since the earthquake and the coseismic vertical displacement (VDR) for locations at different model distances from the trench. The lines show the VDR from the REF model. The gray line (100%) represents the coseismic vertical displacement, the thick red line corresponds with coseismic + primary afterslip, and the other lines represent the accumulated vertical deformation at different viscoelastic relaxation times. Dots represent the VDR for various GNSS benchmarks at the end of currently available time series: Solid circles for the 2011 Tohoku earthquake, squares for the 2010 Maule earthquake, and a diamond for the 2004 Sumatra earthquake. Arrows indicate whether the ratio increases or decreases. Benchmark distance from the trench is mapped into model distance by  $\tan(\alpha)/\tan(25^\circ)$ .

stations J178, J037, J176, J549, and J550 after 6.3 year agrees roughly with the model prediction of primary afterslip and subsequent post-seismic relaxation during  $5\tau$  (orange line in Figure 20). The fit is poor for stations J803 and J934, and the increasing trend of HDR's means that the fit is further deteriorating. As we saw with the coseismic horizontal displacements (Figure 18b), we cannot fit a single model to both the near and far-field data. The HDR model curves are therefore not expected to reproduce the data either. Another confounding factor likely is three-dimensionality, which become more important with increasing distance from the coseismic slip zone. Specifically, afterslip along lateral edges (Freed et al., 2017) also contributes to the horizontal displacements of these stations thereby increasing the HDR beyond what is predicted by our model.

#### 4.5.4. Sumatra 2004 Vertical

Postseismic relaxation resulted in long-wavelength subsidence of the overriding plate after the 2004 Sumatra earthquake (Broerse et al., 2015). For example, Phuket subsided  $\sim 60$  mm during the 7 years following the earthquake. Near-field vertical displacements were more variable, but the detailed pattern is incompletely constrained by the observations. Figure 21 shows the vertical displacement ratio (VDR). This figure is harder to understand because the coseismic verticals change sign twice resulting in two asymptotes and positive and negative values of the VDR. The horizontal dashed line represents the VDR of the earthquake. The red curve shows the VDR of the REF model after primary afterslip. Yellow, green, and blue curves represent the model

VDR after  $3\tau$ ,  $5\tau$ , and  $10\tau$ , that is, after viscoelastic relaxation and continued slip on updip and downdip sections of the interface.

Near-field station CARI (Port Blair) subsided immediately after the earthquake (Bilham et al., 2005). Since then, the station has been moving upward again but the net (coseismic plus postseismic) vertical displacement still is downward. When we use the "coseismic" subsidence of CARI, we consequently find a VDR of 54%, and decreasing, 12 years after the event. This result is clearly inconsistent with the model predicted increase due to primary afterslip (red line). If we follow the often-suggested interpretation that here it was a slow-slip event, (rapid) afterslip possibly would have been an integral component of the "coseismic" event. In this interpretation, the current uplift (and associated decrease in the VDR) would be an expected expression of post-seismic processes. The discrepancy with the model would be smaller in this case.

Coseismic vertical displacements are very small in the far field relative to the observation uncertainty for even the largest magnitude earthquakes (Figure 4a). VDR therefore is highly sensitive/unstable in the far field, and we do not consider the VDR of the continuous station in Phuket.

#### 4.5.5. Maule 2010 Vertical

Stations in Constitución (CONS), Concepción (BN08 and CONZ), and San Javier (SJAV) are located in the Chilean forearc. CONS subsided 4.7 m during the earthquake. It did not subside further during 4.4 years following the event as would be expected if primary afterslip would have occurred during this period (red curve in Figure 21). Rather, two small earthquakes resulted in minor uplift as represented by its VDR of 97%.

Concepción subsided 2.9 m due to the earthquake. Seven years after the earthquake further subsidence has occurred so that the VDR is 103% (Figure 21). This can be understood in the context of the model only if we accept that primary afterslip occurs over a longer period like we saw in our discussion of HDR. In this case, further subsidence due to (slower) primary afterslip could be balanced by the contribution of viscoelastic relaxation so that the VDR changes little.

Benchmark SJAV subsided 46 cm during the earthquake. Its VDR has hardly decreased during 4.5 years after the earthquake as would be expected based on the REF model.

The mismatch between our model predictions and observed VDR is perhaps not surprising in light of the conclusion of Klein et al. (2016) that a complex pattern of upward and downward postseismic velocities

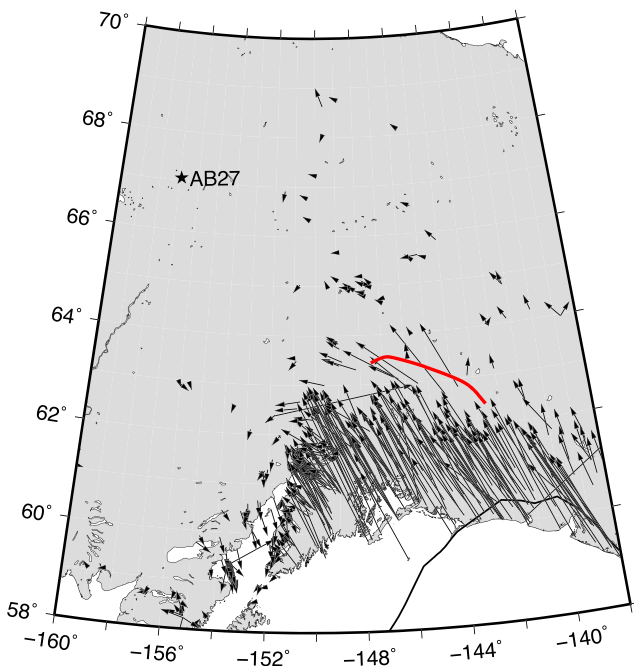


**Figure 22.** Current horizontal velocities relative to AB27 in the region of the 1964  $M_w$  9.2 Prince William Sound (Alaska) earthquake (Snay et al., 2016). The red line indicates the  $M_w$  7.9 Denali earthquake fault. Landward velocities indicate locking of the subduction interface. Based on these observations, one would infer that the postseismic period is largely over (see text for further discussion).

exists in the forearc. Melnick (2016) finds more consistent subsidence than Klein et al. (2016), but he also has conflicting observations near the northern region of the highest coseismic slip. This complexity defies our attempt to model it with a simple 2-D model.

#### 4.5.6. Tohoku 2011 Vertical

Land subsidence due to the 2011 Tohoku earthquake was followed by uplift that can be largely ascribed to afterslip down-dip from the maximum-slip part of the coseismic fault (Diao et al., 2013; Hu et al., 2016; Yamagiwa et al., 2015). After 6.3 years, the observed VDR of all stations is, however, significantly larger than expected from the REF model (Figure 21). The reason for the mismatch could be that (the VDR decrease by) afterslip is slow and counteracted by viscoelastic flow (which increases VDR).

#### 4.5.7. Chile 1960

Extensive uplift following the 1960 Valdivia earthquake was attributed to afterslip by Barrientos and Ward (1990) with a characteristic time of 15.6 years (Barrientos et al., 1992). At the latitude of the highest coseismic slip, locking today results in landward velocities within ~200 km distance from the trench (Wang et al., 2007). Trenchward velocities in the backarc further to the east indicate continued postseismic relaxation (Moreno et al., 2010). These observations agree qualitatively with our model (Figure A7).

#### 4.5.8. Alaska 1964

The region of postseismic uplift largely coincides with the region that subsided during the 1964 Alaska earthquake. Suito and Freymueller (2009) conclude that this uplift was largely driven by afterslip in the decade after the event.

Snay et al. (2016) present a GNSS velocity field for Alaska in a “stable North America” reference frame that is corrected for post-glacial relaxation. A confounding factor for an interpretation in terms of postseismic signature is the likely existence of a Bering plate (Cross & Freymueller, 2008) that moves southeastward relative to North America. Figure 22 shows horizontal velocities relative to station AB27. The signature of locking of the subduction interface is clear in a broad region from the coast to ~200 km inland. Further inboard, the imprint of the 2002  $M_w$  7.9 Denali earthquake is clear. Trenchward velocities are not visible east of 150°W, suggesting that postseismic relaxation has mostly passed if one were to use the “convergence point” as the sole indicator. However, mostly downward velocities are expected during the interseismic period, and this is not what is observed over Kenai Peninsula and Cook Inlet where uplift rates exceed 10 mm/yr, even after correction for glacial isostatic adjustment (Freymueller et al., 2008; Snay et al., 2016). More likely this is because the relatively short distance between the trench and the backstop hides the convergence point here like we saw in Model 7 (Figure 13), where it reaches the backstop already during the postseismic phase (around  $3\tau$ ). This would be earlier if the backstop were located closer to the trench. Vertical velocity in this case would be a more reliable indicator of whether the postseismic phase has passed. Continuing uplift suggests that postseismic relaxation still occurs in the region of the 1964 Prince William Sound earthquake (Figure A8).

### 4.6. Inter/Preseismic Period and Seismic Coupling

Pre-Maule horizontal velocities parallel to the Nazca-South America convergence vector as derived from GNSS campaigns 1996–2002 by Ruegg et al. (2009) fit a straight line with ~55 mm/yr at the trench and zero mm/yr at ~400 km distance from the trench along a swath 35.5°–36.5°S. In our models, such a linear decrease occurs between the trench and the backstop and corresponds with shortening of the elastic overriding plate on a viscous mantle. Down flexing of the overriding plate in our models agrees with vertical displacement rates 1992–2000 from coral growth before the 2007  $M_w$  8.4 Mentawai (Sumatra) earthquake (Chlieh et al., 2008). Pre-2011 Tohoku velocities (Hashimoto et al., 2009; Loveless & Meade, 2010) show a semilinear decrease of horizontal velocities toward the backarc also. Well-resolved subsidence of the forearc occurred before the 2011 Tohoku earthquake (Hashimoto et al., 2009). Our model thus agrees qualitatively with the observations.

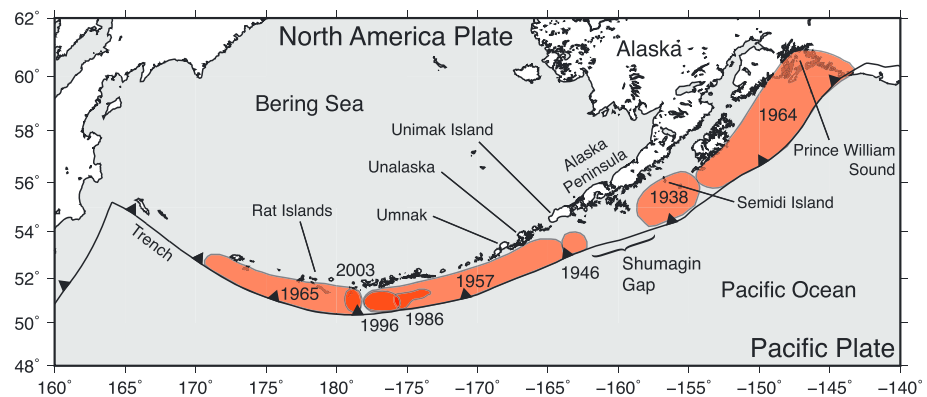


**Figure 23.** Rupture zones and years of instrumentally recorded great ( $M_w$  7.7–9.2) megathrust earthquakes along the Aleutian subduction zone.

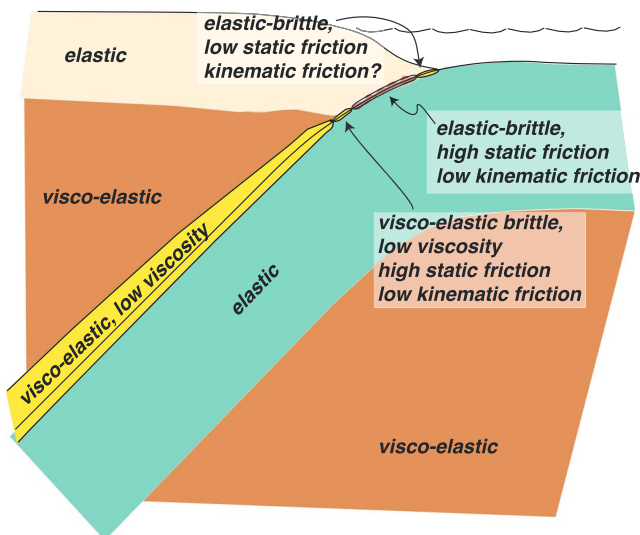


**Figure 24.** Synthesis of rheological elements that are needed for a consistent geodynamic evolution over many earthquake cycles and that have an expression in seismological, geodetic, and/or geological observations during (parts of) the cycle. The deep viscoelastic shear zone between the slab and the wedge (yellow) plays an important role during primary and secondary afterslip and associated sinking of the slab. This shear zone results from dynamic strain localization along the plate contact so that the shear stress between the slab and the wedge is less than 1 MPa. At the upper end of this shear zone, brittle processes contribute (substantially?) less than viscous flow to the permanent strain, as is needed by colocated primary afterslip and aftershocks immediately downdip of the locked fault, and by postseismic normal faulting in the overriding plate. The seismogenic fault is fully locked throughout the cycle and relocks rapidly after the earthquake, so it has a high static friction and a low kinematic friction. The updip section of the interface has a lower static friction but still exhibits relatively low interseismic slip due to the slip nearby locked fault. The tsunami potential of the earthquake will significantly increase when the updip fault slips coseismically. It depends on whether the coseismic kinematic friction is higher or lower than the long-term kinematic friction. The regions surrounding the interface are largely elastic and viscoelastic. Although the asthenosphere is a power law material, viscosities are essentially constant here given the relatively small stress changes during the earthquake cycle.

#### 4.7. Summary and Conclusions

Observations of coseismic surface deformation are reasonably well reproduced by our models after correcting for the dip angle of the fault. The observations call for primary afterslip that occurs over periods of months to years. This is a clear discrepancy with our simple model. For afterslip also a correction for slip of the involved interface is required; the surface observations are most sensitive to the orientation/dip of the interface immediately downdip of the coseismic fault. Horizontal displacements are reasonably well reproduced during the postseismic period but may be further improved by using a realistic slab geometry because this affects the stressing of the viscoelastic wedge during earlier stages. Vertical postseismic displacements are sensitive to details of the postseismic processes and are not well matched by our generic model. Model predictions for the interseismic period agree qualitatively with the observations.

### 5. Discussion

#### 5.1. Identifying Seismic Gaps or Low Coupling Regions During the Postseismic Period

The Shumagin seismic gap along Alaska Peninsula (Aleutian margin, Figure 23) is straddled by the location of two mid-1900 earthquakes: 1938  $M_w$  8.3 earthquake near Simidi Island in the east (Johnson & Satake, 1994; Sykes, 1971), and the 1946  $M_w$  8.2 Scotch Cap earthquake near Unimak Island in the west (Johnson & Satake, 1997; López & Okal, 2006). On the Simidi Island segment, relocking of the interface is clear from horizontal GNSS velocities away from the trench (Fournier & Freymueller, 2007). Further westward along Alaska Peninsula, the GNSS velocities become more trench parallel, which was interpreted as locking decreasing to zero in the Shumagin part of the margin (Fournier & Freymueller, 2007; Larson & Lisowski, 1994). There are no known historical events in the Shumagin gap. The absence of uplifted terraces and subsided shorelines on Shumagin Islands (Witter et al., 2014) and slow subsidence since 3.4 ka supports the interpretation as a creeping segment here (Fournier & Freymueller, 2007).

The 1946  $M_w$  8.2 event near Unimak Island demonstrates that this part of the margin is seismogenic. Geodetic observations on Unimak Island

(Cross & Freymueller, 2008) may give a false impression of low coupling of the subduction interface if postseismic relaxation of the 1946 event still continues (Figures 7 and 15b). We think that this is very likely given our conclusion that the Prince William Sound part of the margin still is in the postseismic phase. Our interpretation also explains observations of multiple tsunami deposits (the last in 1957) above a section of the margin that was previously interpreted to be creeping (Witter et al., 2016). Coseismic slip during the 1957  $M_w$  8.6 Aleutian earthquake thus likely extended east to Unimak along the locked margin.

GNSS velocities even further to the west (Unalaska, Umnak, and Rat Islands) are small and show only volcanic signatures (Cross & Freymueller, 2008; Freymueller et al., 2008). Here, too, we expect that the geodetic observations do not reveal the actual locking pattern due to postseismic relaxation. Finite faults of the 1965  $M_w$  8.7 Rat Islands earthquake (Beck & Christensen, 1991) and of the 1957 Aleutian earthquake together cover this part of the margin. There are no clear indications in the data for the Aleutian-Alaska margin for creeping sections other than the Shumagin gap (157–161°W).

### 5.2. Rheological Complexity

Our model is based on a simplified rheology. Specifically, rate-and-state interface friction and Burgers bulk rheologies are ingredients of many models, particularly those addressing the coseismic phase but also after-slip (e.g., Hetland & Simons, 2010; Perfettini & Avouac, 2004). Our model rheology is, however, not simple (Figure 23). On short time scales, all parts of the subduction zone are elastic. The locked fault requires a high static friction and a low kinematic friction. The mantle wedge and the slab need to be mechanically decoupled by a zone of localized deformation to facilitate afterslip and to make it possible that the slab can subduct on geological time scales. It is most likely that this deformation zone is a viscoelastic shear zone at high temperatures deeper in the mantle like we used in the models, and we assumed that the brittle-ductile transition in the plate boundary zone occurs immediately downdip of the locked zone. In reality, a fraction of the primary afterslip occurs by aftershocks downdip of the locked fault, which suggests that the uppermost part of the shear zone involves coexisting brittle deformation at high stresses and slip rates. The updip part of the interface has low static friction, and during primary afterslip the kinematic friction is higher here. Alternatively, updip coseismic slip requires a low kinematic friction so that the deep rupture can extend to the ocean bottom which will increase the tsunami potential. With our goal in mind of identifying the main physical processes that are common to seismogenic subduction margins, the relatively good fit to geodetic observations based on simplified rheology is encouraging, but it is also clear that modeling of particular postseismic time series of horizontal and vertical displacements requires more rheological detail.

### 5.3. Geometric Complexity

Our focus on megathrust events with very wide margins that are affected by them allow us to study the response in a two-dimensional cross section. However, finite fault solutions of the great events show major lateral variations in the coseismic slip, as do preseismic locking patterns. Particularly, near-field observations are sensitive to such variability and it is clear that three-dimensional models are needed to reproduce all aspects of the geodetic observations (e.g., Pollitz et al., 2008; Suito & Freymueller, 2009).

Slab dip exerts a major influence on the geodetic expressions of deep earth processes during all stages of the cycle. Corrections for slab dip in the near field are simple, and we exploited them here. Deep afterslip and its coupling to flow in the mantle wedge require the incorporation of a realistic slab dip during the postseismic phase.

### 5.4. Physical Model Consistency and Including Multiple Earthquake Cycles

We specifically consider models where afterslip and viscoelastic relaxation are a result of a significant earthquake. The models do therefore not apply to large aseismic slip transients that may or may not be induced by small earthquakes (e.g., Dragert et al., 2004; Schwartz & Rokosky, 2007), and which are associated with tremors near the downdip end of the seismogenic zone. Consistent afterslip (i.e., stress driven) thus is a consequence of the shear stresses resulting from the loading history including the main quake (Hu et al., 2016; Mikhailov et al., 2013; van Dinther et al., 2013). This is where our inclusion of the prestresses via the cyclic earthquakes is important. The amount of slip on our model shear zone is a consequence of the need for resolving the slip budget over multiple cycles, and significant deep afterslip directly after the earthquake is an integral component of this. In such a consistent framework, it is possible to next investigate shear/fault zones with rheological complications if required by geodetic time series.



### 5.5. Postseismic Landward Velocities

Three years after the Tohoku earthquake two of the offshore GPS/A stations above the coseismic fault showed significant landward displacements (Watanabe et al., 2014). We interpret this as a consequence of relocking of the coseismic interface. The highest possible landward velocity due to locking to the trench is the convergence rate, that is,  $93 \pm 5$  mm/yr offshore Tohoku (Argus et al., 2011). The postseismic horizontal velocity of station KAMS was approximately equal to this (Watanabe et al., 2014). The horizontal velocity of station MYGI since the  $M_w$  7.3 aftershock was only slightly higher than the convergence rate, again largely in agreement with relocking. More recently, GPS/A observations with the extended offshore network show landward velocities at localities above the coseismic fault (Tomita et al., 2017). Interestingly, landward velocities of stations G07–G09 and G13 are slightly higher than the convergence rate. Given its persistence years after the earthquake, this is unlikely to be caused by poroelastic flow. Very likely this additional landward motion is driven by viscoelastic relaxation of shear stresses that result from slip gradients on the updip part of the coseismic fault (Sun et al., 2014; Sun & Wang, 2015). Observational support for this mechanism is, however, limited for two reasons: first, it is because details of the coseismic slip distribution are typically poorly resolved near this end of the subduction fault (Hooper et al., 2013) and the second reason is that (currently unobserved) primary afterslip further updip will tend to reduce the slip gradient and diminish viscoelastic flow. The reason why our reference model does not show additional landward velocities in the early postseismic phase (cf. Figure 6a) is due to model choices; because we do not lock the interface to a depth of 10 km, interseismic slip reduces the displacement gradient here (Figure 3b). A second reason is that primary afterslip on this updip part is faster than viscoelastic relaxation elsewhere (and probably too fast); slower primary afterslip would result in a longer period during which slip gradients persist. In their regional Tohoku model, Hu et al. (2016) incorporate afterslip that it is driven by coseismic shear stresses, and they find an overall good fit to the surface displacements 2 years after the Tohoku earthquake. In the offshore region above the coseismic interface their model does, however, not reproduce landward displacements. Inaccuracies in the coseismic slip model, in the identification of parts of the interface that exhibit afterslip, or in the evolution of afterslip may result in overestimate or underestimates of the additional landward motion by viscoelastic models.

### 5.6. Future Directions

A complete characterization of the common processes that act at different margins requires further development of the relatively simple models that we present here. Specifically, what will be needed are a more realistic slab geometry, three-dimensionality (also to be able to incorporate smaller events), slower primary afterslip, and observationally constrained effective elastic thicknesses of the involved plate. There are two prime reasons why it will be important to only add complexity that is required by surface kinematic observations. First, inversion of complete geodetic time series requires that such next generation models are relatively simple. Second, many of the megathrust parameters are relatively unconstrained for the past, so that any realistic attempt to extend the models to the geological past so that we can interpret geological observations needs to be based on the main physical features only. For instance, the question of how mountain building on geological time scales is connected to the earthquake cycle is currently still wide open.

## 6. Conclusions

Similar physical processes drive the geodetic imprint of megathrust events during the earthquake cycle at different margins (Figure 24). Available observations are largely consistent with our model predictions based on a subduction interface that is fully locked in the depth range (few to  $\sim 10$ ) to  $\sim 40$  km, except during earthquakes. Relocking is probably fast. Further downdip, the interface is a viscoelastic shear zone where aftershocks contribute modestly to slip in its uppermost part. Observations suggest a relaxation time of a few years for this shear zone. The shear zone continues to be active, while bulk viscous relaxation in the mantle occurs. Simple shortening occurs of the overriding plate between the plate contact and a backstop in the overriding plate after postseismic relaxation.

The duration of the postseismic relaxation period is controlled by (1) the earthquake recurrence rate and (2) the mantle viscosity. Specifically, the ratio of the characteristic time between megathrust events and the mantle relaxation time is important. Whether or not this relaxation is expressed in horizontal and vertical surface deformation depends largely on the earthquake magnitude.

In the context of our mechanical models we conclude the following. Surface displacements and velocities are very sensitive to earthquake magnitude, slab dip, and to the distance between the trench and the backstop. They are not very sensitive to details of the mechanical coupling between the deep slab and the mantle wedge. Coseismic friction on the interface updip of the seismic fault affects the tsunami potential but has no effect on the surface kinematics.

A potential mechanism for short living tensile stresses above the downdip end of the coseismic fault as observed after, for example, the 2011 Tohoku and 2010 Maule events, may be delayed slip of the deeper interface. These stresses decrease when the downdip part of the interface starts slipping.

If not properly corrected for, inversion of kinematic observations during the postseismic period gives a false impression of an unlocked interface. From inversion of our synthetic GNSS observations we find that the locking pattern can be reasonably well resolved during the interseismic period for a well-designed network. Slip on the deep interface below the locking depth is never correctly reproduced by inversions.

## Glossary

Afterslip	One form of postseismic relaxation. Transient slip on the same plate interface that was active coseismically. Afterslip occurs predominantly on the part of the interface where there was little or no coseismic slip. Aftershocks of the coseismic earthquake can be considered as afterslip that produces seismic waves.
Backstop	Far-field location on the upper plate that is best constrained by where interseismic horizontal velocities are observed to become very small.
Brittle-ductile transition	The depth at which mechanical behavior changes from elastic+fault slip to viscoelastic.
Coseismic slip	Rapid slip on the seismogenic portion of the plate interface that radiates seismic waves, that is, an earthquake
Deep shear zone	A narrow (<1 km wide) zone with low shear strength between the top of the subducting plate and the mantle of the upper plate downdip of the seismogenic fault.
GNSS	Global Navigation Satellite System, including the United States' Global Positioning System (GPS), the European Union's Galileo system, and the Russian GLONASS system.
GPS/A	Positioning system for the sea floor based on combining GNSS positioning of a buoy or ship with acoustic ranging of transponders on the bottom of the sea.
Interseismic loading	Stress accumulation in elastic overriding and subducting plates resulting from continued plate convergence while the interface is partly locked.
Interseismic period	The interval between earthquakes after transient, postseismic processes have ended.
Locking	When tectonic plates cannot slide across their boundary due to frictional resistance, they are "locked" to each other. Plates that can slide past each other are "unlocked." The earthquake cycle centers on the locking, unlocking, and relocking of the seismogenic one.
Mantle wedge	The deeper, warmer region of the upper plate and mantle that can deform through viscous flow during postseismic and interseismic periods.
Maxwell rheology	Combined mechanical material property of a linear isotropic elastic material and a linear isotropic viscous material. The initial response to a shear stress of a Maxwell material is elastic, and viscoelastic thereafter.
Maxwell time	Characteristic time for relaxation of shear stresses in a material with a Maxwell rheology (cf. Appendix A).
Megathrust	Plate boundary interface between a subducting and an overriding plate. The term was used in the context of the 1964 Alaska earthquake by Plafker (1969).
Overriding (or Upper) plate	The lithospheric plate that lies above the subducting slab.
Postseismic relaxation	Transient deformation processes driven by coseismic shear stresses, that is, afterslip and viscoelastic relaxation.

Relocking	Refers to the process of locking of the part of the megathrust that was also locked before an earthquake.
Seismic (or earthquake) cycle	A repeated pattern of elastic strain energy accumulation and subsequent release in an earthquake, consisting of characteristic periods: the coseismic period of the earthquake, the postseismic period after an Earthquake, and the interseismic period between earthquakes. The duration of one cycle varies strongly; that is, the seismic cycle is nonperiodic.
Seismogenic fault	The area of the plate interface that is locked and accumulating shear stresses in between earthquakes then subsequently slips during the coseismic rupture.
Subducting slab	The lithospheric plate that descends beneath the overriding plate.
Viscoelastic relaxation	One form of postseismic relaxation whereby shear stresses decrease as permanent shear strain accumulates and flow occurs.

## Appendix A

Figures A1–A8 show additional model results and regional observations.

### A1. Elastic and Viscoelastic Parameters

#### A1.1. Characteristic Elements of Elastic and Viscoelastic Materials

The first-order mechanical properties of rocks are well represented by compressible elasticity and incompressible viscous shear flow. The shear stress in an elastic material that results from an imposed shear strain

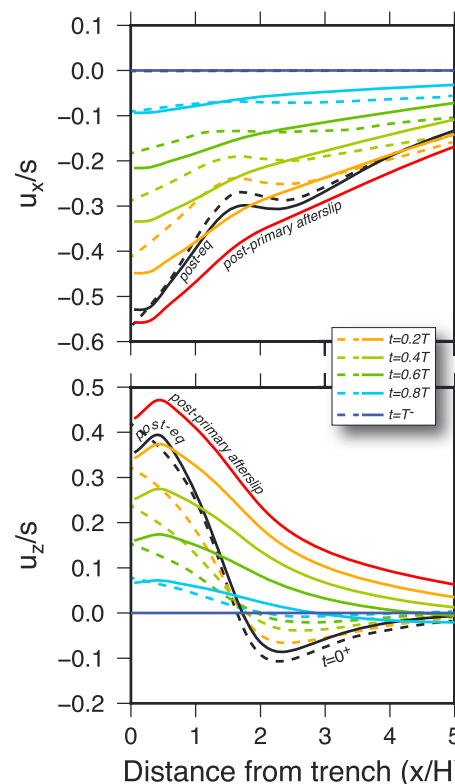


**Figure A1.** Comparison of our model (solid lines) with the multicycle model of Segall (2010) (dashed lines), which is based on a horizontal elastic plate above a viscoelastic half-space (Savage, 1983). Horizontal and vertical surface displacements ( $u_x$  and  $u_z$ ) scaled by the coseismic slip ( $s$ ) as function of horizontal distance from the trench on the overriding plate ( $x$ ) scaled by the plate thickness ( $H$ ). Here the fault/slab dips  $30^\circ$  and the time ratio is  $\mu T/\eta$  (shear modulus  $\mu$ , earthquake cycle time  $T$ , and viscosity  $\eta$ ). Dashed lines show the surface response immediately after the layer-cutting earthquake (time  $t = 0^+$ ), and at different fractions of  $T$  thereafter. Solid lines are the displacements from our model at the same time, and after primary afterslip (red line), which does not occur in the other model. The coseismic response in black of the models is very similar although we have no locking of the updip part of our models. However, differences are significant at all stages until late in the earthquake cycle.

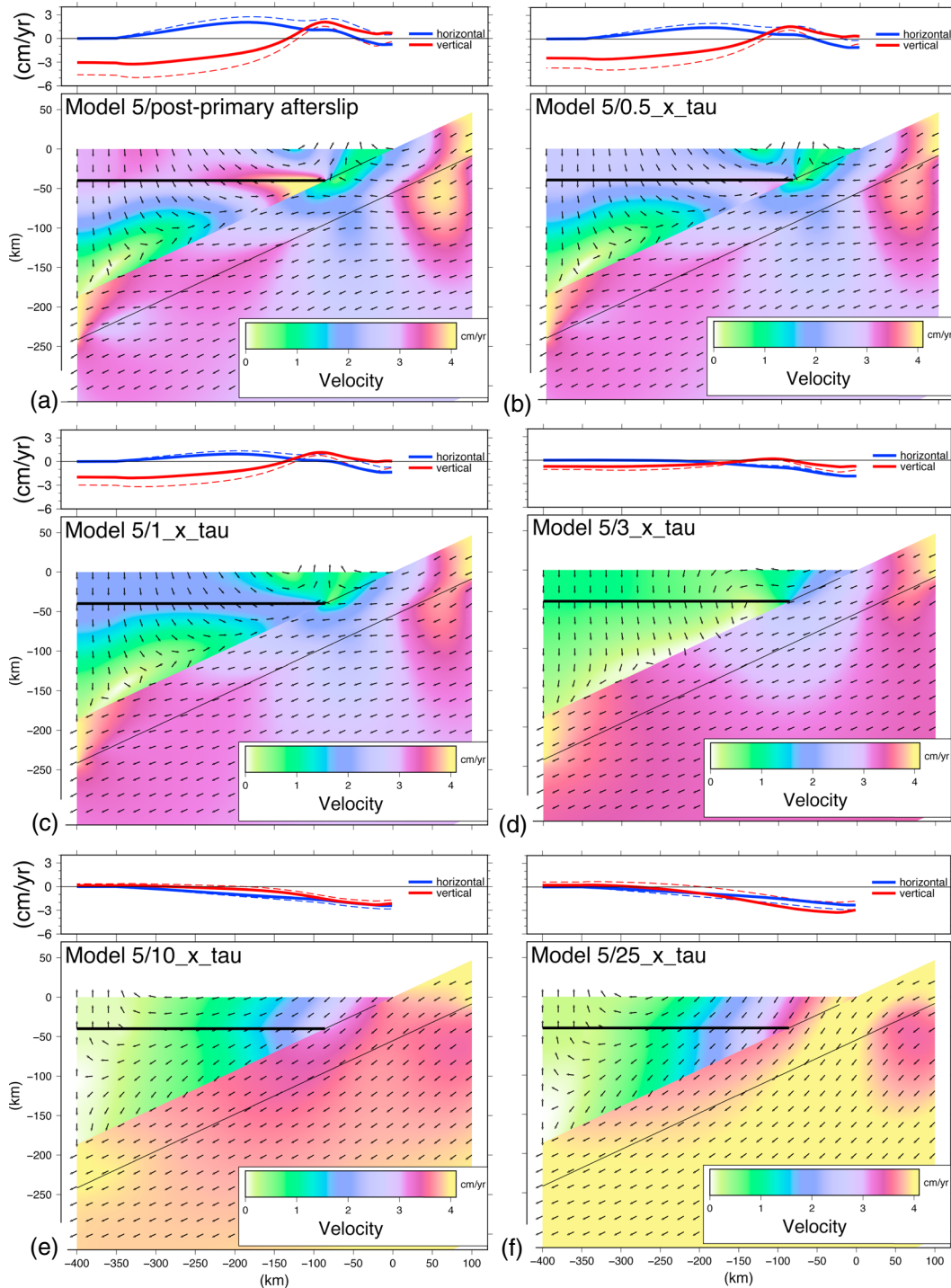


**Figure A2.** Evolution of the velocity field for Model 5 (thinner slab). In all top panels, surface velocities of the REF model are indicated by dashed lines for comparison. Early in the cycle (until time  $\sim 3\tau$ ), horizontal surface velocities toward the trench (positive) are smaller than in the REF model, and upward velocities are higher. Later in the cycle (after  $\sim 5\tau$ ) this pattern changes around, that is, with smaller landward horizontal velocities and more pronounced subsidence rates. Surface velocities and the velocities in the rest of the model (cf. Figure 6) thus are sensitive to the thickness of the subducting plate at all stages of the earthquake cycle.

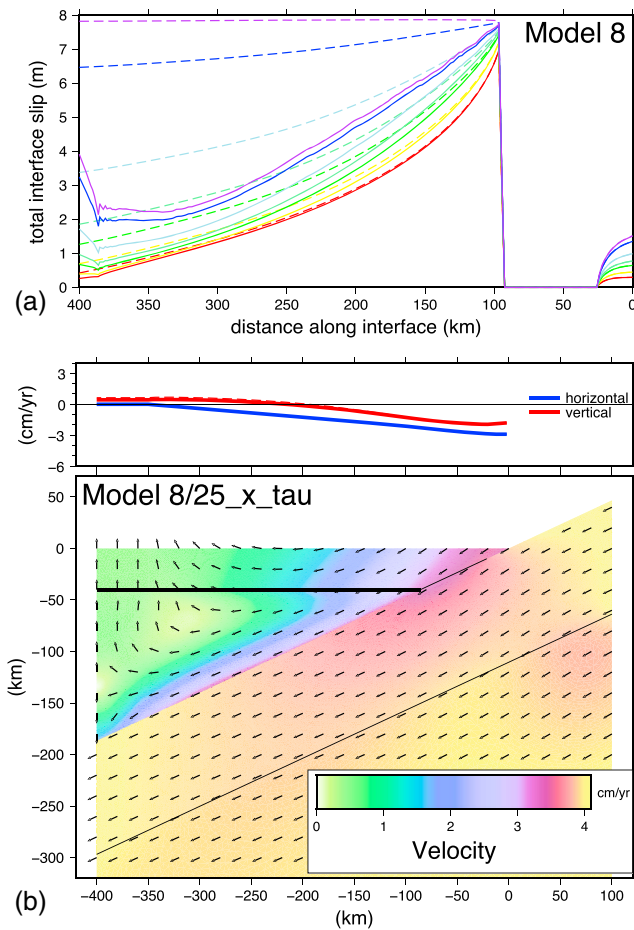


**Figure A3.** Results of Model 8, which has a 0.3 MPa shear stress on the deep shear zone. (a) Total slip on the interface at different times (color code same as Figure 3b). Dashed curves represent the REF model; solid curves are the results of Model 8. Afterslip (red curves) is nearly identical, but interface slip differs significantly in later parts of the cycle. (b) Velocities at  $t = 25\tau$ . A comparison with Figure 6f shows that the velocity field differs significantly along the slab-wedge interface, but this difference is not expressed at the surface.

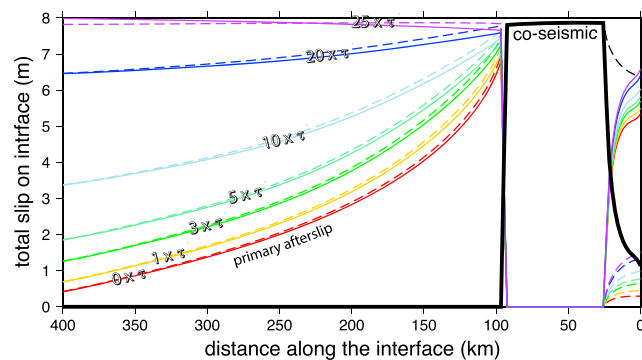


**Figure A4.** Interface slip evolution for Model 9 (solid curves), which has a high coseismic friction on the shallow interface (updip from the locked section). Dashed curves represent the REF model. Coseismic slip is much less than the reference model. This difference is compensated by primary afterslip.



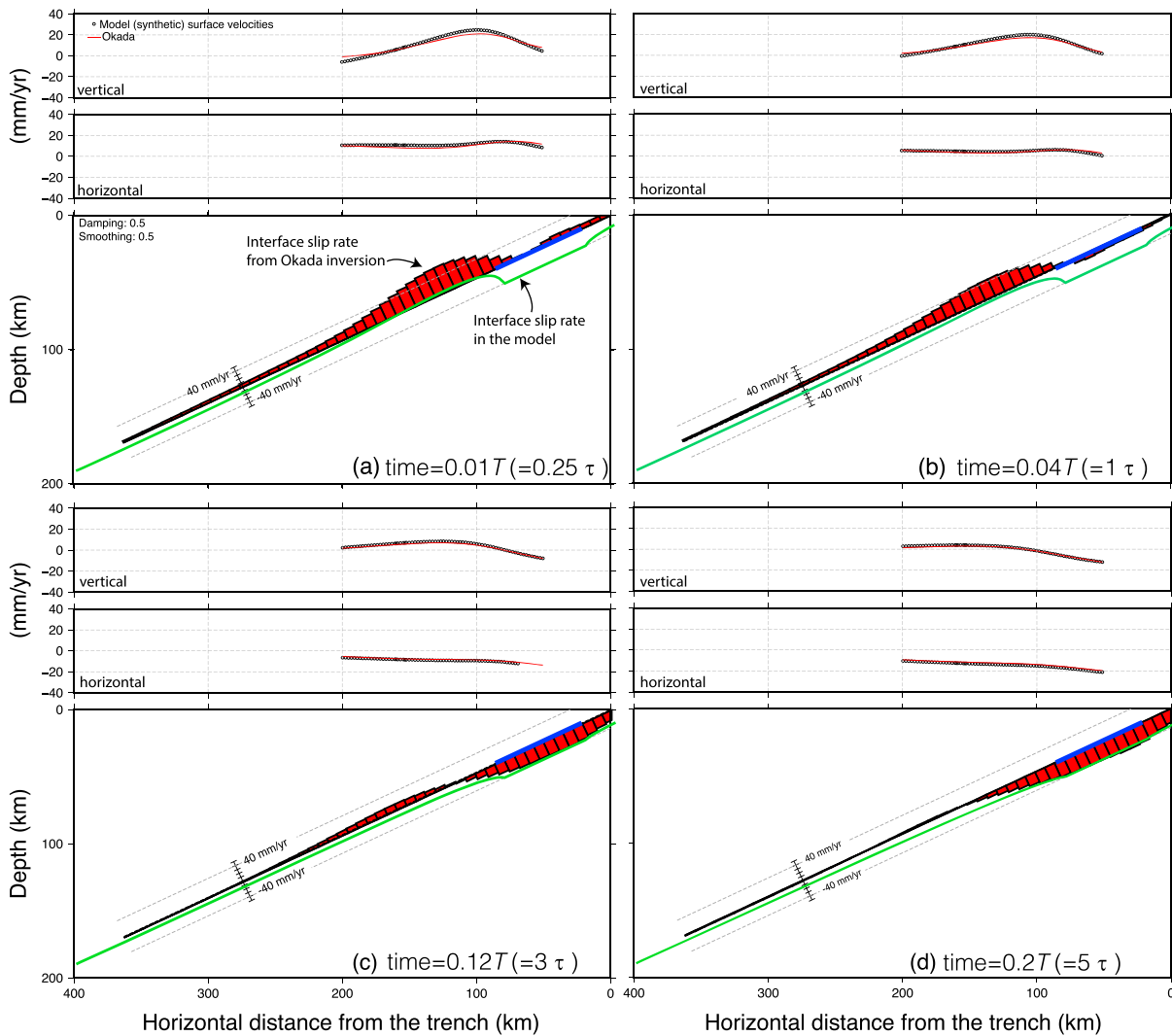


**Figure A5.** Results from a combined inversion (Okada) of the synthetic horizontal and vertical velocities of the REF model (Model 1). The aperture of the network is more realistic than in Figure 15, with benchmarks from 50 km away from the trench to the volcanic arc. The network is very dense and the synthetic data are noise free. (a) Time=0.01T. Top (middle) panel shows vertical (horizontal) velocities of Model 1 and of the Okada model. The bottom panel shows the inverted interface slip rate (red bars) and the actual interface slip rate in Model 1 (minus the back slip rate of 40 mm/yr, green line). Ideally, the red bar diagram would follow the green line but full locking of the coseismic fault (blue line) is clearly not reproduced as 40 mm/yr back slip by the inversion. (b) Time = 0.04 T. (c) Time = 0.12 T. (d) Time = 0.2 T. After the postseismic period ( $5\tau$  and thereafter) the back slip rate on the updip and locked parts of the interface are well reproduced by the inversion. Back slip on the deep interface below the locking depth is never correctly reproduced.

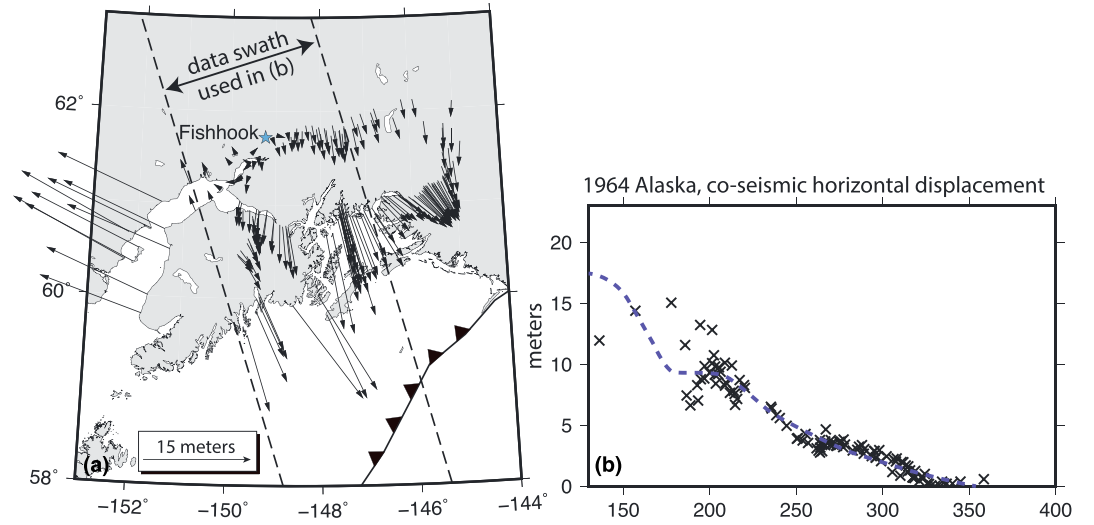


**Figure A6.** Horizontal coseismic displacements from the Alaska 1964 earthquake relative to fishhook (Snay et al., 1987). The blue dashed line shows the prediction of our generic model.

is proportional to the shear modulus  $\mu$ ; this represents the material resistance to shape change. In a viscoelastic material, imposed shear stresses relax by incompressible viscous shear flow at a rate that is controlled by the (shear) viscosity  $\eta$ . The characteristic relaxation time ("Maxwell time") of a viscoelastic material is

$$\tau = 2\eta/\mu \quad (\text{A1})$$

A corollary of our plane strain approximation is that the relaxation time  $\tau_R = 2(1 - \nu)\tau$ , that is, it is 50% longer than the Maxwell time when we select a Poisson's ratio  $\nu = 0.25$  (Melosh & Raefsky, 1983).

The overriding plate in our models is purely elastic. It shows flexural behavior during the earthquake cycle. The resistance of a beam to flexure (in 2-D) is controlled by the flexural rigidity

$$D = \frac{EH^3}{12(1 - \nu^2)} \quad (\text{A2})$$

where  $E$  is Young's modulus and  $H$  is beam thickness. An isotropic elastic material is defined by only two independent parameters, and the shear and bulk modulus are related to Young's modulus and Poisson's ratio:

$$\mu = \frac{E}{2(1 + \nu)} \quad K = \frac{E}{3(1 - 2\nu)} \quad (\text{A3})$$

In the REF model,  $E = 50$  GPa,  $\nu = 0.25$ ,  $\mu = 20$  GPa,  $K = 33.3$  GPa, and  $\eta = 5 \cdot 10^{18}$  Pa s.

#### A1.2. Sensitivity of the REF Model to Variations in Elastic and Viscoelastic Properties

Equation (A3) show that increasing Young's modulus  $E$  by a factor of 10 results in the same increase in the shear and bulk moduli ( $\mu$  and  $K$ ). Equations (A1) and (A2) show that a concurrent increase of the viscosity by a factor of 10 causes both relaxation times to come out the same. As is clear from (A3), the flexural rigidity changes significantly with an increase of  $E$  by a factor of 10. We verified this in a model where we increased  $E$  and  $\eta$  by a factor of 10 in the mantle wedge and subslab asthenosphere. We do not show the results here because they are identical.

To bring out the sensitivity of the results of the REF model to earthquake induced shear strains in the mantle wedge and subslab asthenosphere, we decreased  $\mu = 11.1$  GPa—we keep the bulk modulus at the value of the REF model (the corresponding value for Poisson's ratio  $\nu = 0.35$  is near the upper bound for rocks). Shear strains therefore result in smaller shear stresses. To avoid an increase of the Maxwell time (and therefore a decrease of the time ratio  $T/\tau$ ), we decrease the viscosity to match, that is,  $\eta = 2.78 \cdot 10^{18}$  Pa s. The resulting surface velocities and displacements are only slightly different. Afterslip velocities on the downdip end of the interface initially are slightly higher than in the REF model, become

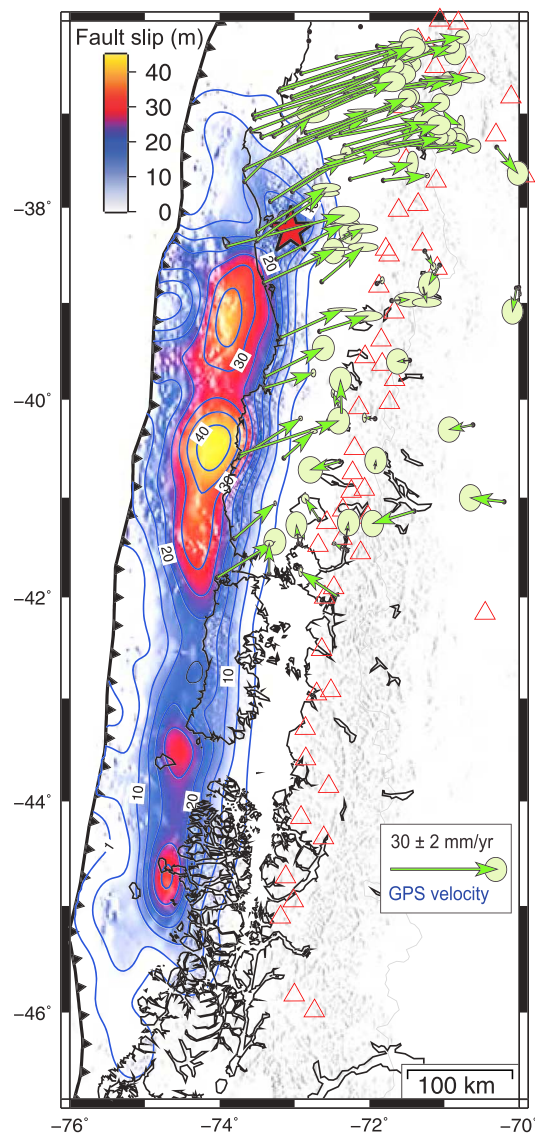


**Figure A7.** Coseismic slip of the 1960 Valdivia  $M_w$  9.5 earthquake from Moreno et al. (2009) and horizontal velocities before the 2010 Maule event (to the north of 38°S) relative to stable South America (Moreno et al., 2010). Red triangles indicate active volcanoes. GNSS velocities along the coast near the high-slip patches are directed landward, and velocities further to the east are directed trenchward. Such convergence agrees qualitatively with our model prediction during the postseismic relaxation period.

up to 20% lower by  $5 \times \tau$ , and the difference goes to zero after that. We conclude that the sensitivity to coseismic shear strains is moderate.

With a next model we aim to bring out the sensitivity of the results to lateral pressure variations. We retain  $\mu = 20$  GPa and reduce the bulk modulus  $K = 21.9$  GPa in the mantle wedge and subslab asthenosphere (the corresponding value for Poisson's ratio  $\nu = 0.15$  is at the lower extreme of what is realistic for rocks). Volume changes therefore result in smaller pressure gradients. The resulting coseismic slip, the primary after-slip, stress, and displacement fields are nearly identical to the REF model. Postseismic velocities are different shortly after the earthquake, and the difference decays away largely within  $1 \times \tau$ . The results are largely insensitive to the elastic bulk modulus of the wedge and subslab asthenosphere.

The influence of contrasts in the compliance of the overriding and subducting plate is investigated in a next model. We change the REF model by lowering the Young's modulus of the overriding plate to  $E = 42.5$  GPa

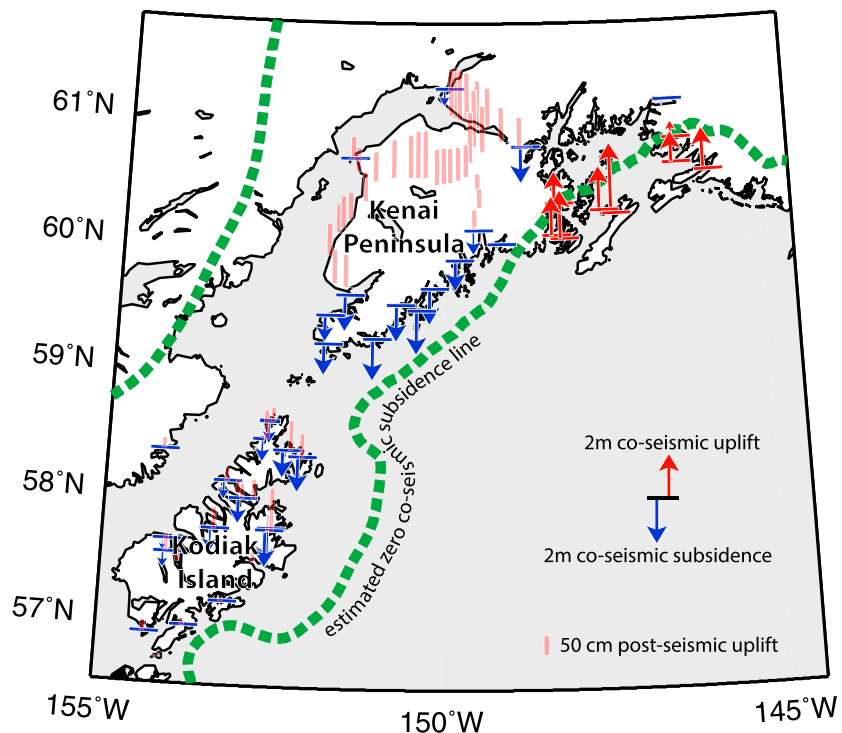


**Figure A8.** Coseismic vertical displacement observations for 1964 Alaska event from Plafker (1972) (red and blue arrows) and his estimated lines of zero subsidence (dashed green lines). Red bars show postseismic uplift after 29 years on Kodiak Island (collected by Gilpin, 1995, published in Suito & Freymueller, 2009), and after 35 years on Kenai peninsula (Cohen & Freymueller, 2004). The region of coseismic subsidence still experiences postseismic uplift. Our model results are consistent with this observation.

and increasing Poisson's ratio to  $\nu = 0.45$ , so that the flexural rigidity remains the same. The kinematic results (displacement, earthquake slip, afterslip, and velocities) turn out to be largely insensitive to the elasticity contrast; only near the trench are vertical velocities affected shortly after the earthquake. Stresses are approximately similar too.

#### Acknowledgments

Author contributions following the CReDiT taxonomy: Conceptualization: R. G. and K. P. F.; Data Curation: R. G.; Investigation: R. G. and M. W. H.; Methodology: R. G. and M. W. H.; Resources and Software: R. G. and L. v. d. W.; Validation: R. G.; Supervision: R. G. and K. P. F.; Visualization: R. G. and M. W. H.; Writing: R. G., T.B., and M. W. H. Input and output files and the software source codes that were used for the models of this paper are digitally stored at Utrecht University. Files are accessible at <ftp://ftp.geo.uu.nl/pub/people/govers/2017RevGeophys/>. We gratefully acknowledge constructive comments by Editor-in-Chief Fabio Florindo, Thorne Lay, Wouter Schellart, and an anonymous reviewer that helped to improve an earlier version of the manuscript.

#### References

- Altamimi, Z., Collilieux, X., & Metivier, L. (2011). ITRF2008: An improved solution of the international terrestrial reference frame. *Journal of Geodesy*, 85, 457–473. <https://doi.org/10.1007/s00190-011-0444-4>
- Altamimi, Z., Métivier, L., & Collilieux, X. (2012). ITRF2008 plate motion model. *Journal of Geophysical Research*, 117, B07402. <https://doi.org/10.1029/2011JB008930>
- Ammon, C., Ji, C., Thio, H., Robinson, D., Ni, S., Hjorleifsdottir, V., ... Wald, D. (2005). Rupture process of the 2004 Sumatra-Andaman earthquake. *Science*, 308, 1133–1139. <https://doi.org/10.1126/science.1112260>
- Ammon, C. J., Lay, T., Kanamori, H., & Cleveland, M. (2011). A rupture model of the 2011 off the Pacific coast of Tohoku Earthquake. *Earth Planets and Space*, 63(7), 693–696. <https://doi.org/10.5047/eps.2011.05.015>
- Anderson, E., Bai, Z., Bischof, C., Blackford, S., Demmel, J., Dongarra, J., ... Sorensen, D. (1999). *LAPACK Users' Guide* (3rd ed.). Philadelphia, PA: Society for Industrial and Applied Mathematics. <https://doi.org/10.1137/1.9780898719604>
- Argus, D. F., Gordon, R. G., & DeMets, C. (2011). Geologically current motion of 56 plates relative to the no-net-rotation reference frame. *Geochemistry, Geophysics, Geosystems*, 12, Q11001. <https://doi.org/10.1029/2011GC003751>
- Aron, F., Allmendinger, R. W., Cembrano, J., González, G., & Yanez, G. (2013). Permanent fore-arc extension and seismic segmentation: Insights from the 2010 Maule earthquake, Chile. *Journal of Geophysical Research: Solid Earth*, 118, 724–739. <https://doi.org/10.1029/2012JB009339>
- Aron, F., Cembrano, J., Astudillo, F., Allmendinger, R. W., & Arancibia, G. (2015). Constructing forearc architecture over megathrust seismic cycles: Geological snapshots from the Maule earthquake region, Chile. *Geological Society of America Bulletin*, 127(3–4), 464–479. <https://doi.org/10.1130/B31125.1>
- Arriagada, C., Arancibia, G., Cembrano, J., Martínez, F., Carrizo, D., Van Sint Jan, M., ... Yañez, G. (2011). Nature and tectonic significance of co-seismic structures associated with the Mw 8.8 Maule earthquake, central-southern Chile forearc. *Journal of Structural Geology*, 33, 891–897. <https://doi.org/10.1016/j.jsg.2011.03.004>
- Asano, Y., Saito, T., Ito, Y., Shiomi, K., Hirose, H., Matsumoto, T., ... Sekiguchi, S. (2011). Spatial distribution and focal mechanisms of aftershocks of the 2011 off the Pacific coast of Tohoku earthquake. *Earth, Planets and Space*, 63, 669–673. <https://doi.org/10.5047/eps.2011.06.016>

- Avouac, J.-P. (2015). From geodetic imaging of seismic and aseismic fault slip to dynamic modeling of the seismic cycle. *Annual Review of Earth and Planetary Sciences*, 43(1), 233–271. <https://doi.org/10.1146/annurev-earth-060614-105302>
- Banerjee, P., Pollitz, F., Nagarajan, B., & Bürgmann, R. (2007). Coseismic slip distributions of the 26 December 2004 Sumatra-Andaman and 28 March 2005 Nias earthquakes from GPS static offsets. *Bulletin of the Seismological Society of America*, 97(1A), S86–S102. <https://doi.org/10.1785/0120050609>
- Barrientos, S., Plafker, G., & Lorca, E. (1992). Postseismic coastal uplift in southern Chile. *Geophysical Research Letters*, 19(7), 701–704. <https://doi.org/10.1029/92GL00210>
- Barrientos, S., & Ward, S. N. (1990). The 1960 Chile earthquake: Inversion for slip distribution from surface deformation. *Geophysical Journal International*, 103(3), 589–598. <https://doi.org/10.1111/j.1365-246X.1990.tb05673.x>
- Beck, S. L., & Christensen, D. H. (1991). Rupture process of the February 4, 1965, Rat Islands earthquake. *Journal of Geophysical Research*, 96(B2), 2205–2221. <https://doi.org/10.1029/90JB02092>
- Bedford, J., Moreno, M., Baez, J. C., Lange, D., Tilmann, F., Rosenau, M., ... Vigny, C. (2013). A high-resolution, time-variable afterslip model for the 2010 Maule  $M_w = 8.8$ , Chile megathrust earthquake. *Earth and Planetary Science Letters*, 383(C), 26–36. <https://doi.org/10.1016/j.epsl.2013.09.020>
- Bedford, J., Moreno, M., Li, S., Oncken, O., Baez, J. C., Bevis, M., ... Lange, D. (2016). Separating simultaneous postseismic processes: An application of the postseismic straightening method to the Maule 2010 cGPS. *Journal of Geophysical Research: Solid Earth*, 121, 7618–7638. <https://doi.org/10.1002/2016JB013093>
- Billham, R., Engdahl, R., Feldl, N., & Satyabala, S. P. (2005). Partial and complete rupture of the Indo-Andaman plate boundary 1847–2004. *Seismological Research Letters*, 76, 299–311. <https://doi.org/10.1785/gssrl.76.3.299>
- Bletery, Q., Thomas, A. M., Rempel, A. W., Karlstrom, L., Sladen, A., & De Barros, L. (2016). Mega-earthquakes rupture flat megathrusts. *Science*, 354(6315), 1027–1031. <https://doi.org/10.1126/science.aag0482>
- Blewitt, G., Kreemer, C., Hammond, W. C., & Gazeaux, J. (2016). MIDAS robust trend estimator for accurate GPS station velocities without step detection. *Journal of Geophysical Research: Solid Earth*, 121, 2054–2068. <https://doi.org/10.1002/2015JB012552>
- Briggs, R. W., Engelhart, S. E., Nelson, A. R., Dura, T., Kemp, A. C., Haeussler, P. J., ... Bradley, L. A. (2014). Uplift and subsidence reveal a nonpersistent megathrust rupture boundary (Sitkinak Island, Alaska). *Geophysical Research Letters*, 41, 2289–2296. <https://doi.org/10.1002/2014GL059380>
- Broerse, T., Riva, R., Simons, W., Govers, R., & Vermeersen, B. (2015). Postseismic GRACE and GPS observations indicate a rheology contrast above and below the Sumatra slab. *Journal of Geophysical Research: Solid Earth*, 120, 5343–5361. <https://doi.org/10.1002/2015JB011951>
- Chlieh, M., Avouac, J. P., Hjorleifsdottir, V., Song, T. R. A., Ji, C., Sieh, K., ... Galetzka, J. (2007). Coseismic slip and Afterslip of the great  $M_w$  9.15 Sumatra-Andaman earthquake of 2004. *Bulletin of the Seismological Society of America*, 97, S152–S173. <https://doi.org/10.1785/0120050631>
- Chlieh, M., Avouac, J. P., Sieh, K., Natawidjaja, D. H., & Galetzka, J. (2008). Heterogeneous coupling of the Sumatran megathrust constrained by geodetic and paleogeodetic measurements. *Journal of Geophysical Research*, 113, B05305. <https://doi.org/10.1029/2007JB004981>
- Christensen, D. H., & Beck, S. L. (1994). The rupture process and tectonic implications of the great 1964 Prince William Sound earthquake. *Pure and Applied Geophysics*, 142(1), 29–53. <https://doi.org/10.1007/BF00875967>
- Cifuentes, I. L., & Silver, P. G. (1989). Low-frequency source characteristics of the great 1960 Chilean earthquake. *Journal of Geophysical Research*, 94(B1), 643–663. <https://doi.org/10.1029/JB094iB01p00643>
- Cohen, S. C. (1994). Evaluation of the importance of model features for cyclic deformation due to dip-slip faulting. *Geophysical Journal International*, 119(3), 831–841. <https://doi.org/10.1111/j.1365-246X.1994.tb04020.x>
- Cohen, S. C. (1999). Numerical models of crustal deformation in seismic zones. In R. Dmowska & B. Saltzman (Eds.), *Advances in Geophysics* (Vol. 41, pp. 131–232). San Diego, CA: Academic Press.
- Cohen, S. C., & Freymueller, J. T. (2004). Crustal deformation in southcentral Alaska: The 964 Prince William sound earthquake subduction zone. In *Advances in Geophysics* 47 (pp. 1–58). Amsterdam: Elsevier. [https://doi.org/10.1016/S0065-2687\(04\)47001-0](https://doi.org/10.1016/S0065-2687(04)47001-0)
- Constable, S. C., Parker, R. L., & Constable, C. G. (1987). Occams inversion: A practical algorithm of generating smooth models from electromagnetic sounding data. *Geophysics*, 52(3), 289–300. <https://doi.org/10.1190/1.1442303>
- Cross, R. S., & Freymueller, J. T. (2008). Evidence for and implications of a Bering plate based on geodetic measurements from the Aleutians and western Alaska. *Journal of Geophysical Research*, 113, B07405. <https://doi.org/10.1029/2007JB005136>
- Darwin, C. (1846). *Geological Observations on South America*. London: Smith, Elder and Co.
- Delouis, B., Nocquet, J.-M., & Vallée, M. (2010). Slip distribution of the February 27, 2010  $M_w = 8.8$  Maule earthquake, central Chile, from static and high-rate GPS, InSAR, and broadband teleseismic data. *Geophysical Research Letters*, 37, L17305. <https://doi.org/10.1029/2010GL043899>
- Delouis, B., Philip, H., Dorbath, L., & Cisternas, A. (1998). Recent crustal deformation in the Antofagasta region (northern Chile) and the subduction process. *Geophysical Journal International*, 132(2), 302–338. <https://doi.org/10.1046/j.1365-246x.1998.00439.x>
- Diao, F., Xiong, X., Wang, R., Zheng, Y., Walter, T. R., Weng, H., & Li, J. (2013). Overlapping post-seismic deformation processes: Afterslip and viscoelastic relaxation following the 2011  $M_w$  9.0 Tohoku (Japan) earthquake. *Geophysical Journal International*, 196(1), 218–229. <https://doi.org/10.1093/gji/ggt376>
- Ding, M., & Lin, J. (2014). Post-seismic viscoelastic deformation and stress transfer after the 1960  $M_9.5$  Valdivia, Chile earthquake: Effects on the 2010  $M_{8.8}$  Maule, Chile earthquake. *Geophysical Journal International*, 197(2), 697–704. <https://doi.org/10.1093/gji/ggu048>
- Doin, M., & Fleitout, L. (1996). Thermal evolution of the oceanic lithosphere: An alternative view. *Earth and Planetary Science Letters*, 142(1–2), 121–136. [https://doi.org/10.1016/0012-821X\(96\)00082-9](https://doi.org/10.1016/0012-821X(96)00082-9)
- Dragert, H., Wang, K., & Rogers, G. (2004). Geodetic and seismic signatures of episodic tremor and slip in the northern Cascadia subduction zone. *Earth, Planets and Space*, 56, 1143–1150. <https://doi.org/10.1186/BF03353333>
- Fariás, M., Comte, D., Roecker, S., Carrizo, D., & Pardo, M. (2011). Crustal extensional faulting triggered by the 2010 Chilean earthquake: The Pichilemu seismic sequence. *Tectonics*, 30, TC6010. <https://doi.org/10.1029/2011TC002888>
- Fournier, T. J., & Freymueller, J. T. (2007). Transition from locked to creeping subduction in the Shumagin region, Alaska. *Geophysical Research Letters*, 34, L06303. <https://doi.org/10.1029/2006GL029073>
- Freed, A. M., Hashima, A., Becker, T. W., Okaya, D. A., Sato, H., & Hatanaka, Y. (2017). Resolving depth-dependent subduction zone viscosity and afterslip from postseismic displacements following the 2011 Tohoku-oki, Japan earthquake. *Earth and Planetary Science Letters*, 459, 279–290. <https://doi.org/10.1016/j.epsl.2016.11.040>
- Freymueller, J. T., Woodard, H., Cohen, S. C., Cross, R. S., Elliott, J. R., Larsen, C. F., ... Zweck, C. (2008). Active deformation processes in Alaska, based on 15 years of GPS measurements. In J. T. Freymueller, P. J. Haeussler, & R. L. Wesson (Eds.), *Active Tectonics and Seismic Potential of Alaska, Geophysical Monograph Series* (Vol. 179, pp. 1–42). Washington, DC: American Geophysical Union. <https://doi.org/10.1029/179GM02>



- Gahalaut, V. K., Jade, S., Catherine, J. K., Gireesh, R., Ananda, M. B., Kumar, P., ... Kumar, S. (2008). GPS measurements of postseismic deformation in the Andaman-Nicobar region following the giant 2004 Sumatra-Andaman earthquake. *Journal of Geophysical Research*, 113, B08401. <https://doi.org/10.1029/2007JB005511>
- Gahalaut, V. K., Nagarajan, B., Catherine, J. K., & Kumar, S. (2006). Constraints on 2004 Sumatra-Andaman earthquake rupture from GPS measurements in Andaman-Nicobar Islands. *Earth and Planetary Science Letters*, 242(3-4), 365-374. <https://doi.org/10.1016/j.epsl.2005.11.051>
- Gilpin, L. M. (1995). Holocene paleoseismicity and coastal tectonics of the Kodiak Islands, Alaska (PhD thesis). Santa Cruz: University of California.
- Govers, R., & Wortel, M. J. R. (1993). Initiation of asymmetric extension in continental lithosphere. *Tectonophysics*, 223(1-2), 75-96. [https://doi.org/10.1016/0040-1951\(93\)90159-H](https://doi.org/10.1016/0040-1951(93)90159-H)
- Govers, R., & Wortel, M. (2005). Lithosphere tearing at STEP faults: Response to edges of subduction zones. *Earth and Planetary Science Letters*, 236(1-2), 505-523. <https://doi.org/10.1016/j.epsl.2005.03.022>
- Gutenberg, B., & Richter, C. F. (1954). *Seismicity of the Earth*. Princeton, NJ: Princeton University Press.
- Han, S.-C., Sauber, J., Luthcke, S. B., Ji, C., & Pollitz, F. F. (2008). Implications of postseismic gravity change following the great 2004 Sumatra-Andaman earthquake from the regional harmonic analysis of GRACE intersatellite tracking data. *Journal of Geophysical Research*, 113, B11413. <https://doi.org/10.1029/2008JB005705>
- Hashimoto, C., Noda, A., Sagiya, T., & Matsu'ura, M. (2009). Interplate seismogenic zones along the Kuril-Japan trench inferred from GPS data inversion. *Nature Geoscience*, 2(2), 141-144. <https://doi.org/10.1038/NGEO421>
- Hayes, G. P. (2014). Continuing megathrust earthquake potential in Chile after the 2014 Iquique earthquake. *Nature*, 512(7514), 295-298. <https://doi.org/10.1038/nature13677>
- Hetland, E. A., & Simons, M. (2010). Post-seismic and interseismic fault creep II: Transient creep and interseismic stress shadows on megathrusts. *Geophysical Journal International*, 181(1), 99-112. <https://doi.org/10.1111/j.1365-246X.2009.04482.x>
- Hicks, S. P., Rietbrock, A., Ryder, I. M. A., Lee, C.-S., & Miller, M. (2014). Anatomy of a megathrust: The 2010 M8.8 Maule, Chile earthquake rupture zone imaged using seismic tomography. *Earth and Planetary Science Letters*, 405, 142-155. <https://doi.org/10.1016/j.epsl.2014.08.028>
- Hirahara, K. (2002). Interplate earthquake fault slip during periodic earthquake cycles in a viscoelastic medium at a subduction zone. *Pure and Applied Geophysics*, 159, 2001-2220.
- Hoehner, A., Babeyko, A. Y., & Sobolev, S. V. (2008). Enhanced GPS inversion technique applied to the 2004 Sumatra earthquake and tsunami. *Geophysical Research Letters*, 35, L08310. <https://doi.org/10.1029/2007GL033133>
- Hoehner, A., Sobolev, S. V., Einarsson, I., & Wang, R. (2011). Investigation on afterslip and steady state and transient rheology based on postseismic deformation and geoid change caused by the Sumatra 2004 earthquake. *Geochemistry, Geophysics, Geosystems*, 12, Q07010. <https://doi.org/10.1029/2010GC003450>
- Holdahl, S. R., & Sauber, J. (1994). Coseismic slip in the 1964 Prince William Sound earthquake: A new geodetic inversion. *Pure and Applied Geophysics*, 142(1), 55-82. <https://doi.org/10.1007/BF00875968>
- Hooper, A., Pietrzak, J., Simons, W., Cui, H., Riva, R., Naeije, M., ... Socquet, A. (2013). Importance of horizontal seafloor motion on tsunami height for the 2011  $M_w=9.0$  Tohoku-Oki earthquake. *Earth and Planetary Science Letters*, 361(c), 469-479. <https://doi.org/10.1016/j.epsl.2012.11.013>
- Hsu, Y.-J., Simons, M., Avouac, J.-P., Galetzka, J., Sieh, K., Chlieh, M., ... Bock, Y. (2006). Frictional afterslip following the 2005 Nias-Simeulue earthquake, Sumatra. *Science*, 312(5782), 1921-1926. <https://doi.org/10.1126/science.1126960>
- Hu, Y., Bürgmann, R., Freymueller, J. T., Banerjee, P., & Wang, K. (2014). Contributions of poroelastic rebound and a weak volcanic arc to the postseismic deformation of the 2011 Tohoku earthquake. *Earth, Planets and Space*, 66(1), 106-110. <https://doi.org/10.1186/1880-5981-66-106>
- Hu, Y., Bürgmann, R., Uchida, N., Banerjee, P., & Freymueller, J. T. (2016). Stress-driven relaxation of heterogeneous upper mantle and time-dependent afterslip following the 2011 Tohoku earthquake. *Journal of Geophysical Research: Solid Earth*, 121, 385-411. <https://doi.org/10.1002/2015JB012508>
- Hu, Y., & Wang, K. (2012). Spherical-Earth finite element model of short-term postseismic deformation following the 2004 Sumatra earthquake. *Journal of Geophysical Research*, 117, B05404. <https://doi.org/10.1029/2012JB009153>
- Hu, Y., Wang, K., He, J., Klotz, J., & Khazardze, G. (2004). Three-dimensional viscoelastic finite element model for postseismic deformation of the great 1960 Chile earthquake. *Journal of Geophysical Research*, 109, B12403. <https://doi.org/10.1029/2004JB003163>
- Hughes, K. L. H., Masterlark, T., & Mooney, W. D. (2010). Poroelastic stress-triggering of the 2005 M8.7 Nias earthquake by the 2004 M9.2 Sumatra-Andaman earthquake. *Earth and Planetary Science Letters*, 293(3-4), 289-299. <https://doi.org/10.1016/j.epsl.2010.02.043>
- Ichinose, G., Somerville, P., Thio, H. K., Graves, R., & O'Connell, D. (2007). Rupture process of the 1964 Prince William Sound, Alaska, earthquake from the combined inversion of seismic, tsunami, and geodetic data. *Journal of Geophysical Research*, 112, B07306. <https://doi.org/10.1029/2006JB004728>
- Ide, S., Baltay, A., & Beroza, G. C. (2011). Shallow dynamic overshoot and energetic deep rupture in the 2011  $M_w$  9.0 Tohoku-Oki earthquake. *Science*, 332(6036), 1426-1429. <https://doi.org/10.1126/science.1207020>
- Ito, Y., Tsuji, T., Osada, Y., Kido, M., Inazu, D., Hayashi, Y., ... Fujimoto, H. (2011). Frontal wedge deformation near the source region of the 2011 Tohoku-Oki earthquake. *Geophysical Research Letters*, 38, L00G05. <https://doi.org/10.1029/2011GL048355>
- Jarrard, R. D. (1986). Relations among subduction parameters. *Reviews of Geophysics*, 24(2), 217-284. <https://doi.org/10.1029/RG024i002p00217>
- Johnson, K. M., Fukuda, J., & Segall, P. (2012). Challenging the rate-state asperity model: Afterslip following the 2011 M9 Tohoku-oki, Japan, earthquake. *Geophysical Research Letters*, 39, L20302. <https://doi.org/10.1029/2012GL052901>
- Johnson, J. M., & Satake, K. (1994). Rupture extent of the 1938 Alaskan earthquake as inferred from tsunami waveforms. *Geophysical Research Letters*, 21(8), 733-736. <https://doi.org/10.1029/94GL00333>
- Johnson, J. M., & Satake, K. (1997). Estimation of seismic moment and slip distribution of the April 1, 1946, Aleutian tsunami earthquake. *Journal of Geophysical Research*, 102(B6), 11,765-11,774. <https://doi.org/10.1029/97JB00274>
- Jónsson, S., Segall, P., Pedersen, R., & Björnsson, G. (2003). Post-earthquake ground movements correlated to pore-pressure transients. *Nature*, 424(6945), 179-183. <https://doi.org/10.1038/nature01776>
- Kanamori, H. (1977). The energy release in great earthquakes. *Journal of Geophysical Research*, 82(20), 2981-2987. <https://doi.org/10.1029/JB082i020p02981>
- Karato, S.-I., Jung, H., Katayama, I., & Skemer, P. (2008). Geodynamic significance of seismic anisotropy of the upper mantle: New insights from laboratory studies. *Annual Review of Earth and Planetary Sciences*, 36, 59-95. <https://doi.org/10.1146/annurev.earth.36.031207.124120>

- Kato, A., Igarashi, T., Obara, K., Sakai, S., Takeda, T., Saiga, A., ... Yamada, T. (2013). Imaging the source regions of normal faulting sequences induced by the 2011 M9.0 Tohoku-Oki earthquake. *Geophysical Research Letters*, 40, 273–278. <https://doi.org/10.1002/grl.50104>
- Kato, A., Sakai, S., & Obara, K. (2011). A normal-faulting seismic sequence triggered by the 2011 off the Pacific coast of Tohoku earthquake: Wholesale stress regime changes in the upper plate. *Earth, Planets and Space*, 63, 745–748. <https://doi.org/10.5047/eps.2011.06.014>
- Klein, E., Fleitout, L., Vigny, C., & Garau, J. D. (2016). Afterslip and viscoelastic relaxation model inferred from the large-scale post-seismic deformation following the 2010 Mw 8.8 Maule earthquake (Chile). *Geophysical Journal International*, 205(3), 1455–1472. <https://doi.org/10.1093/gji/ggw086>
- Kneller, E., Van Keken, P., Karato, S., & Park, J. (2005). B-type olivine fabric in the mantle wedge: Insights from high-resolution non-Newtonian subduction zone models. *Earth and Planetary Science Letters*, 237, 781–797. <https://doi.org/10.1016/j.epsl.2005.06.049>
- Koketsu, K., Yokota, Y., Nishimura, N., Yagi, Y., Miyazaki, S., Satake, K., ... Okada, T. (2011). A unified source model for the 2011 Tohoku earthquake. *Earth and Planetary Science Letters*, 310, 480–487. <https://doi.org/10.1016/j.epsl.2011.09.009>
- Lallemant, S., Heuret, A., & Boutelier, D. (2005). On the relationships between slab dip, back-arc stress, upper plate absolute motion, and crustal nature in subduction zones. *Geochemistry, Geophysics, Geosystems*, 6, Q09006. <https://doi.org/10.1029/2005GC000917>
- Larson, K. M., & Lisowski, M. (1994). Strain accumulation in the Shumagin Islands: Results of initial GPS measurements. *Geophysical Research Letters*, 21(6), 489–492. <https://doi.org/10.1029/94GL00417>
- Lay, T., Ammon, C. J., Kanamori, H., Xue, L., & Kim, M. J. (2011). Possible large near-trench slip during the 2011 M<sub>w</sub> 9.0 off the Pacific coast of Tohoku earthquake. *Earth, Planets and Space*, 63, 687–692. <https://doi.org/10.5047/eps.2011.05.033>
- Lay, T., Kanamori, H., Ammon, C. J., Hutko, A. R., Furlong, K., & Rivera, L. (2009). The 2006–2007 Kuril Islands great earthquake sequence. *Journal of Geophysical Research*, 114, B11308. <https://doi.org/10.1029/2008JB006280>
- Lay, T., Kanamori, H., Ammon, C. J., Nettles, M., Ward, S. N., Aster, R., ... Sipkin, S. (2005). The great Sumatra-Andaman earthquake of 26 December 2004. *Science*, 308, 1127–1133. <https://doi.org/10.1126/science.1112250>
- Levenberg, K. (1944). A method for the solution of certain non-linear problems in least squares. *Quarterly of Applied Mathematics*, 2(2), 164–168. <https://doi.org/10.1090/qam/10666>
- Li, S., Freymueller, J., & McCaffrey, R. (2016). Slow slip events and time-dependent variations in locking beneath Lower Cook Inlet of the Alaska-Aleutian subduction zone. *Journal of Geophysical Research: Solid Earth*, 121, 1060–1079. <https://doi.org/10.1002/2015JB012491>
- Li, S., Moreno, M., Bedford, J., Rosenau, M., Heidbach, O., Melnick, D., & Oncken, O. (2017). Postseismic uplift of the Andes following the 2010 Maule earthquake: Implications for mantle rheology. *Geophysical Research Letters*, 118, 3059–1776. <https://doi.org/10.1002/2016GL071995>
- Lomnitz, C. (2004). Major earthquakes of Chile: A historical survey, 1535–1960. *Seismological Research Letters*, 75, 368–378. <https://doi.org/10.1785/gssrl.75.3.368>
- López, A. M., & Okal, E. A. (2006). A seismological reassessment of the source of the 1946 Aleutian “tsunami” earthquake. *Geophysical Journal International*, 165, 835–849. <https://doi.org/10.1111/j.1365-246X.2006.02899.x>
- Lorito, S., Romano, F., Atzori, S., Tong, X., Avallone, A., McCloskey, J., ... Piatanesi, A. (2011). Limited overlap between the seismic gap and coseismic slip of the great 2010 Chile earthquake. *Nature Geoscience*, 4, 173–177. <https://doi.org/10.1038/ngeo1073>
- Loveless, J. P., Hoke, G. D., Allmendinger, R. W., González, G., Isacks, B. L., & Carrizo, D. A. (2005). Pervasive cracking of the northern Chilean Coastal Cordillera: New evidence for forearc extension. *Geology*, 33, 973–976. <https://doi.org/10.1130/G22004.1>
- Loveless, J. P., & Meade, B. J. (2010). Geodetic imaging of plate motions, slip rates, and partitioning of deformation in Japan. *Journal of Geophysical Research*, 115, B02410. <https://doi.org/10.1029/2008JB006248>
- Loveless, J. P., & Meade, B. J. (2016). Two decades of spatiotemporal variations in subduction zone coupling offshore Japan. *Earth and Planetary Science Letters*, 436, 19–30. <https://doi.org/10.1016/j.epsl.2015.12.033>
- Masterlark, T. (2003). Finite element model predictions of static deformation from dislocation sources in a subduction zone: Sensitivities to homogeneous, isotropic, Poisson-solid, and half-space assumptions. *Journal of Geophysical Research*, 108(B11), 2540. <https://doi.org/10.1029/2002JB002296>
- Matsu'ura, M., & Sato, T. (1989). A dislocation model for the earthquake cycle at convergent plate boundaries. *Geophysical Journal International*, 96(1), 23–32. <https://doi.org/10.1111/j.1365-246X.1989.tb05247.x>
- Meade, B. J., Klinger, Y., & Hetland, E. A. (2013). Inference of multiple earthquake-cycle relaxation timescales from irregular geodetic sampling of Interseismic deformation. *Bulletin of the Seismological Society of America*, 103(5), 2824–2835. <https://doi.org/10.1785/0120130006>
- Melnick, D. (2016). Rise of the central Andean coast by earthquakes straddling the Moho. *Nature Geoscience*, 9(5), 401–407. <https://doi.org/10.1038/ngeo2683>
- Melosh, H. J., & Raefsky, A. (1980). Dynamical origin of subduction zone topography. *Geophysical Journal of the Royal Astronomical Society*, 60(3), 333–354. <https://doi.org/10.1111/j.1365-246X.1980.tb04812.x>
- Melosh, H. J., & Raefsky, A. (1983). Anelastic response of the Earth to a dip slip earthquake. *Journal of Geophysical Research*, 88(B1), 515–526. <https://doi.org/10.1029/JB088iB01p00515>
- Melosh, H. J., & Williams, C. A. (1989). Mechanics of graben formation in crustal rocks: A finite element analysis. *Journal of Geophysical Research*, 94(B10), 13,961–13,973. <https://doi.org/10.1029/JB094iB10p13961>
- Meltzner, A. J., Sieh, K., Abrams, M., Agnew, D. C., Hudnut, K. W., Avouac, J.-P., & Natawidjaja, D. H. (2006). Uplift and subsidence associated with the great Aceh-Andaman earthquake of 2004. *Journal of Geophysical Research*, 111, B02407. <https://doi.org/10.1029/2005JB003891>
- Meltzner, A. J., Sieh, K., Chiang, H.-W., Shen, C.-C., Suwargadi, B. W., Natawidjaja, D. H., ... Galetzka, J. (2010). Coral evidence for earthquake recurrence and an A.D. 1390–1455 cluster at the south end of the 2004 Aceh–Andaman rupture. *Journal of Geophysical Research*, 115, B10402. <https://doi.org/10.1029/2010JB007499>
- Metois, M., Vigny, C., & Socquet, A. (2016). Interseismic coupling, megathrust earthquakes and seismic swarms along the Chilean subduction zone (38°–18°S). *Pure and Applied Geophysics*, 173(5), 1431–1449. <https://doi.org/10.1007/s00024-016-1280-5>
- Mikhailov, V., Lyakhovskaya, V., Panet, I., van Dinther, Y., Diamant, M., Gerya, T., ... Timoshkina, E. (2013). Numerical modelling of post-seismic rupture propagation after the Sumatra 26.12.2004 earthquake constrained by GRACE gravity data. *Geophysical Journal International*, 194(2), 640–650. <https://doi.org/10.1093/gji/ggt145>
- Miyazaki, S., Segall, P., Fukuda, J., & Kato, T. (2004). Space time distribution of afterslip following the 2003 Tokachi-oki earthquake: Implications for variations in fault zone frictional properties. *Geophysical Research Letters*, 31, L06623. <https://doi.org/10.1029/2003GL019410>
- Mizoguchi, K., Uehara, S.-I., & Ueta, K. (2012). Surface fault ruptures and slip distributions of the Mw 6.6 11 April 2011 Hamadoori, Fukushima prefecture, Northeast Japan, earthquake. *Bulletin of the Seismological Society of America*, 102, 1949–1956. <https://doi.org/10.1785/0120110308>
- Moreno, M. S., Bolte, J., Klotz, J., & Melnick, D. (2009). Impact of megathrust geometry on inversion of coseismic slip from geodetic data: Application to the 1960 Chile earthquake. *Geophysical Research Letters*, 36, L16310. <https://doi.org/10.1029/2009GL039276>

- Moreno, M., Rosenau, M., & Oncken, O. (2010). 2010 Maule earthquake slip correlates with pre-seismic locking of Andean subduction zone. *Nature*, 467(7312), 198–202. <https://doi.org/10.1038/nature09349>
- Nur, A., & Mavko, G. (1974). Postseismic viscoelastic rebound. *Science*, 183(4121), 204–206. <https://doi.org/10.1126/science.183.4121.204>
- Okada, Y. (1992). Internal deformation due to shear and tensile faults in a half-space. *Bulletin of the Seismological Society of America*, 82(2), 1018–1040.
- Ozawa, S., Nishimura, T., Munekane, H., Suito, H., Kobayashi, T., Tobita, M., & Imakiire, T. (2012). Preceding, coseismic, and postseismic slips of the 2011 Tohoku earthquake, Japan. *Journal of Geophysical Research*, 117, B07404. <https://doi.org/10.1029/2011JB009120>
- Ozawa, S., Nishimura, T., Suito, H., Kobayashi, T., Tobita, M., & Imakiire, T. (2011). Coseismic and postseismic slip of the 2011 magnitude-9 Tohoku-Oki earthquake. *Nature*, 475(7356), 373–376. <https://doi.org/10.1038/nature10227>
- Pacheco, J., Sykes, L., & Scholz, C. H. (1993). Nature of seismic coupling along simple plate boundaries of the subduction type. *Journal of Geophysical Research*, 98(B8), 14,133–14,159. <https://doi.org/10.1029/93JB00349>
- Panet, I., Pollitz, F., Mikhailov, V., Diamant, M., Banerjee, P., & Grijalva, K. (2010). Upper mantle rheology from GRACE and GPS postseismic deformation after the 2004 Sumatra-Andaman earthquake. *Geochemistry, Geophysics, Geosystems*, 11, Q06008. <https://doi.org/10.1029/2009GC002905>
- Papazachos, B., Scordilis, E., Panagiotopoulos, D., Papazachos, C., & Karakaisis, G. (2004). Global relations between seismic fault parameters and moment magnitude of earthquakes. *Bulletin of the Geological Society of Greece*, 36, 1482–1489.
- Parkin, E. J. (1972). Horizontal crustal movements. In *The Great Alaska Earthquake of 1964: Seismology and Geodesy* (pp. 419–434). Washington, DC: National Academy of Sciences.
- Paul, J., Rajendran, C. P., Lowry, A. R., Andrade, V., & Rajendran, K. (2012). Andaman Postseismic deformation observations: Still slipping after all these years? *Bulletin of the Seismological Society of America*, 102, 343–351. <https://doi.org/10.1785/0120110074>
- Perfettini, H., & Avouac, J. P. (2004). Stress transfer and strain rate variations during the seismic cycle. *Journal of Geophysical Research*, 109, B06402. <https://doi.org/10.1029/2003JB002917>
- Perfettini, H., & Avouac, J. P. (2014). The seismic cycle in the area of the 2011  $M_w$  9.0 Tohoku-Oki earthquake. *Journal of Geophysical Research: Solid Earth*, 119, 4469–4515. <https://doi.org/10.1002/2013JB010697>
- Perfettini, H., Avouac, J., Tavera, H., Kositsky, A., Nocquet, J., Bondoux, F., ... Soler, P. (2010). Seismic and aseismic slip on the Central Peru megathrust. *Nature*, 465, 78–81. <https://doi.org/10.1038/nature09062>
- Piersanti, A. (1999). Postseismic deformation in Chile: Constraints on the asthenospheric viscosity. *Geophysical Research Letters*, 26(20), 3157–3160. <https://doi.org/10.1029/1999GL005375>
- Piersanti, A., Spada, G., Sabadini, R., & Bonafede, M. (1995). Global post-seismic deformation. *Geophysical Journal International*, 120(3), 544–566. <https://doi.org/10.1111/j.1365-246X.1995.tb01838.x>
- Plafker, G. (1969). Tectonics of the March 27, 1964 Alaska earthquake. *U.S. Geological Survey Professional Paper*, 543–I. Retrieved from <https://pubs.usgs.gov/pp/0543i/>
- Plafker, G. (1972). Alaskan earthquake of 1964 and Chilean earthquake of 1960—Implications for arc tectonics. *Journal of Geophysical Research*, 77(5), 901–925. <https://doi.org/10.1029/JB077i005p00901>
- Plafker, G., & Savage, J. C. (1970). Mechanism of the Chilean earthquakes of May 21 and 22, 1960. *Geological Society of America Bulletin*, 81(4), 1001–1030. [https://doi.org/10.1130/0016-7606\(1970\)81%5B1001:MOTCE0%5D2.0.CO;2](https://doi.org/10.1130/0016-7606(1970)81%5B1001:MOTCE0%5D2.0.CO;2)
- Pollitz, F., Banerjee, P., Grijalva, K., Nagarajan, B., & Bürgmann, R. (2008). Effect of 3-D viscoelastic structure on post-seismic relaxation from the 2004  $M = 9.2$  Sumatra earthquake. *Geophysical Journal International*, 173, 189–204. <https://doi.org/10.1111/j.1365-246X.2007.03666.x>
- Pollitz, F. F., Brooks, B., Tong, X., Bevis, M. G., Foster, J. H., Bürgmann, R., ... Blanco M. (2011). Coseismic slip distribution of the February 27, 2010  $M_w$  8.8 Maule, Chile earthquake. *Geophysical Research Letters*, 38, L09309. <https://doi.org/10.1029/2011GL047065>
- Pollitz, F. F., Bürgmann, R., & Banerjee, P. (2006). Post-seismic relaxation following the great 2004 Sumatra-Andaman earthquake on a compressible self-gravitating Earth. *Geophysical Journal International*, 167, 397–420. <https://doi.org/10.1111/j.1365-246X.2006.03018.x>
- Pritchard, M. E., & Simons, M. (2006). An aseismic slip pulse in northern Chile and along-strike variations in seismogenic behavior. *Journal of Geophysical Research*, 111, B08405. <https://doi.org/10.1029/2006JB004258>
- Remy, D., Perfettini, H., Cotte, N., Avouac, J. P., Chlieh, M., Bondoux, F., ... Socquet, A. (2016). Postseismic reloading of the subduction megathrust following the 2007 Pisco, Peru, earthquake. *Journal of Geophysical Research: Solid Earth*, 121, 3978–3995. <https://doi.org/10.1002/2015JB012417>
- Ruegg, J., Rudloff, A., Vigny, C., Madariaga, R., de Chabaliar, J., Campos, J., ... Dimitrov, D. (2009). Interseismic strain accumulation measured by GPS in the seismic gap between Constitución and Concepción in Chile. *Physics of the Earth and Planetary Interiors*, 175, 78–85. <https://doi.org/10.1016/j.pepi.2008.02.015>
- Ruff, L., & Kanamori, H. (1980). Seismicity and the subduction process. *Physics of the Earth and Planetary Interiors*, 23(3), 240–252. [https://doi.org/10.1016/0031-9201\(80\)90117-X](https://doi.org/10.1016/0031-9201(80)90117-X)
- Ryder, I., Rietbrock, A., Kelson, K., Bürgmann, R., Floyd, M., Socquet, A., ... Carrizo, D. (2012). Large extensional aftershocks in the continental forearc triggered by the 2010 Maule earthquake, Chile. *Geophysical Journal International*, 188, 879–890. <https://doi.org/10.1111/j.1365-246X.2011.05321.x>
- Sagiya, T., Miyazaki, S., & Tada, T. (2000). Continuous GPS array and present-day crustal deformation of Japan. *Pure and Applied Geophysics*, 157(11–12), 2303–2322.
- Satirapod, C., Trisirisatayawong, I., Fleitout, L., Garau, J. D., & Simons, W. J. F. (2013). Vertical motions in Thailand after the 2004 Sumatra–Andaman earthquake from GPS observations and its geophysical modelling. *Advances in Space Research*, 51(8), 1565–1571. <https://doi.org/10.1016/j.asr.2012.04.030>
- Sato, M., Ishikawa, T., Ujihara, N., Yoshida, S., Fujita, M., Mochizuki, M., & Asada, A. (2011). Displacement above the hypocenter of the 2011 Tohoku-Oki earthquake. *Science*, 332, 1395–1395. <https://doi.org/10.1126/science.1207401>
- Savage, J. C. (1983). A dislocation model of strain accumulation and release at a subduction zone. *Journal of Geophysical Research*, 88(B6), 4984–4996. <https://doi.org/10.1029/JB088iB06p04984>
- Savage, J. C., & Hastie, L. M. (1966). Surface deformation associated with dip-slip faulting. *Journal of Geophysical Research*, 71(20), 4897–4904. <https://doi.org/10.1029/JZ071i020p04897>
- Savage, J., & Prescott, W. H. (1978). Asthenosphere readjustment and the earthquake cycle. *Journal of Geophysical Research*, 83(B7), 3369–3376. <https://doi.org/10.1029/JB083iB07p03369>
- Schellart, W. P., & Rawlinson, N. (2013). Global correlations between maximum magnitudes of subduction zone interface thrust earthquakes and physical parameters of subduction zones. *Physics of the Earth and Planetary Interiors*, 225, 41–67. <https://doi.org/10.1016/j.pepi.2013.10.001>
- Schwartz, S., & Rokosky, J. (2007). Slow slip events and seismic tremor at circum-Pacific subduction zones. *Reviews of Geophysics*, 45, RG3004. <https://doi.org/10.1029/2006RG000208>

- Scott, C. P., Allmendinger, R. W., González, G., & Loveless, J. P. (2016). Coseismic extension from surface cracks reopened by the 2014 Pisagua, northern Chile, earthquake sequence. *Geology*, 44(5), 387–390. <https://doi.org/10.1130/G37662.1>
- Segall, P. (2010). *Earthquake and Volcano Deformation*. Princeton: Princeton University Press. <https://doi.org/10.1515/9781400833856>
- Sieh, K., Natawidjaja, D. H., Meltzner, A. J., Shen, C.-C., Cheng, H., Li, K.-S., ... Edwards, R. L. (2008). Earthquake Supercycles inferred from sea-level changes recorded in the corals of West Sumatra. *Science*, 322, 1674–1678. <https://doi.org/10.1126/science.1163589>
- Snay, R. A., Cline, M. W., & Timmerman, E. L. (1987). Project REDEAM: Models for historical horizontal deformation (Technical Report NOS 125 NGS 42). Silver Springs, MD: National Geodetic Survey, NOAA.
- Snay, R. A., Freymueller, J. T., Craymer, M. R., Pearson, C. F., & Saleh, J. (2016). Modeling 3-D crustal velocities in the United States and Canada. *Journal of Geophysical Research: Solid Earth*, 121, 5365–5388. <https://doi.org/10.1002/JB011707>
- Song, T., & Simons, M. (2003). Large trench-parallel gravity variations predict seismogenic behavior in subduction zones. *Science*, 301(5633), 630–633. <https://doi.org/10.1126/science.1085557>
- Subarya, C., Chlieh, M., Prawirodirdjo, L., Avouac, J.-P., Bock, Y., Sieh, K., ... McCaffrey, R. (2006). Plate-boundary deformation associated with the great Sumatra–Andaman earthquake. *Nature*, 440, 46–51. <https://doi.org/10.1038/nature04522>
- Suito, H., & Freymueller, J. T. (2009). A viscoelastic and afterslip postseismic deformation model for the 1964 Alaska earthquake. *Journal of Geophysical Research*, 114, B11404. <https://doi.org/10.1029/2008JB005954>
- Sun, T., & Wang, K. (2015). Viscoelastic relaxation following subduction earthquakes and its effects on afterslip determination. *Journal of Geophysical Research: Solid Earth*, 120, 1329–1344. <https://doi.org/10.1002/2014JB011707>
- Sun, T., Wang, K., Iinuma, T., Hino, R., He, J., Fujimoto, H., ... Hu, Y. (2014). Prevalence of viscoelastic relaxation after the 2011 Tohoku-oki earthquake. *Nature*, 514(7520), 84–87. <https://doi.org/10.1038/nature13778>
- Sykes, L. (1971). Aftershock zones of great earthquakes, seismicity gaps, and earthquake prediction for Alaska and the Aleutians. *Journal of Geophysical Research*, 76(32), 8021–8041. <https://doi.org/10.1029/JB076i032p08021>
- Thatcher, W., & Rundle, J. B. (1979). A model for the earthquake cycle in underthrust zones. *Journal of Geophysical Research*, 84(B10), 5540–5556. <https://doi.org/10.1029/JB084iB10p05540>
- Thatcher, W., & Rundle, J. B. (1984). A viscoelastic coupling model for the cyclic deformation due to periodically repeated earthquakes at subduction zones. *Journal of Geophysical Research*, 89(B9), 7631–7640. <https://doi.org/10.1029/JB089iB09p07631>
- Tichelaar, B. W., & Ruff, L. J. (1993). Depth of seismic coupling along subduction zones. *Journal of Geophysical Research*, 98(B2), 2017–2037. <https://doi.org/10.1029/92JB02045>
- Toda, S., & Tsutsumi, H. (2013). Simultaneous reactivation of two, subparallel, inland normal faults during the Mw 6.6 11 April 2011 Iwaki earthquake triggered by the Mw 9.0 Tohoku-oki, Japan, earthquake. *Bulletin of the Seismological Society of America*, 103(2B), 1584–1602. <https://doi.org/10.1785/0120120281>
- Tomita, F., Kido, M., Ohta, Y., Iinuma, T., & Hino, R. (2017). Along-trench variation in seafloor displacements after the 2011 Tohoku earthquake. *Science Advances*, 3(7), e1700113. <https://doi.org/10.1126/sciadv.1700113>
- Trubienko, O., Garau, J. D., & Fleitout, L. (2014). Models of postseismic deformation after megathrust earthquakes: The role of various rheological and geometrical parameters of the subduction zone. *Solid Earth Discussions*, 6(1), 427–466. <https://doi.org/10.5194/sed-6-427-2014>
- Tsang, L. L. H., Meltzner, A. J., Hill, E. M., Freymueller, J. T., & Sieh, K. (2015). A paleogeodetic record of variable interseismic rates and megathrust coupling at Simeulue Island, Sumatra. *Geophysical Research Letters*, 42, 10,585–10,594. <https://doi.org/10.1002/2015GL066366>
- van Dinther, Y., Gerya, T. V., Dalguer, L. A., Mai, P. M., Morra, G., & Giardini, D. (2013). The seismic cycle at subduction thrusts: Insights from seismo-thermo-mechanical models. *Journal of Geophysical Research: Solid Earth*, 118, 6183–6202. <https://doi.org/10.1002/2013JB010380>
- Vauchez, A., Tommasi, A., & Mainprice, D. (2012). Faults (shear zones) in the Earth's mantle. *Tectonophysics*, 558–559, 1–27. <https://doi.org/10.1016/j.tecto.2012.06.006>
- Vigny, C., Simons, W., Abu, S., Bamphenyu, R., Satirapod, C., Choosakul, N., ... Socquet, A. (2005). Insight into the 2004 Sumatra–Andaman earthquake from GPS measurements in southeast Asia. *Nature*, 436, 201–206. <https://doi.org/10.1038/nature03937>
- Vigny, C., Socquet, A., Peyrat, S., Ruegg, J. C., Metois, M., Madariaga, R., ... Kendrick, E. (2011). The 2010 Mw 8.8 Maule megathrust earthquake of Central Chile, monitored by GPS. *Science*, 332, 1417–1421. <https://doi.org/10.1126/science.1204132>
- Wang, K. (1995). Coupling of tectonic loading and earthquake fault slips at subduction zones. *Pure and Applied Geophysics*, 145(3–4), 537–559. <https://doi.org/10.1007/BF00879588>
- Wang, K., & Dixon, T. H. (2004). “Coupling” semantics and science in earthquake research. *Eos, Transactions of the American Geophysical Union*, 108, 180. <https://doi.org/10.1029/2004EO180005>
- Wang, K., Hu, Y., Bevis, M., Kendrick, E., Smalley, R. J., Vargus, R. B., & Lauria, E. (2007). Crustal motion in the zone of the 1960 Chile earthquake: Detangling earthquake-cycle deformation and forearc-sliver translation. *Geochemistry, Geophysics, Geosystems*, 8, Q10010. <https://doi.org/10.1029/2007GC001721>
- Wang, K., Hu, Y., & He, J. (2012). Deformation cycles of subduction earthquakes in a viscoelastic Earth. *Nature*, 484, 327–332. <https://doi.org/10.1038/nature11032>
- Wang, K., & Tréhu, A. M. (2016). Invited review paper: Some outstanding issues in the study of great megathrust earthquakes—The Cascadia example. *Journal of Geodynamics*, 98, 1–18. <https://doi.org/10.1016/j.jog.2016.03.010>
- Watanabe, S.-I., Sato, M., Fujita, M., Ishikawa, T., Yokota, Y., Ujihara, N., & Asada, A. (2014). Evidence of viscoelastic deformation following the 2011 Tohoku-oki earthquake revealed from seafloor geodetic observation. *Geophysical Research Letters*, 41, 5789–5796. <https://doi.org/10.1002/2014GL061134>
- Wessel, P., Smith, W. H. F., Scharroo, R., Luis, J., & Wobbe, F. (2013). Generic mapping tools: Improved version released. *Eos, Transactions American Geophysical Union*, 94(45), 409–410. <https://doi.org/10.1002/2013EO450001>
- Wesson, R. L., Melnick, D., Cisternas, M., Moreno, M., & Ely, L. L. (2015). Vertical deformation through a complete seismic cycle at Isla Santa María, Chile. *Nature Geoscience*, 8(7), 547–551. <https://doi.org/10.1038/ngeo2468>
- Weston, J., Ferreira, A. M. G., & Funning, G. J. (2014). Joint earthquake source inversions using seismo-geodesy and 3-D earth models. *Geophysical Journal International*, 198(2), 671–696. <https://doi.org/10.1093/gji/ggu110>
- White, S. M., Trenkamp, R., & Kellogg, J. N. (2003). Recent crustal deformation and the earthquake cycle along the Ecuador–Colombia subduction zone. *Earth and Planetary Science Letters*, 216(3), 231–242. [https://doi.org/10.1016/S0012-821X\(03\)00535-1](https://doi.org/10.1016/S0012-821X(03)00535-1)
- Wiseman, K., Bürgmann, R., Freed, A. M., & Banerjee, P. (2015). Viscoelastic relaxation in a heterogeneous Earth following the 2004 Sumatra–Andaman earthquake. *Earth and Planetary Science Letters*, 431(C), 308–317. <https://doi.org/10.1016/j.epsl.2015.09.024>
- Witter, R. C., Briggs, R. W., Engelhart, S. E., Gelfenbaum, G., Koehler, R. D., & Barnhart, W. D. (2014). Little late Holocene strain accumulation and release on the Aleutian megathrust below the Shumagin Islands, Alaska. *Geophysical Research Letters*, 41, 2359–2367. <https://doi.org/10.1002/2014GL059393>

- Witter, R. C., Carver, G. A., Briggs, R. W., Gelfenbaum, G., Koehler, R. D., La Selle, S., ... Hill, T. D. (2016). Unusually large tsunamis frequent a currently creeping part of the Aleutian megathrust. *Geophysical Research Letters*, 43, 76–84. <https://doi.org/10.1002/2015GL066083>
- Yagi, Y., & Kikuchi, M. (2003). Co-seismic slip, post-seismic slip, and largest aftershock associated with the 1994 Sanriku-haruka-oki, Japan, earthquake. *Geophysical Research Letters*, 30(22), 2177. <https://doi.org/10.1029/2003GL018189>
- Yamagiwa, S., Miyazaki, S., Hirahara, K., & Fukahata, Y. (2015). Afterslip and viscoelastic relaxation following the 2011 Tohoku-oki earthquake (Mw9.0) inferred from inland GPS and seafloor GPS/acoustic data. *Geophysical Research Letters*, 42, 66–73. <https://doi.org/10.1002/2014GL061735>